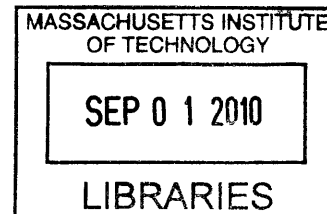# High Efficiency Solar Air Heaters with Novel Built-in Heat Storage for Use in a Humidification-Dehumidification Desalination Cycle

by

## Edward K. Summers

S.B., Massachusetts Institute of Technology (2008)

Submitted to the Department of Mechanical Engineering
in partial fulfillment of the requirements for the degree of

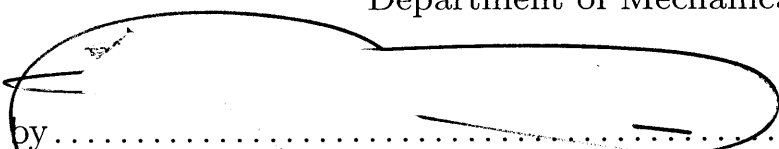Masters of Science in Mechanical Engineering

at the

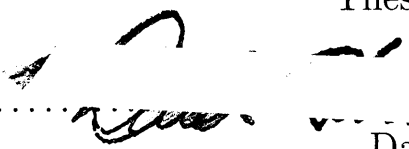MASSACHUSETTS INSTITUTE OF TECHNOLOGY

June 2010

Author . . . . . . . . . . . . . . . . . . . . . . . . . . . . . . . . . . . . . . . . . . . . . . . . . . . . .
Department of Mechanical Engineering
May 7, 2010

Certified by . . . . . . . . . . . . . . . . . . . . . . . . . . . . . . . . . . . . . . . . . . . . . . . .
John H. Lienhard V
Collins Professor of Mechanical Engineering
Thesis Supervisor

Accepted by . . . . . . . . . . . . . . . . . . . . . . . . . . . . . . . . . . . . . . . . . . . . . . .
David E. Hardt
Graduate Officer, Department of Mechanical Engineering

# High Efficiency Solar Air Heaters with Novel Built-in Heat Storage for Use in a Humidification-Dehumidification Desalination Cycle

by

Edward K. Summers

Submitted to the Department of Mechanical Engineering
on May 7, 2010, in partial fulfillment of the
requirements for the degree of
Masters of Science in Mechanical Engineering

## Abstract

Compared to solar water heaters, solar air heaters have received relatively little investigation and have resulted in few commercial products. However, in the context of a Humidication-Dehumidication (HD) Desalination cycle air heating offers signicant performance gains for the cycle. Solar collectors can be over 40% of an air-heated HDH system's cost, thus design optimization is crucial. Best design practices and sensitivity to material properties for solar air heaters are investigated, and absorber solar absorptivity and glazing transmissivity are found to have the strongest effect on performance. Wind speed is also found to have a significant impact on performance. Additionally a well designed collector includes a double glazing, roughened absorber plates for superior heat transfer to the airstream. A collector in this configuration performs better than current collectors with an efficiency of 58% at a normalized gain of 0.06 K m$^2$/W. Additionally, maintaining a constant air outlet temperature is also important for HD cycle performance. The use of built in phase change material storage (PCM) is found to produce consistent air outlet temperatures throughout the day or night. Using PCM directly below the absorber plate avoids heat transfer inefficiencies by using the working fluid to transfer energy to another storage system. Using a two dimensional finite element model it is found that a PCM layer of 8 cm below the absorber plate is sufficient to produce a consistent output temperature close to the PCM melting temperature with a time-averaged collector efficiency of 35%. However, this efficiency is significantly lower than a collector without storage, indicating a trade-off between efficiency and constant temperature heating, and suggesting alternative forms of energy storage might be more viable. Collectors that can deliver consistent outlet temperatures with good efficiency increase the performance of the HDH cycle. A prototype collector with storage is also built.

Thesis Supervisor: John H. Lienhard V
Title: Collins Professor of Mechanical Engineering

# Acknowledgments

Thanks to my advisor, John Lienhard, for his guidance, to my labmates for collaborating on this project.

Thanks to Alexander Guerra for his help with the ADINA FEM software, taking on the software's steep leaning curve.

Also, to The Center for Clean Water and Clean Energy at MIT and KFUPM, and to The King Fahd University of Petroleum and Minerals for funding this project and assuring I got a paycheck.

Thanks to our co-collabrators at KFUPM, Prof. M.A. Antar, Prof. S.M. Zubair, and Prof. P. Gandhidasan, for contributing to this work in various respects.

And lastly to my friends and family for supporting my endeavors, and putting up with my absence when I was preparing for quals.

# Contents

# List of Figures

# List of Tables

15

# Nomenclature

**Roman Symbols**

$A_p$      Collector area [m$^2$]

$A_{chan}$      Cross-sectional area of airflow channel [m$^2$]

$c_p$      Specific heat capacity at constant pressure [J/kg K]

$d$      Depth [m]

$d_h$      Hydraulic diameter [m]

$\mathcal{F}$      Radiation transmittance factor

$f$      Friction factor

$F'$      Collector efficiency factor

$F_R$      Collector heat removal factor or effectiveness

$f_r$      Rough surface friction factor

$F_{cg}$      View factor between collector and ground

$F_{cs}$      View factor between collector and sky

$g$      Acceleration of gravity [m/sec$^2$]

$g_r$      Dimensionless roughness constant

$h$      Height [m]

$h^+$      Non dimensional rib height

$h_1$      Convective heat transfer coefficient between absorber and airstream [W/m$^2$K]

$h_2$      Convective heat transfer coefficient between glazing and airstream [W/m$^2$K]

$h_r$      Radiation heat transfer coefficient between the absorber and glazing [W/m$^2$K]

$h_{sf}$      Latent heat of solidification [J/kg]

| $h_{rib}$ | Rib height [m] |
|---|---|
| $I_T$ | Solar irradiation flux on a tilted surface [W/m$^2$] |
| $k$ | Thermal conductivity [W/mK] |
| $k_s$ | Sand grain roughness [m] |
| $K_{ext}$ | Glazing plate extinction coefficient |
| $l_c$ | Characteristic length [m] |
| $\dot{m}$ | Mass flow rate of air though channel [kg/sec] |
| $n$ | Glazing index of refraction |
| $NG$ | Normalized gain [Km$^2$/W] |
| $p_{rib}$ | Rib separation distance [m] |
| $Pr$ | Prandtl number of air |
| $q_u$ | Useful heat gain by the fluid per unit collector area [W/m$^2$] |
| $Q_l$ | Total heat loss from collector [W] |
| $Ra$ | Rayleigh number - Natural convection between glazing plates |
| $Re_{d_h}$ | Reynolds number based on hydraulic diameter - Airflow through collector |
| $r$ | Fraction of solar radiation received by glazing panel |
| $S$ | Solar Heat flux into absorber plate [W/m$^2$] |
| $s$ | Relative density of a metal mesh |
| $St$ | Stanton number |
| $T$ | Temperature [K] |
| $t$ | Thickness [m] |
| $t_i$ | Simulation time index [sec] |
| $T_{melt}$ | PCM melting temperature [K] |
| $U_b$ | Bottom loss coefficient [W/m$^2$K] |
| $U_L$ | Overall heat loss coefficient [W/m$^2$K] |
| $U_t$ | Top loss coefficient [W/m$^2$K] |
| $V$ | Characteristic velocity [m/sec] |

| $w$ | Width [m] |

**Greek Symbols**

| $\alpha$ | Solar absorptivity |
| $\beta$ | Coefficient of thermal expansion for air [1/K] |
| $\Delta T$ | Temperature difference between the absorber and inner glazing [K] |
| $\delta T$ | Temperature range over which the PCM melts [K] |
| $\delta$ | Solar incidence angle |
| $\epsilon$ | Infrared emissivity |
| $\eta$ | Collector efficiency |
| $\theta_E$ | Solar radiation entrance angle |
| $\theta_I$ | Beam radiation incidence angle |
| $\theta_{tilt}$ | collector tilt angle |
| $\mu$ | Viscosity of air [Pa s] |
| $\nu$ | Kinematic viscosity of air [m$^2$/sec] |
| $\phi$ | Latitude |
| $\rho$ | Density [kg/m$^3$] |
| $\rho_s$ | Solar reflectivity |
| $\rho_{s,g}$ | Average ground reflectance |
| $\sigma$ | Stefan-Boltzman constant [W/m$^2$ K$^4$] |
| $(\tau\alpha)$ | Transmittance-absorbtance product |
| $\tau$ | Solar transmissivity |
| $\tau_c$ | Time constant [sec] |

**Subscripts**

| $a$ | Absorber plate |
| $air$ | Air |
| $Al$ | Aluminum |
| $amb$ | Ambient conditions |

| | |
|---|---|
| *beam* | Beam irradiation component |
| *c*1 | Inner glazing plate |
| *c*2 | Outer glazing plate |
| *chan* | Airflow channel |
| *d* | Diffuse irradiation component |
| *f* | Fluid |
| *g* | Glazing plate material property |
| *gr* | Ground reflected irradiation component |
| $h_s$ | Forced convection heat transfer coefficient in a smooth pipe [W/m$^2$] |
| *in* | Air inlet |
| *ins* | Insulation |
| *l* | Phase change material liquid phase |
| *orth* | Orthogonal component of solar radiation |
| *out* | Air outlet |
| *PCM* | Phase change material |
| *pll* | Parallel component of solar radiation |
| *r* | Radiation heat transfer |
| *s* | Phase change material solid phase |
| *sky* | Sky |
| *stack* | Glazing stack combination property |
| *T* | Radiation on a tilted surface |

# Chapter 1

# Introduction

Currently many areas of the word suffer from a scarcity of fresh drinking water. Despite the fact that the world is over 2/3 water, most of it is too salty for human consumption. According to the International Water Management Institute [1] many areas of the world have severe physical water scarcity, as shown in Figure 1-1 [1] .

**Areas of physical and economic water scarcity**
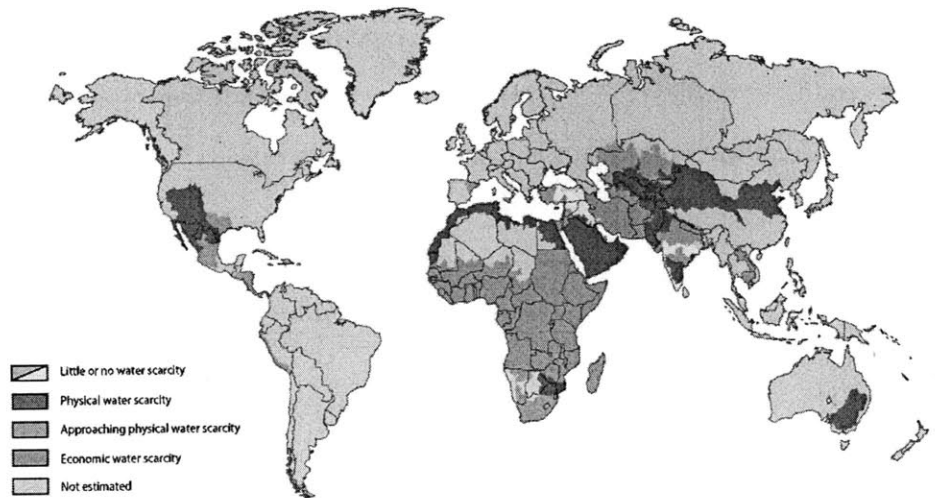


Figure 1-1: World map detailing water scarcity.

These same areas, however, are endowed with great solar resources as seen in Figure 1-2 [2].
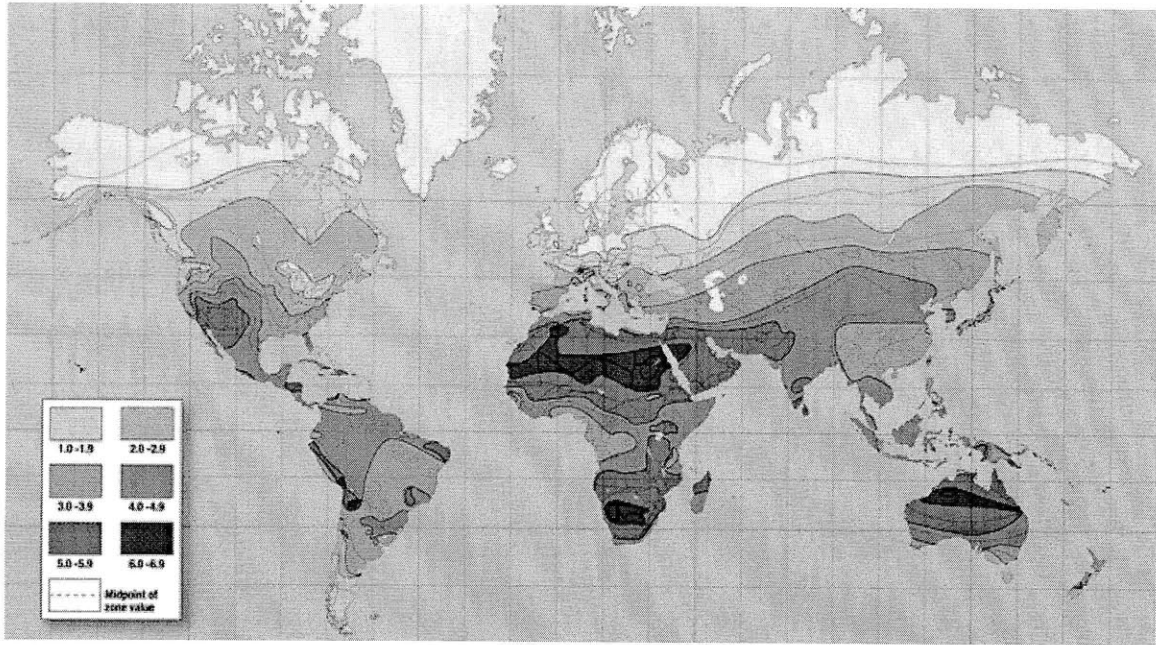
Figure 1-2: World map showing the distribution of solar resources in units of $kWh/m^2$ day

Humidification-Dehumidification (HD) desalination is a means to bring this resource to bear in solving the physical water scarcity problem. Utilizing solar energy these systems could be deployed in parts of the world without access to "on-grid" energy, or fossil fuels, which providing cheap drinking water.

The HD system works in many ways like the earth's natural water cycle, where the sun's energy evaporates water from the oceans, which condenses in the atmosphere and returns to earth in the form of precipitation that collects in rivers and streams. Water can then be used for drinking.

The same method is used in a solar still, where the sun's energy evaporates water in a closed vessel, with the water condensing on the top surface of that vessel, which is exposed to the environment. However this is highly inefficient, as the entire latent heat of evaporation of water is lost to the environment.

The HD system aims to separate these components and use the latent heat of evaporation of water to pre-heat more water to be evaporated. Such a system is shown in Figure 1-3. The heat input for this system is in the form of solar heat.

Water enters the system and is used as the condensing fluid for a moist air stream, where it gains energy and is passed through a humidifier, mixing it with an air stream that is then heated and then condensed. The dried air is then passed back to the humidifier to gain more water.
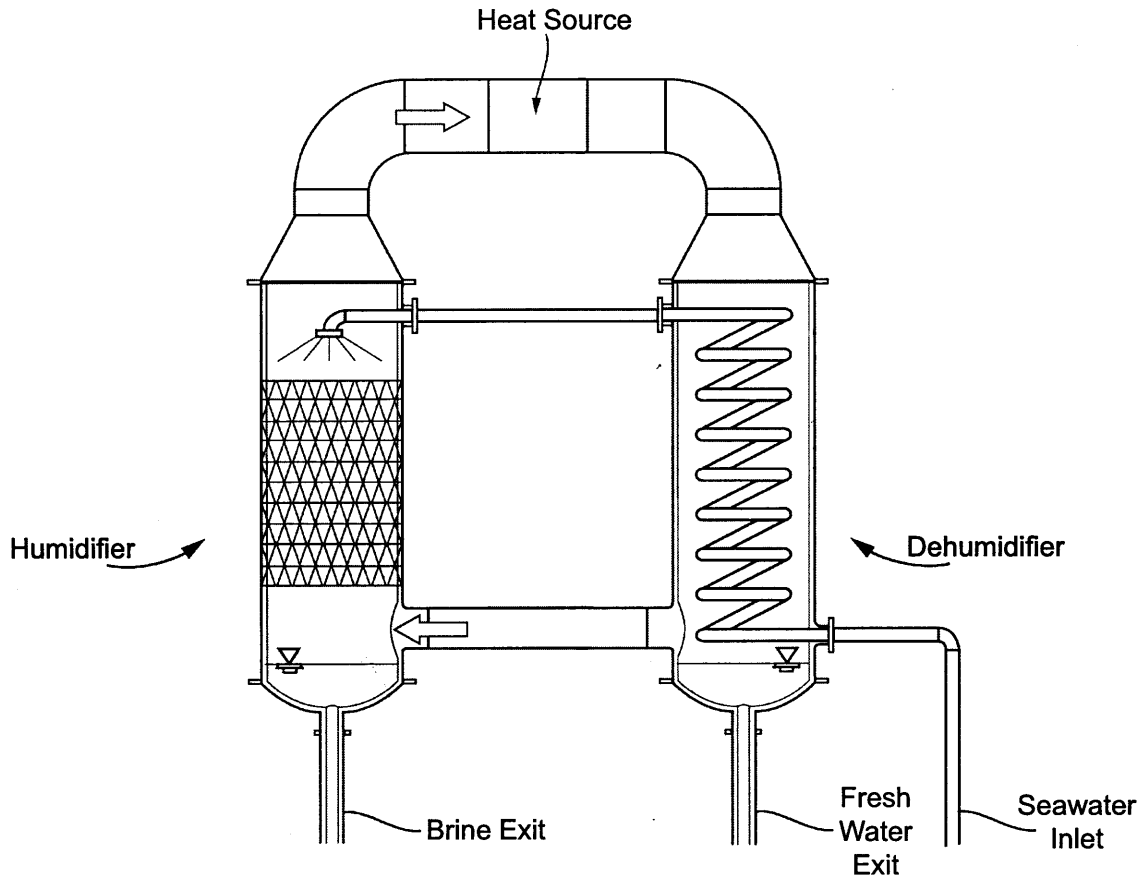


Figure 1-3: A single-stage HD desalination system. Arrows indicate the direction of air flow.

The solar air heater is a vital component of a HD desalination system. Such a system, the first of its kind, is described by [3]. Instead of heating water before it is evaporated, the solar heater heats the air and moisture is introduced into the heated air. This continues over a number of cycles to maximize the moisture introduced.

The solar air heaters in this cycle are constantly exposed to moist air on the inside, and solar radiation and blowing sand in the desert environment on the outside. As a

result the collectors have to be resistant to corrosion, and be able to withstand harsh weathering for an extended period of time while efficiently transferring heat to moist air that can have as much as 15% water vapor by weight.

The subject of this work is to gain a better understanding of the heat transfer processes in such a collector and to optimize its design to enable maximum performance of the overall HD desalination cycle.

# Chapter 2

# Existing Solar Air Heating Technologies and Best Design Practices

## 2.1 Comparison of Performance

The standard metric of a solar air heater's performance is the collector thermal efficiency. It is defined by Equation 2.1

$$\eta = \frac{\dot{m}c_p(T_{out} - T_{in})}{I_T A_p} \tag{2.1}$$

where terms are defined in nomenclature. It is the energy gain of the airstream divided by the total solar energy incident on the collector. This definition of performance is that used by the ASHRAE 93-2003 Standard for solar collector testing [4], and it defines both the instantaneous and time averaged efficiencies when evaluating dynamically changing solar radiation inputs and temperature profiles.

In solar collectors, efficiency decreases with fluid temperature gain, as heat losses are directly proportional to temperature. The most common way of showing solar air heater efficiency is to plot the efficiency versus the normalized heat gain as defined

by Equation 2.2. It has has the units K m$^2$/W.

$$NG = \frac{(T_{out} - T_{air})}{I_T} \qquad \cdot \qquad (2.2)$$

The normalized gain will decrease with increasing air mass flow rate as the temperature rise in the collector will be lower as the air spends less time being heated. For the purposes of all the comparisons in this thesis, the air inlet temperature is equal to the ambient air temperature, making the temperature difference in the numerator equal to the temperature rise in the collector.

## 2.2 Existing Air Heater Technologies

### 2.2.1 Historical Technologies

Air heating collectors have been occasionally used since World War II, mostly for low temperature space heating applications. The collectors are typically flat plate with large airflow channels. Air flows over or under the absorber plate, and double-pass strategies are sometimes employed. The 1959 Colorado Solar House [5] used a glass and metal collector with many glazings staggered on top of each other, and achieved 30% efficiency. Figure 2-1 shows the layout the Colorado Solar House collectors.
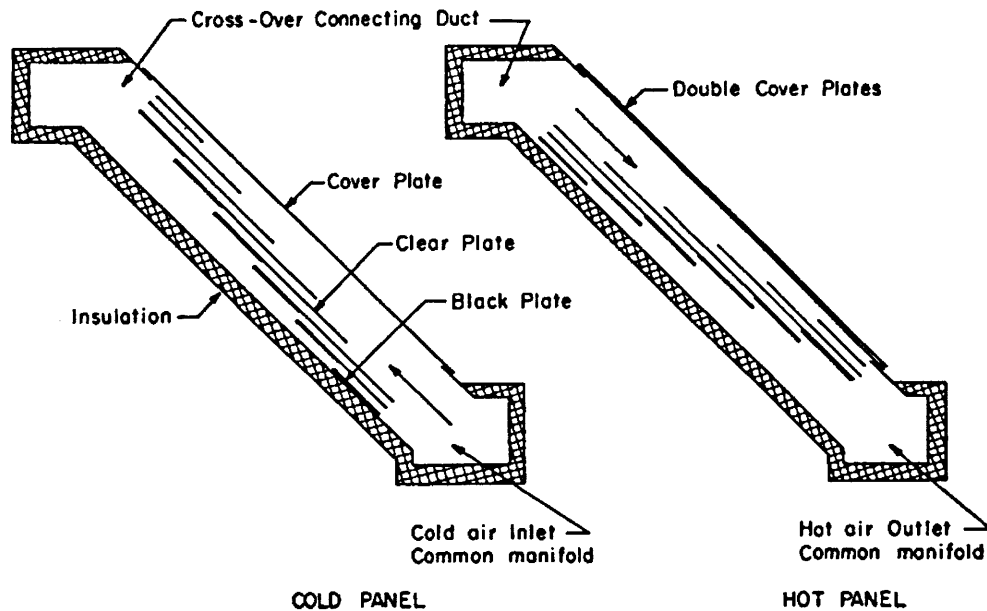
Figure 2-1: Air heating collectors from the Colorado Solar House

In the 1960s, solar energy was developed in India as a means of cheap energy for crop drying. Gupta and Garg [6] tested several designs that used both corrugated absorber surfaces as well as wire mesh packing over the absorber. They also provided an overall efficiency that took into account the power to force air through the heater. They showed that corrugated surfaces performed better than those enhanced with wire mesh, achieving a maximum of 65% overall energy conversion efficiency. A design by Close [7] was able to achieve temperatures of around 65 °C with a collector efficiency of 50%. This study also investigated the use of corrugated absorber surfaces to maximize heat transfer by increasing surface area, and used a trapped layer of air between the single glazing surface and absorber.

Initial experiments using polymer materials were done by Whillier [8], who tested glazing made of Tedlar, a polyvinylfluoride (PVF) film. It was found that, despite higher heat losses from the Tedlar, its improved transmittance compensated. It worked especially well when there was more than one glazing, and only the outer glazing was glass.

Interest in solar air heating, and alternative energy in general, picked up with the 1973 oil crisis. Many air heaters were patented in this period [9, 10, 11], and they included novel designs using multiple glazings, forcing air through jets to create more turbulence to enhance heat transfer near the absorber plate, and circulating air between the glazings. Satcunanathan and Deonarine [12] also explored passing air between multiple glazings before heating it, and they found collector efficiency gains of 10-15%.

The previous designs mainly used painted metal absorber surfaces and glass glazings. These surfaces are prone of corrosion and fouling especially in the presence of humid air. With the advent of new types of polymers it became possible to experiment with new designs that used materials with much lower thermal conductivity. Interest in polymer materials also occurred with Bansal [13] who tested PVF glazings in the environment for an extended period of time and found increased collector performance with PVF glazings. Use of packings to enhance heat transfer were investigated by Choudhury and Garg [14], who achieved a collector efficiency of 70% by using a packing material placed above the absorber plate and allowing air to pass through it. Sharma et al. [15] used a wire matrix packing above the absorber plate to enhance heat transfer.

### 2.2.2 Modern Air Heater Designs

**Improving Convective Heat Transfer and Air Residence Time**

Modern air heater designs have focused mainly on improving convective heat transfer at the absorber. Mittal and Varshney [16] investigated using wire mesh as a packing material, with air flowing between the absorber the second glazing through the mesh, achieving a collector efficiency of 70%. Figure 2-2 shows the flow path of this heater.
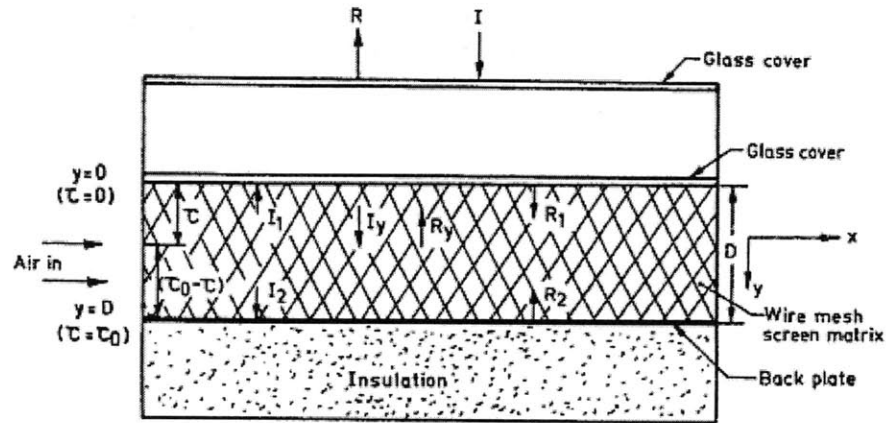
Figure 2-2: Flowpath from Mittal and Varshney

Mohamad [17] found that a packed bed of porous media improved heat transfer as well as pre-warming the air by first running it between two glazing plates. This also improved collector efficiency by reducing heat loss to the environment, and helped achieve an overall efficiency, which accounts for pumping losses for moving air through the collector, of 75%. Esen [18] compared several obstacles mounted on a flat plate to a plain flat plate and found that short triangular shaped barriers improved heat transfer efficiency the most by breaking up the boundary layer and reducing dead zones in the collector. Sahu and Bhagoria [19] used short (1.5 mm) ribs perpendicular to the absorber plate to break up airflow as it went over the absorber plate and ribs, as shown in Figure 2-3.
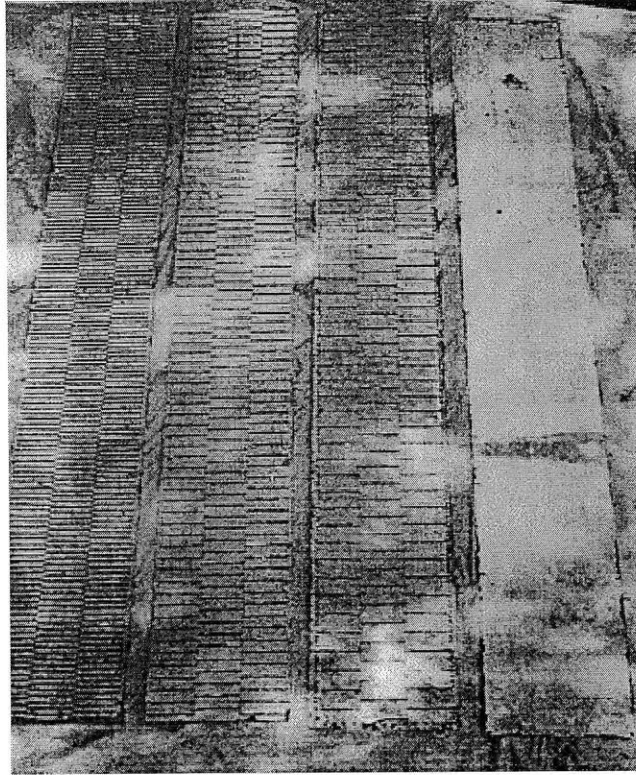
Figure 2-3: Roughened Absorber Plates from Sahu and Bhagoria

Romdhane [20] used small extensions from a metal plate to improve mixing of air on the plate. These extensions had the advantage of not increasing pressure drop like packed bed solar air heaters. Ho et al. [21] increased the collector efficiency of a flat metal absorber plate to 68% by running the air above and below the absorber plate, as shown in Figure 2-4. The flow turns 180 degrees to move back above the plate. This configuration increases pressure drop in the flow, but the paper does not report how much.
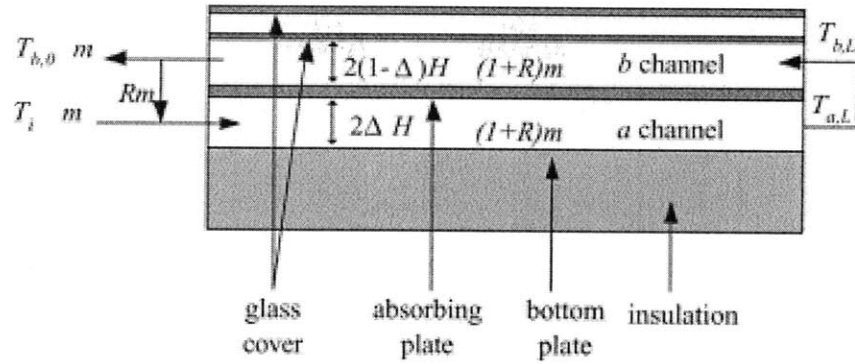
Figure 2-4: Flow path for heater in Ho et al.

Ramadan et al (2007) [22] also reported an efficiency increase using double pass heating in addition to using a limestone packing above the absorber plate and passing air through it, as shown in Figure 2-5.
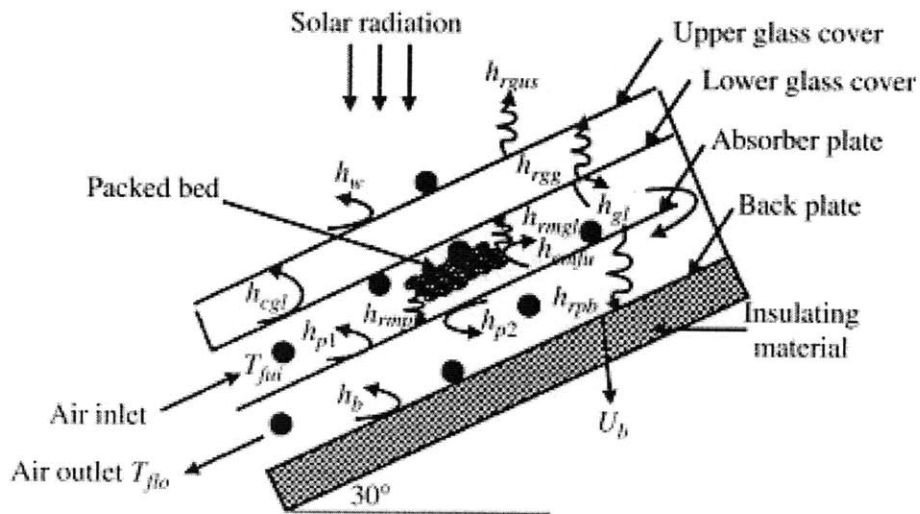


Figure 2-5: Flow path for a packed bed air heater from Ramadan et al. Black dots are temperature measurement points

## Selective Absorber Surfaces

A selective absorber coating is a coating that has a high solar absorptivity, and low infrared emissivity [23]. These coatings can help improve efficiency by increasing the absorptivity of the absorber plate and decreasing radiative loss. However at low temperature differences between the absorber and the environment, there is little

31

improvement.

Hachemi [24] studied the effect of selective surfaces on a solar air heater. The heater he tested compared a selectively coated absorber plate and a black painted absorber plate. The black plate was made from aluminum and the selective plate was sun-copper. Both collectors used a polycarbonate glazing with a stagnant air layer between the glazing and the absorber with air flowing under the absorber. For the case where fins were used, 5 cm long fins were attached to the bottom of the absorber plate perpendicular to the airflow in a staggered pattern. The fins impinged on the airflow to increase the rate of heat transfer. Their configuration is shown in Figure 2-6 The study found that, with a well-designed solar collector, which, minimizes thermal radiation from the absorber, efficiency gains from using selective surfaces alone vanish at high temperature difference. It also shows that using other improvements such as fins, make the marginal gain in efficiency even less. Figure 2-7 shows that data for selective vs. non-selective surfaces.



1. Glazing
2. Absorber plate
3. Collector chest
4. Fins
5. Air inlet
6. Insulation sheet
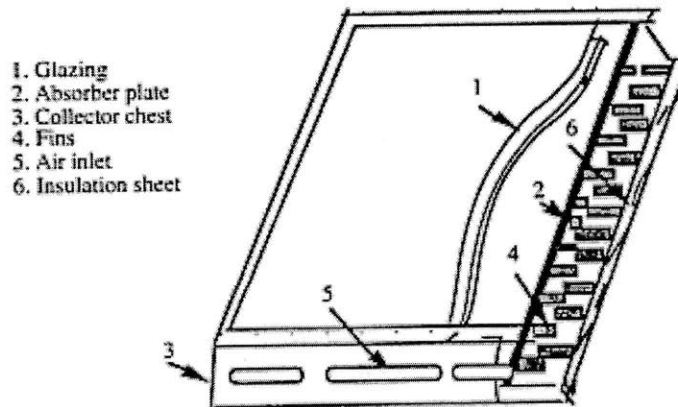
Figure 2-6: Configuration of impinging fins used by Hachemi
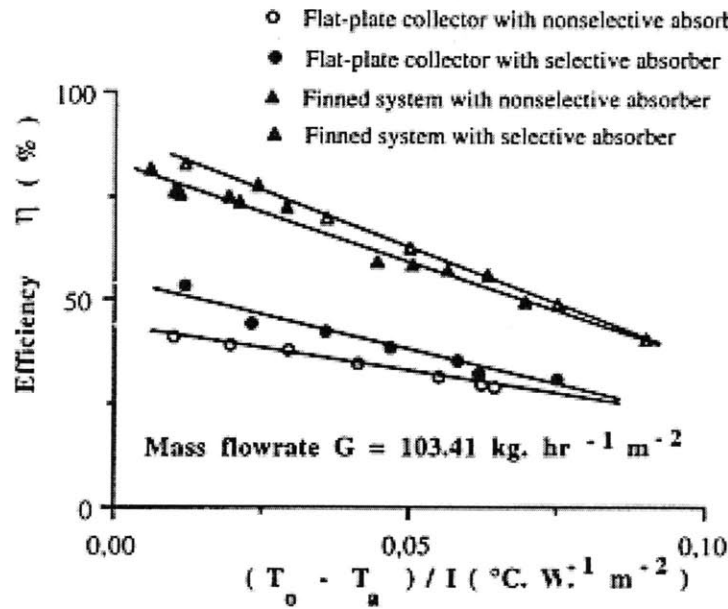
Figure 2-7: Efficiency vs. normalized heat gain with selective vs. non-selective surfaces from Hachemi

This figure shows an approximately 5% efficiency gain at 0.05 normalized heat gain, which corresponds to temperature difference of 50 °C at 1000 W/m$^2$ solar irradiation, which are approximately the conditions needed for a solar desalination system in a desert climate. This paper demonstrated that selective surfaces might not be that important with proper overall collector design.

Texieria et al. [25] found a doubling of efficiency for a unglazed flat plate operating at a temperature difference of 70 °C and solar irradiation of 1000 W/m$^2$ using selective surfaces as opposed to non-selective surfaces. This design's greatest enhancement was the addition of a selective surface as opposed to changing the absorber shape or adding glazings or additional insulation. Liu et al. [26] found only a 5% efficiency increase when using selective coatings on a corrugated absorber in a single-glazed solar air heater using a heavily insulated back plate with air flowing under the absorber. This compares with a reported 20% increase in efficiency by adding corrugation and not using selective surfaces.

33

### Improvements On More Basic Designs

Other attempts have been made to improve existing flat plate absorber with limited success. These designs sacrifice efficiency for simplicity. Koyuncu [27] compared several flat plate designs, with one ribbed plate design, and several glazing configurations. The most efficient, at 45.8%, was flat black metal plate with a single polymer glazing, and air passing over the absorber. Matrawy [28] used fins below the absorber plate to enhance heat transfer to the air as it flowed under the absorber, but only achieved 50% collector efficiency.

### Air Heaters for HD Desalination

Chafik [3] investigated the design of solar air heaters for his process. However the designs required a great deal of improvement to be used effectively for long periods of time in an environment with constant moisture and blown sand. The solar collectors used in the Chafik process were a first attempt at what might be used in a large scale solar-driven HD desalination system. They were built entirely of polymers and used angled flat absorber plates where air went under the absorber. The most efficient design averaged about 40% and used a double glazing.

## 2.2.3 Commercial Products

To date there are no commercial systems that utilize solar air heaters for solar desalination, only products for home heating and crop drying. Most products have moderate temperature rise, and are very expensive. Several of these products were rated by the Solar Collector and Certification Corporation [29], which gives data for efficiency as a function of temperature rise normalized by solar irradiation. Table 2.1 shows their efficiency for a temperature rise of 50° C and a solar irradiation of 1 kW/m$^2$, which are representative values for a HD desalination application. The best performing collector under these conditions is the Sunmate Sm-14, achieving only 32% efficiency.

Table 2.1: Efficiencies of commercial solar air heaters at 50 °C temperature rise and 1 kW/m$^2$ solar irradiation.

| Product | Manufacturer | Efficiency |
|---|---|---|
| Solarway 6000 | Energy Conserv. Products and Services | 12.2% |
| SunMate Sm-14 | Environmental Solar Systems | 32.3% |
| MSM-101 | SolarMax Heating | 10.2% |
| Northen Comfort NC-32 | Sunsiaray Solar Inc. | 26.6% |
| SolarSheat 1500G | Your Solar Home | 14.0% |

## 2.3 Comparison of Designs in Academic Literature

When evaluating the performance of different solar air heaters it is necessary to take into account a variety of parameters. Performance data varies widely among academic literature. The following table summarizes some air heaters for which the necessary performance parameters if given with other important operation and performance parameters listed if known. Some values in the table were calculated from other parameters.

Table 2.2: Operating conditions of solar air heaters in literature.

| Heater/Year | $d_h$ [m] | $\dot{m}$ [kg/s] | $Re_{d_h}$ | $I$ [W/m$^2$] | $T_{out}$ [°C] | $T_{out} - T_{in}$ [°C] | NG [Km$^2$/W] | $\eta$ |
|---|---|---|---|---|---|---|---|---|
| Romdhane [20] | | | | | | 60 | 0.05 | 80% |
| Sahu and Bhagoria [19] | 0.044 | 0.0164 | 8000 | 815 | 53 | 12 | 0.0147 | 79.5% |
| Mohamad [17] | | | | | | | 0.12 | 75% |
| Ramadan et al. [22] | 0.214 | 0.0105 | 1026 | 662 | 68.5 | 38.5 | 0.0582 | 45.3% |
| Choudhury, and Garg [14] | | | | | | | | |
| Mittal and Varshney [16] | 0.047 | 0.025 | 6291 | 600 | 48 | 18 | 0.03 | 70% |
| Ho, Yeh, and Wang [21] | 0.086 | 0.0214 | 6693 | 1100 | | | | 68% |
| Satucunanathan and Deonarine [12] | 0.073 | 0.0418 | 5378 | 850 | | 23.8 | 0.028 | 68% |
| Esen [18] | | 0.02 | | 900 | 58.9 | 23.3 | 0.0259 | 53% |
| Close [7] | 0.157 | 0.2842 | 31091 | 504 | 54.4 | 30.8 | 0.0611 | 40% |
| Sharma et al. [15] | 0.328 | 0.0165 | 1627 | 900 | 50 | 14 | 0.0156 | 50% |
| Matrawy [28] | 0.095 | 0.0140 | 1459 | 800 | 63 | 33 | 0.0413 | 50% |
| Koyuncu [27] | | | | 1000 | 45 | 15 | 0.015 | 46% |
| Chafik [3] | 0.011 | 0.00068 | 2411 | 800 | 48 | 22 | 0.0275 | 40% |

As with other heat exchangers, a solar air heater decreases in efficiency with a greater temperature drop. The most common way of showing solar air heater efficiency is to plot the efficiency versus the normalized heat gain, or the rise in temperature divided by the solar radiation flux. Figure 2-8 shows the reported efficiencies of solar air heaters in academic literature as a function of the normalized gain. The five points in grey are considered the current state of the art in solar air heating. The best commercial heater, the Sunmate Sm-14 [29], is also included for comparison.
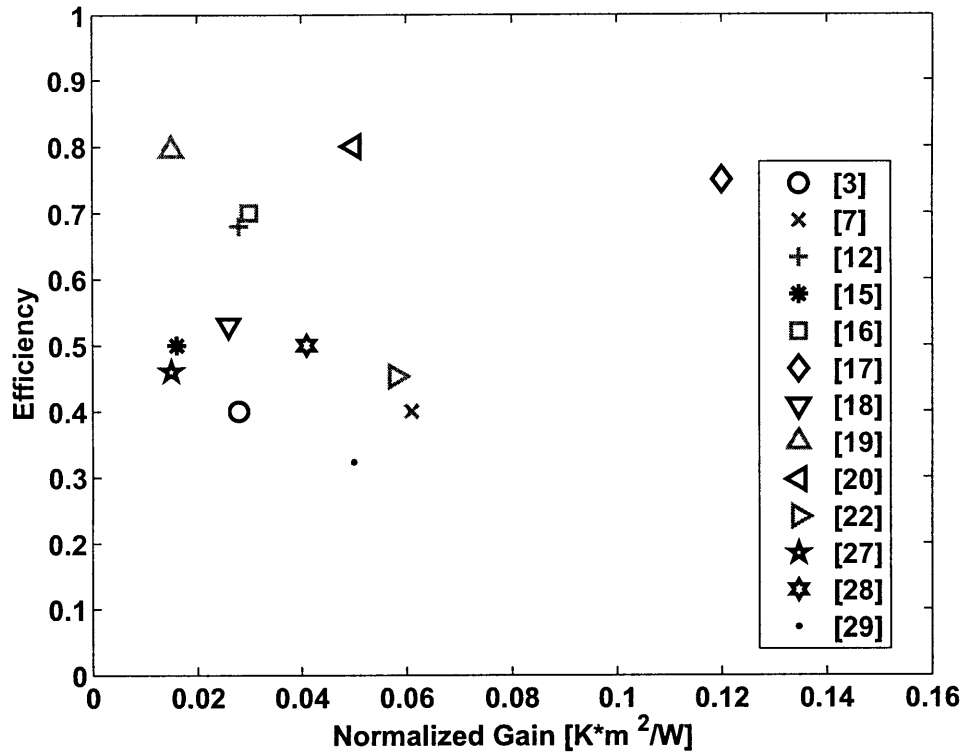
Figure 2-8: Efficiency vs. normalized gain for various heaters in literature

There are two outliers which will be excluded from the comparison as they do not fit with the majority of the data. Mohamad [17] is a theoretical study that claims an extremely large efficiency improvement with an addition of porous media as an absorber, with 75% efficiency at 0.12 K m$^2$/W of normalized gain. However, experiments conducted on a collector in a similar configuration [30] show only 60% efficiency at a normalized gain of 0.017, which is significantly lower than the normalized gain claimed by Mohamad, therefore we discount Mohamad's prediction. Romdhane [20] is an experimental study with various types of surface roughening. He claims a near constant efficiency through increasing normalized gain to his highest normalized gain and efficiency. However, when experiments are done by varying mass flow rate, the same collector shows a linearly increasing trend with increasing mass flow rate, which is expected. The increase in mass flow rate is accompanied by a decrease in temperature rise (and normalized gain) as the air has a shorter residence time in the

37

collector. This is inconsistent with the reported results for varying normalized gain, and therefore Romhdane's maximum reported efficiency is discounted.

To get a better understanding of what makes a solar air heater preform well, and to guide future designs, the highest performing heaters design attributes are tabulated in Table 2.3.

Table 2.3: Design characteristics of the best performing solar air heaters.

| Heater | Multi-Glazed | Multi-Pass | Airflow w/r/t Abs. | Rough-ened Abs. | Corru-gated Abs. | Packing | Construction Materials |
|---|---|---|---|---|---|---|---|
| Sahu and Bhagoria [19] | No | No | Above | Yes | No | No | Absorber: Galvinized Steel, Glazing: Glass |
| Ramadan et al. [22] | Yes | Yes | Above/ Below | No | No | Yes | Packing: Gravel or Limestone, Absorber: Steel, Glazing: Glass |
| Mittal and Varshney [16] | Yes | No | Above | No | No | Yes | Absorber and Wire Matrix: Metal, Glazing: Glass |
| Satucunan-than and Deonarine [12] | Yes | Yes | Above | No | Yes | No | Absorber: Aluminum or Steel Glazing: Glass |
| Close [7] | Yes | No | Below | No | Yes | No | Absorber: Aluminum or Steel, Glazing: Glass |

By comparing the designs of the five best heaters a list of apparent best design practices can be obtained.

- *Air flow over the absorber plate*: Having air flow above the absorber decreases losses from the top of the absorber plate and eliminates conduction resistance through the plate. Many modern air heaters use this method. [12, 16, 19]


- *Packing materials*: Packing materials in the air stream improve heat transfer

38

by mixing the air and providing more surface area to absorb radiation. Packing also provides sensible heat storage but comes at the cost of high pressure drop [16, 22]. In the context of HDH, the materials have to be moisture and corrosion resistant. Since they add effective energy storage to the collector they will be considered in a separate transient analysis.

- *Roughened absorber plate*: improves convection heat transfer into the air. Rough configurations also increase pressure drop, but only marginally when compared to a smooth plate for duct cross sections used in solar air heating. Roughening for increased convection has been extensively investigated, and has shown performance improvements in collectors [17, 19].

- *Multiple passes of air through the collector*: improves heat gain by increasing contact with the absorber, and makes absorber run cooler, decreasing losses [22]. However the same can be accomplished with a rough absorber plate without having a very thermally conductive absorber. This allows many more materials to be used as absorber surfaces, such as those with low thermal conductivity.

- *Multiple glazing layers*: reduces heat loss by infrared radiation and traps an insulating air layer between the glazings. However this comes at a greater material cost and lower solar transmissivity. All of the top performing heaters except Sahu and Bhagoria [19] use a double glazing.

- *Glass and metal construction*: provides better heat transfer characteristics and better durability. All the best performing collectors used glass and metal construction, as polymer alternatives, especially for glazings, suffer from low durability although providing optical properties comprable to glass [31].

## 2.3.1 Potential Shortcomings

When considering solar air heaters for a humidification-dehumidification desalination process these designs may have several shortcomings. Using packing material can cause the formation of cold spots which are not evenly heated that can lead to condensation. Flowing air over the absorber requires a good deal of insulation on the back of the absorber, as the high temperature of the absorber leads to losses if it is exposed to the environment. The use of glazing materials has to be considered, as heat is lost to the environment due to infrared radiation. The glazings have to be robust to UV exposure and resistant to corrosion and fouling in the presence of high humidity. Some early designs [32] employed a glass honeycomb structure under the glazing that was transparent to visible light and functioned as a radiation trap, but these honeycombs are hard to fabricate and did not appear in modern designs.

When air flow through the collector is interrupted, temperature in the collector can rise quickly. No published designs investigated this stagnation temperature. However it might present a problem for designs using plastic absorbers and glazings, which have significantly lower working temperatures than metal and glass.

# Chapter 3

# Solar Air Heater Without Storage: Parameter Sensitivity Study

## 3.1  Introduction

Operating demands placed on solar air heaters require the use of unique materials for the construction of important components like the absorber plates and glazing surfaces. These materials might not have optimal thermal properties in all areas. For example, an engineering plastic may have high solar absorptivity and operating temperature, but might have high infrared emissivity, making it prone to radiative loss. When designing a heater it is necessary to optimize thermal performance, and operating requirements (like moisture level) with cost, and therefore knowing what thermal properties impact performance more than others is vital for selecting cost effective materials, and making design decisions. This study explores how these attributes affect the thermal performance of the collector.

## 3.2  Baseline Heater

### 3.2.1  Heater Geometry

Using information gleaned from the literature review, a simple baseline design was devised. To obtain the required temperature rise a long a narrow collector was necessary, and it has the cross section as illustrated in Figure 3-1. In reality this long effective collector can be achieved by placing shorter modules in series. The total length of the collector is 10 m, and width of 0.3 m, giving a collector area of 3 $m^2$. It consists of an aluminum absorber coated with carbon black paint, and low-iron glass glazing panels. The outside is insulated with fiberglass insulation.
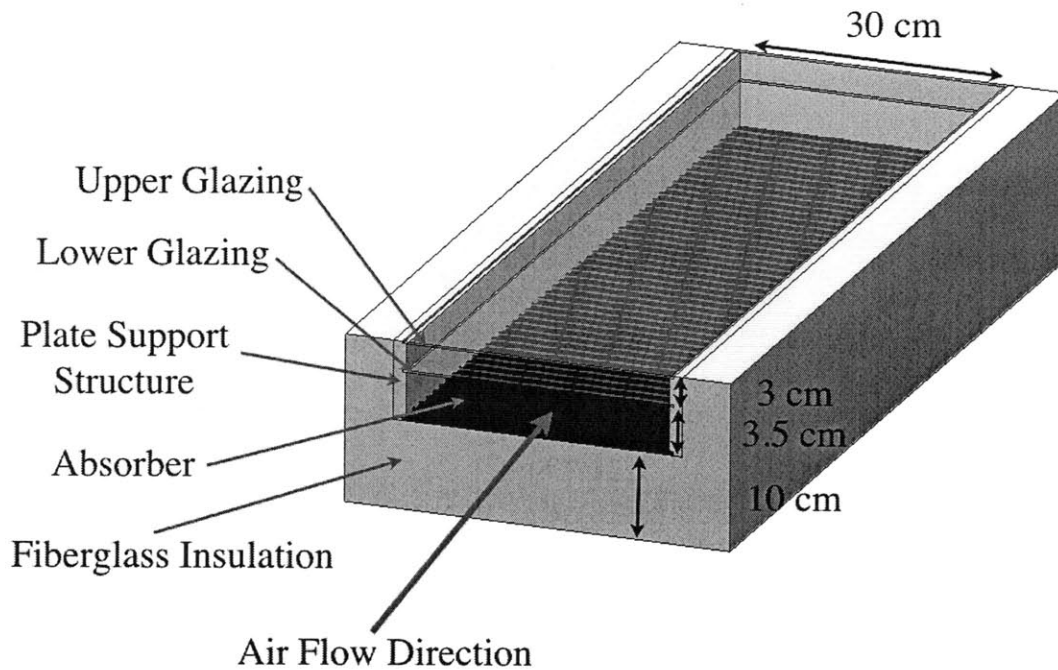
Figure 3-1: Diagram of heater cross section

## 3.2.2 Environmental Conditions

The collector was assumed to be situated in a desert climate where HD desalination is likely to be used. The reference location is Dhahran, Saudi Arabia. The outdoor wind speed is assumed to be a moderate 5 m/s, which is consistent with averages for a desert climate such as Saudi Arabia [33]. The characteristic length over which wind blows is the average of the width and length of the collector, as wind direction is highly variable. The solar insolation for this study was assumed to be constant at a maximum of 900 W/m². The solar radiation in this study was assumed to be entirely beam radiation, due to the climate's typically low air moisture content, and for simplicity of the model. Table 5.2 details the environmental constants.

Table 3.1: Constant parameters for simulating baseline design.

| Constants | Values |
|---|---|
| Solar Irradiation | 900 W/m$^2$ |
| Ambient Wind Speed | 5 m/s |
| Latitude | 27 ° |
| Solar Declination | 23 ° |
| Collector Tilt Angle | 45 ° |
| Collector Inlet Temperature | 30 °C |
| Ambient Air Temperature | 30 °C |
| Dew Point Temperature | 4 °C |
| Insulation Conductivity | 0.02 W/m K |

## 3.2.3   Materials Selection and Properties

Many of the well performing heaters found in the literature review used traditional materials for construction: metal and glass. In the baseline design, a metal absorber plate was used. The plate was coated in carbon black paint [34]. The glazing plates were made of "water white" glass [31]. The properties of these materials are given in Table 5.3. The mass flow rate of 0.029 kg/sec was chosen to obtain a normalized gain of 0.06 K/m$^2$W for the baseline design. The table below summarizes all the constant values used in the design.

Table 3.2: Baseline values of varied material properties.

| Material Properties | Value |
|---|---|
| Glazing Refraction Index | 1.526 |
| Glazing Extinction Coefficient | 4 |
| Absorber Solar Absorptivity | 0.94 |
| Glazing IR Emissivity | 0.92 |
| Absorber IR Emissivity | 0.86 |
| Transmittance Absorptance Product - $(\tau\alpha)$ | 0.77 |

## 3.3   Thermal Model

### 3.3.1   Overall Governing Equations

In steady state, the heat transfer processes in the collector can be modeled as a series of thermal resistances. Each of these heat transfer resistances can be combined into several lumped parameters, as shown in Figure 3-2.
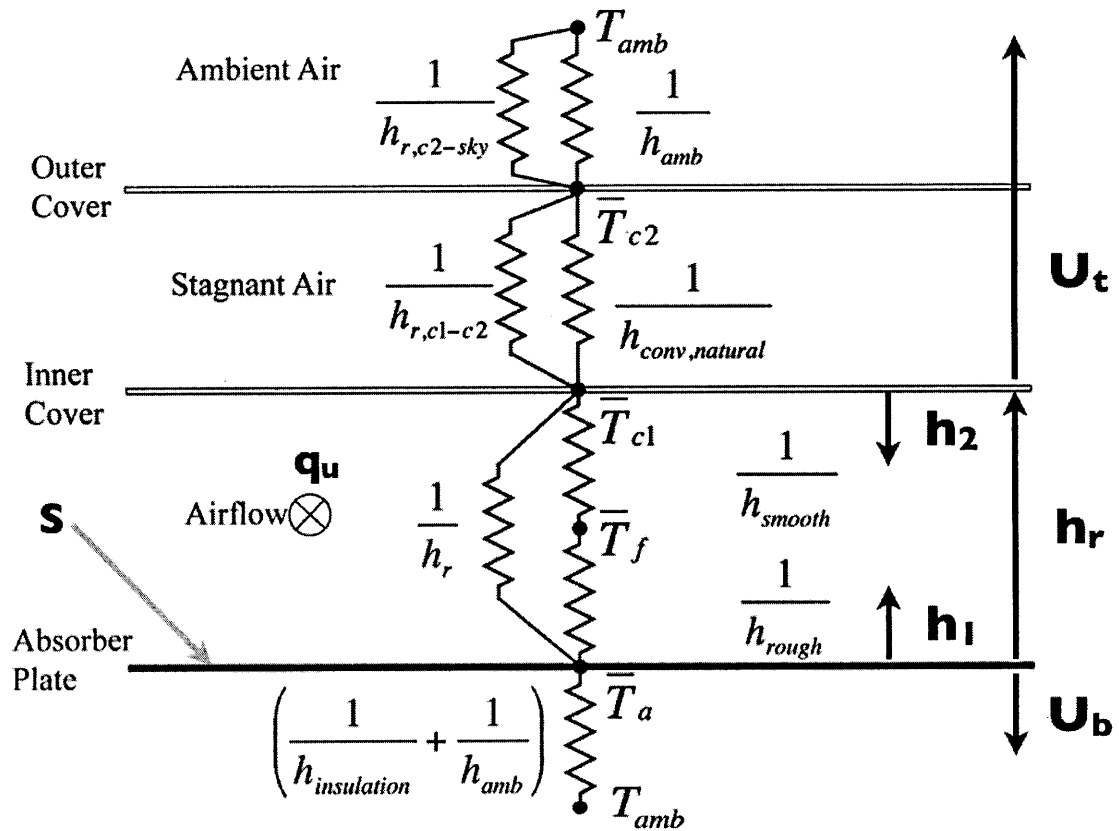


Figure 3-2: Heat transfer resistances with lumped parameters.

These lumped parameters are recommended by Duffie and Beckman [31] and shown in Figure 3-3 as an easy way to combine a network of many individual resistances.
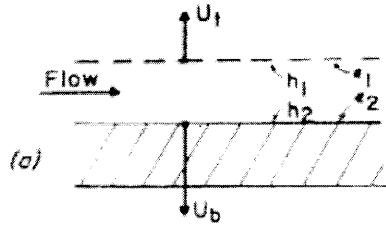
$$U_L = \frac{(U_b+U_t)(h_1 h_2+h_1 h_r +h_2 h_r)+U_b U_t (h_1+h_2)}{h_1 h_r +h_2 U_t+h_2 h_r +h_1 h_2}$$

$$F' = \frac{h_r h_1+h_2 U_t+h_2 h_r +h_1 h_2}{(U_t+h_r +h_1)(U_b+h_2+h_t)-h_r{}^2}$$

$$h_r = \frac{\sigma(T_1^2+T_2^2)(T_1+T_2)}{\dfrac{1}{\epsilon_1}+\dfrac{1}{\epsilon_2}-1}$$

Figure 3-3: Figure 6.14.1a from Duffie and Beckman showing lumped parameter air heater model and equations for total loss coefficient $U_L$, loss factor $F'$ and radiation transfer coefficient $h_r$

These lumped parameters can the be defined in terms of the individual heat transfer resistances that are shown in Figure 3-2. If three control volumes are taken around the glazings, absorber and airstream, and the heat flows between the control volumes are balanced; Equation 3.1 is obtained.

$$U_t(T_{amb} - T_{c1}) + h_r(T_a - T_{c1}) + h_1(T_f - T_{c1}) = 0 \qquad (3.1a)$$

$$S + U_b(T_{amb} - T_a) + h_r(T_{c1} - T_a) + h_2(T_f - T_a) = 0 \qquad (3.1b)$$

$$h_1(T_{c1} - T_f) + h_2(T_a - T_f) = q_u \qquad (3.1c)$$

These governing equations are based on the following assumptions

- *The glazing plates are opaque to infrared radiation*: In the temperature range of the heater radiative losses will occur in the far infrared spectrum, where glass is non-transmissive.

- *The side walls are considered adiabatic*: The side walls are 1/6th the area of the bottom, and in this configuration only 3% of the total heat loss comes from the well insulated plate bottom. Therefore the will insulated sidewalls will contribute on the order of 0.5% to the overall loss, which can be neglected.

- *The properties of air are invariant in the streamwise direction and are based on an average temperature of 47 °C*: The temperature rise in the collector is not high enough to affect the air properties by more than a few percent.

- The collector is heated uniformly over its area by the sun (i.e. no shadows)

Figure 3-2 shows radiation to the same ambient air temperature as convection which is required for the use of simple lumped parameters. Duffie and Beckman [31] state that sky temperature is relatively unimportant for calculating collector performance. However this may become important as the collector is required to run hotter and radiative loss is more important. Therefore sky temperature is included in these calculations and $T_{amb}$ is defined as a sol-air temperature of the environment by Equation 3.2. A correlation [31] for sky temperature based on dew point temperature is used. The sol-air temperature is used for the total loss, despite the fact that there is no radiation from the back surface to the sky. This does not have a large effect on the loss, as the bottom loss only 3% of total loss in the baseline configuration.

$$T_{amb} = T_{air,amb} + \frac{-h_{r,c2-sky}(T_{air,amb} - T_{sky})}{h_{amb} + h_{r,c2-sky}} \tag{3.2}$$

Since the heater experiences airflow, the plate temperature varies considerably from the inlet to the outlet. Therefore it is necessary to integrate the heat loss from inlet to the outlet to obtain an accurate value.

## 3.3.2 Thermal Radiation Input, S

Thermal radiation input is calculated separate from the heat loss and lumped into one parameter which defines the heat input of the collector per unit area of exposed surface. The relations in this section were derived from Chapter 5 of Duffie and Beckman [31] based on their models for transmission of solar radiation through glazing surfaces.

First, the input angle of the radiation, $\theta_I$, needs to be established. This is defined by Equation 3.3:

$$\theta_I = |\phi - \delta - \theta_{tilt}| \tag{3.3}$$

The tilt angle should be optimized so that the sun shines as directly as possible into the collector. Of course this is only optimal at one time as the solar incidence angle changes throughout the day and throughout the year. For the case of this study, the collector is being operated at the reference location (Saudi Arabia) in mid-July, and a constant tilt angle was chosen, as seen in Table 5.2.

Knowing the incidence angle it is possible to define the entrance angle, $\theta_E$, using the index of refraction $n$, and solar incidence angle $\theta_I$

$$\theta_E = \arcsin \frac{\sin(\theta_I)}{n} \tag{3.4}$$

Then the orthogonal and parallel components of the received radiation can be found:

$$r_{pll} = \frac{\sin^2(\theta_E - \theta_I)}{\sin^2(\theta_E + \theta_I)} \tag{3.5a}$$

$$r_{orth} = \frac{\tan^2(\theta_E - \theta_I)}{\tan^2(\theta_E + \theta_I)} \tag{3.5b}$$

Next the absorptivity of the glazing needs to be found:

$$\alpha_g = 1 - \exp\left(\frac{-K_{ext}t_g}{\cos(\theta_E)}\right) \tag{3.6}$$

Now that the basic transmittance, reflectivity, and absorptivity quantities of the glazing are now calculated:

$$\tau_{orth} = \frac{(1 - \alpha_g)(1 - r_{orth}^2)}{1 - (r_{orth}(1 - \alpha_g))^2} \tag{3.7a}$$

$$\tau_{pll} = \frac{(1 - \alpha_g)(1 - r_{pll}^2)}{1 - (r_{pll}(1 - \alpha_g))^2} \tag{3.7b}$$

$$\rho_{s,orth} = r_{orth}(1 + ((1 - \alpha_g)\tau_{orth})) \tag{3.7c}$$

$$\rho_{s,pll} = r_{pll}(1 + ((1 - \alpha_g)\tau_{pll})) \tag{3.7d}$$

$$\alpha_{orth} = \alpha_g \frac{1 - r_{orth}}{1 - r_{orth}(1 - \alpha_g)} \tag{3.7e}$$

$$\alpha_{pll} = \alpha_g \frac{1 - r_{pll}}{1 - r_{pll}(1 - \alpha_g)} \tag{3.7f}$$

So far all these equations are for a single glazing. Since the baseline design has two glazings these components must be combined to find the overall transmissivity and reflectivity for the entire glazing system which is given in Duffie and Beckman [31]. When both glazings are the same material, the equations reduce to:

$$\tau_{stack} = \frac{1}{2}\left[\frac{\tau_{orth}^2}{1 - \rho_{pll}^2}\right] \tag{3.8a}$$

$$\rho_{stack} = \frac{1}{2}\left[(\rho_{orth} + \tau_{stack}\rho_{orth}\tau_{orth}) + (\rho_{pll} + \tau_{stack}\rho_{pll})\right] \tag{3.8b}$$

Knowing the transmissivity and reflectivity of cover system, the transmittance-absorptance product can now be found. This is a number less than 1 gives the fraction of solar radiation acting as the heat input into the collector. The transmittance-absorbtance product is defined by Equation 3.9.

$$(\tau\alpha) = \frac{\tau_{stack}\alpha_a}{1 - (1 - \alpha_a)\rho_{stack}} \tag{3.9}$$

After the transmittance-absorbance product is calculated $S$ is found by: $S = (\tau\alpha)I$, where $I$ is the incident direct solar radiation. $S$ has units of W/m$^2$.

## 3.3.3 Radiative Loss Model

The radiative loss model was based on a 1D resistance model for thermal radiation between the absorber and the sky. Each of the plates was modeled as a finite two dimensional object with a finite spacing between them the side walls were modeled as finite size two dimensional objects perpendicular to the plates. In order to calculate the radiation resistance view factors were calculated for each of the objects. The view factor equations were obtained from Table 10.3 of *A Heat Transfer Textbook* by Lienhard and Lienhard [34]. A schematic diagram of the overall resistance model is provided in Figure 3-4.
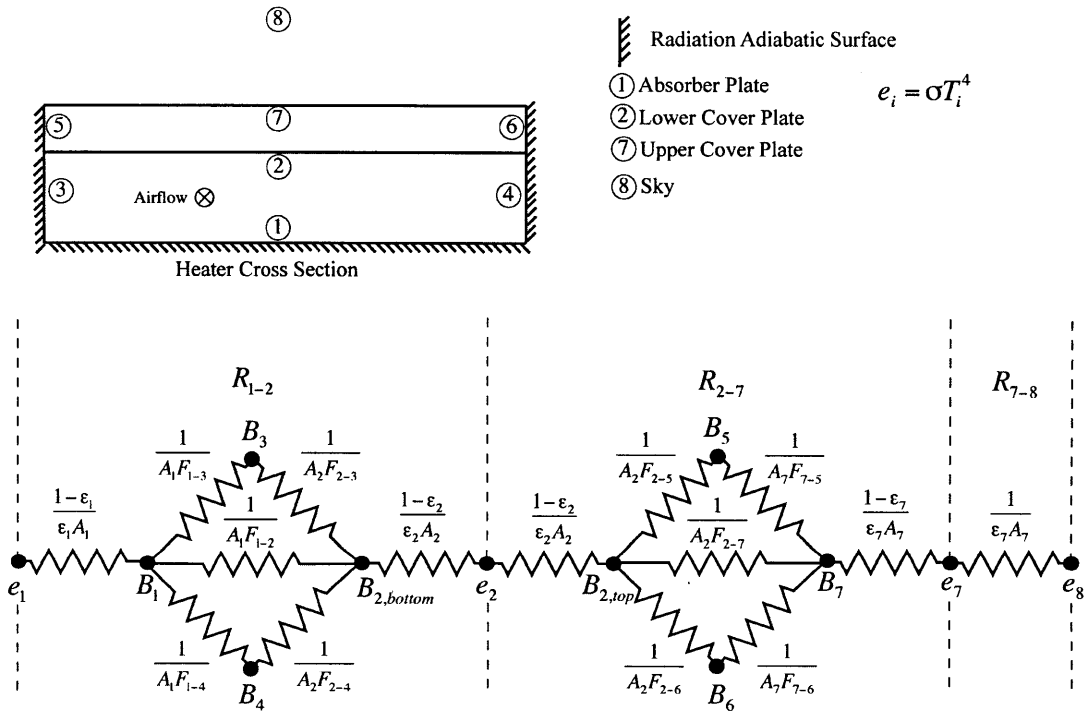


Figure 3-4: Thermal radiation resistance diagram showing total radiation resistances between each plate.

Heat flows from the absorber, $e_1$, to the sky, $e_8$, through the resistance network shown, where $A_i$ is the area of surface $i$ and $F_{j-k}$ is the view factor between surfaces $j$ and $k$. The heat flow between two surfaces is $q_{j_k} = (e_j - e_k)/\sum R_i$. The walls at surfaces 3-6 are adiabatic and radiation does not flow out of the back of the absorber plate. However, the absorber radiate upward. The resistance factors ($R_{1-2}$,

$R_{2-7}$, $R_{7-8}$) in Figure 3-4 are radiation heat transfer resistances, which are calculated from the resistors in the schematic diagram, using resistor network rules. They are then used in a linearized heat transfer coefficient. Using the identity $(T_j^4 - T_k^4) = (T_j - T_k)(T_j^2 + T_k^2)(T_j + T_k)$ a simple temperature difference can be factored out such that $q_{jk} = h_{rad}(T_j - T_k)$. and a temperature dependent radiation heat transfer coefficient can be calculated:

$$h_{rad} = \frac{1}{A} \frac{\sigma(T_j^2 + T_k^2)(T_j + T_k)}{\sum R_i} \tag{3.10}$$

$A$ is the the area of the surfaces in question, which is the same for both surfaces in the case of this type of solar collector. Since $\sum R_i$ contains the area of the plates, it must be divided out for $h_{rad}$ to have the correct units of $W/m^2 K$.

Since the radiation heat transfer coefficient is temperature dependent it is necessary to guess the plate temperatures and solve for them by iteration.

### 3.3.4 Convective Heat Transfer in the Flow Channel

Convective transfer in the flow channel is driven by forced convection. Flow through the channel is characterized by the mass flow rate, channel hydraulic diameter, and a Reynolds number based on that diameter. These quantities are defined in Equation 3.11:

$$d_h = \frac{4A_{chan}}{2(d_{chan} + w_{chan})} \tag{3.11a}$$

$$Re_{d_h} = \frac{\dot{m} d_h}{\mu A_{chan}} \tag{3.11b}$$

Approximating the airflow channel as a tube with diameter $d_h$, the Gnielinski correlation for the heat transfer of turbulent flow in a smooth tube can be used. Equation 3.12 gives relations for the friction factor, $f$, the Nusselt Number, $Nu$, and resulting heat transfer coefficient. Turbulent flow is maintained at all points in the collector as it helps the air in the channel remain well mixed and ensures good heat

transfer to the air. Furthermore it also reduces the thermal entry length so that at the slowest mass flow rate used in this study the Nusselt number is within 20 percent [35] of the fully developed Nusselt number within 60 cm of the channel.

$$f = (1.82 \log(Re_{d_h}) - 1.64)^{-2} \tag{3.12a}$$

$$Nu = \frac{(f/8)(Re_{d_h} - 1000)Pr}{1 + 12.7(f/8)^{\frac{1}{2}} \left(Pr^{\frac{2}{3}} - 1\right)} \tag{3.12b}$$

$$h_s = \frac{Nuk}{d_h} \tag{3.12c}$$

### 3.3.5 Rough Surface Convective Heat Transfer

The previous chapter demonstrated that roughening the absorber plate enhances heat transfer into the air by a considerable amount. This works as surface roughness breaks up the laminar boundary layer increasing mixing of the air and placing more of the air in contact with the hot absorber in a given amount of time.

The surface was modeled as having transverse rib roughening using the correlations developed by Dalle Donne and Meyer [36]. Ribs were used on the absorber at a low rib height and optimal spacing, resulting in a fully rough surface, with parameters given in Table 3.3.

Table 3.3: Roughening parameters.

| Roughening Parameters | Value |
|---|---|
| Rib Height, $h_{rib}$ | 0.0032 m |
| Rib Pitch, $p_{rib}$ | 0.02 m |
| $p_{rib}/h_{rib}$ | 6.3 |
| Roughening Regime | Fully Rough |

The sand grain roughness [36] of such a surface is described by Equation 3.13:

$$k_s = h \exp\left[3.4 - 3.7(p_{rib}/h_{rib})^{-0.73}\right], \ 2 < (p_{rib}/h_{rib}) < 6.3 \tag{3.13a}$$

$$k_s = h \exp\left[3.4 - 0.42(p_{rib}/h_{rib})^{0.46}\right], \ 6.3 < (p_{rib}/h_{rib}) < 20 \tag{3.13b}$$

This sand grain roughness can be used in Equation 3.14 to find the roughened pipe friction factor.

$$f_r = \left[-2.0\log\left(\frac{2k_s}{7.4d_h}\right) - \frac{5.02}{Re}\log\left(\frac{2k_s}{7.4d_h} + \frac{13}{Re}\right)\right]^{-2} \tag{3.14}$$

Along with correlations for sand grain friction, dimensionless constant, $g_r$, is required to calculate the Stanton number to obtain the heat transfer coefficient. $g_r$ requires the calculation of a characteristic velocity and non-dimensional rib height. These relations were taken from Table 4.9 of Mills [35] and are defined in Equation 3.15

$$V = \frac{m_{dot}}{\rho_{air}A_{chan}} \tag{3.15a}$$

$$h^+ = \frac{Vh_{rib}}{\nu}\left(\frac{f_r}{8}\right)^{1/2} \tag{3.15b}$$

$$g_r = 4.3h_{rib}^{0.28}Pr^{0.57} \tag{3.15c}$$

The more general form of $g_r$ in Equation 3.15c was used to maximize the range of rib heights and pitches that could be used in the analysis. This is not the most accurate form of the equation, but high accuracy is not needed since this is a more broad analysis of air heater performance.

Next the Stanton and Nusselt numbers can be calculated for obtaining the heat transfer correlation. This is given in Equation 3.16:

$$St = \frac{f/8}{0.9 + (f/8)^{1/2}(g_r - 7.65)} \tag{3.16a}$$

$$Nu = StRePr \tag{3.16b}$$

53

A rough surface heat transfer coefficient is then calculated from the Nusselt in the same way as done in Equation 3.12c.

## 3.3.6 Natural Convection Between The Cover Plates

The glazing plates contain a layer of stagnant air between them that is circulated around by natural convection as the plate temperatures are different. Correlations for natural convection heat transfer between two inclined plates are given by Duffie and Beckman [31]. The correlation is given by Equation 3.17

$$Nu = 1 + 1.44 \left[ 1 - \frac{1078(\sin 1.8\theta_{tilt})^{1.6}}{Ra \cos \theta_{tilt}} \right] \left[ 1 - \frac{1708}{Ra \cos \theta_{tilt}} \right]^{+} + \left[ \left( \frac{Ra \cos \theta_{tilt}}{5830} \right)^{1/3} - 1 \right]^{+} \tag{3.17}$$

The plus exponent indicates that only positive vales of the expression in brackets are to be used, otherwise the value in brackets is set to zero. The Rayleigh number, $Ra$, is defined by equation 3.18:

$$Ra = \frac{g\beta(T_{c1} - T_{c2})d_{sep}^3}{\nu_a \alpha_a} \tag{3.18}$$

In the case of air, or an ideal gas, the thermal expansion coefficient which is just the inverse of the average of the plate temperatures in Kelvin. Unlike the other convection heat transfer coefficients, this one is dependent on temperature; therefore it is required that $T_{c1}$ and $T_{c2}$ are known.

## 3.3.7 Other Losses

The final convective loss is that of the warm cover plates and lower insulation to the outside air. This is calculated using a constant wind speed and laminar heat transfer coefficient. A Reynolds number, $Re_{l_c}$ is calculated based on the wind speed, $V_{amb}$,

and characteristic length $l_c$, which is the overall length of the collector. The average Nusselt number for laminar forced convection heat transfer is given by Equation 3.19:

$$\overline{Nu} = 0.644 Re_{l_c}^{1/2} Pr^{1/3} \qquad (3.19)$$

The thickness of the insulation on the bottom plate also has a heat transfer coefficient, which is based on pure conduction through a solid, with conductivity $k_{ins}$ and thickness $t_{ins}$:

$$h_{ins} = \frac{k_{ins}}{t_{ins}} \qquad (3.20)$$

## 3.4 Solving The Model

To calculate the final energy output and efficiency of the collector the governing equations in Equations 3.1a and 3.1b can be used to calculate the temperatures of all other surfaces in terms of the fluid temperature, $T_f$. The useful heat gain, $q_u$, is calculated from Equation 3.21.

$$\frac{dT_f}{dx} \frac{\dot{m}c_p}{w_{chan}} = q_u \qquad (3.21)$$

This can be equated to Equation 3.1c and integrated along the stream wise direction to obtain the temperature profile in Figure 3-5. The temperature-dependent heat transfer coefficients are calculated at each step $dx$ along the length to obtain an accurate picture of the heat transfer.
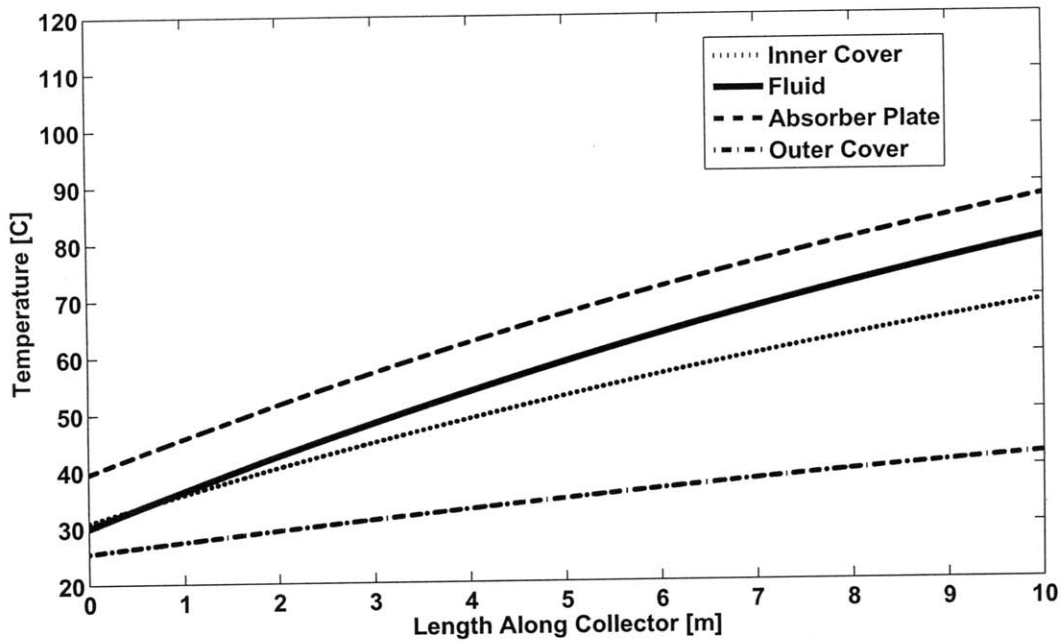
Figure 3-5: Variation of temperature along the length of the collector in the stream-wise direction.

The useful heat gained by the collector can be easily calculated once the fluid outlet temperature is known:

$$q_u = \dot{m}c_p(T_{in} - T_{out}) \tag{3.22}$$

The collector efficiency can be calculated with Equation 3.23

$$\eta = \frac{q_u}{I_T A_p} \tag{3.23}$$

This equation takes similar form to Equation 2.1 when the expression for $q_u$ is substituted into the numerator.

This, however is a very computationally intensive method, especially when the performance effects of many changes in a material property need to be calculated. To speed up computation the code makes use of analytical integrated solutions from Duffie and Beckman [31]. These solutions rely on using average temperatures for each component, which results in the same solution as using local temperatures and

56

integrating when the collector has no heat capacity.

First, through algebraic manipulations, and total heat loss coefficient, $U_L$, and efficiency factor, $F'$, are calculated. For this type of heater the expressions are shown in Figure 3-3. $U_L$ represents the heat transfer coefficient for the heat loss between the absorber plate temperature and the ambient, such that $Q_l = U_L(\bar{T}_a - \bar{T}_{amb})$. The efficiency factor represents the ratio of the actual heat lost to the heat lost if the entire absorber was at the airstream temperature, which would result in the minimum heat loss.

Once the total loss coefficient and efficiency factor are calculated, a heat removal factor is found by stream-wise integration. The heat removal factor is akin to a heat exchanger effectiveness as it represents the ratio of heat transfer to the air to the maximum amount of heat transfer to the air if the the entire absorber was at the air inlet temperature:

$$F_R = \frac{m_{dot}c_p}{A_p U_L} \left( 1 - \exp\left( \frac{-A_p U_L F'}{m_{dot}c_p} \right) \right) \tag{3.24}$$

A simple first law analysis using the entire heater as a control volume the total useful heat per unit exposed area, $q_u$, is found. As the absorber plate temperature is now known it is necessary to guess an absorber plat temperature and iterate.

$$q_u = \left( S - U_L(\bar{T}_{a,guess} - \bar{T}_{amb}) \right) \tag{3.25}$$

Since this is based on a guessed temperature the actual plate and fluid temperatures have to be recalculated with the heat removal factor $F_R$:

$$\bar{T}_a = \bar{T}_{amb} + \frac{q_u}{F_R U_L}(1 - F_R) \tag{3.26}$$

Once a new plate temperature is found then the heat loss can be recalculated according to Equation 3.25 now using the new absorber plate temperature. The first law was then used to calculate a overall heat loss through the top of the heater, $Q_l$ using Equation 3.27.

$$Q_l = A_P(S - q_u) - A_p U_b(T_a - T_{amb}) \qquad (3.27)$$

which can then be used to back out the new glazing plate temperature temperatures, also by applying the first law.

Because it takes several iterations to converge on a final temperature, this whole process needs to be repeated adjusting the guessed temperature at each step to be closer to the correct temperature. All temperature dependent heat transfer coefficients need to be recalculated at every iteration as well. The new guess temperature is adjusted to be 75% of the old guessed temperature, $\bar{T}_{a,guess}$ and 25% of the new plate temperature $\bar{T}_a$. This ensures that the iteration did not become unstable. The final temperature is then found when the $\bar{T}_a$ was within 0.01 K of the previous $\bar{T}_{a,guess}$

Once a final plate temperature is converged upon the useful all the calculations in this section are repeated with the new plate temperature $\bar{T}_a$. All the calculations for the temperature dependent heat transfer coefficents are repeated as well using the final temperatures found for the cover plates.

Knowing the heat loss and useful heat gain, a collector efficiency is calculated with Equation 3.23.

## 3.5    Sensitivity Analysis Results

The sensitivity study investigates the effect of various material properties on performance of the collector, as well as how environmental conditions affect performance when certain materials are used.

### 3.5.1    Material Properties

The material properties that have the greatest impact on performance are the infrared emissivities of the glazing and absorber plates, the glazing stack solar transmissivity, and absorber solar absorptivity. Figure 3-6 shows the relative effect of each parameter

as it is varied from 0 to 1. The operating point was based on the operation of an HD cycle in a desert environment. For the 10 m long collector a normalized gain of 0.06 K m$^2$/W is obtained at a mass flow rate of 0.029 kg/sec (104 kg/hr). The calculations assume that the conduction resistances of the glazings and absorber are negligible, owing to their small thickness. Heater dimensions can be optimized for the desired temperature rise, and optima are easily found for the dimensions of roughness features or spacing between the plates, and will not be discussed here.
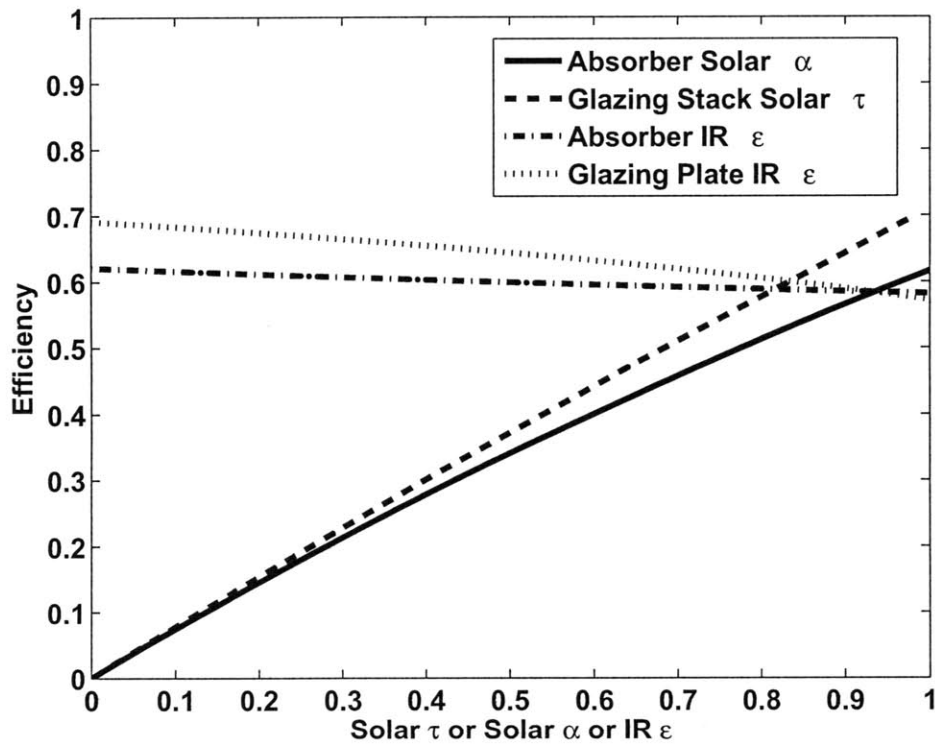


Figure 3-6: Effect of emissivity, absorber absorptivity, and glazing transmissivity on efficiency.

The graph shows that the two most important parameters are absorber solar absorptivity, and the glazing solar transmissivity. Using an absorber with a selective coating ($\alpha = 0.9$-1, $\epsilon = 0.02$-0.3) [23] does not offer significant performance gains with only a 4% efficiency improvement. This is typically a very expensive design addition, as selective surfaces are often made of exotic materials, such as quartz, can involve

expensive manufacturing processes, and are limited to only a few substrates. Using a low $\epsilon$ coating for the glazing plates offers a larger improvement of 10%, but also can be an expensive addition due to materials and manufacturing processes used.

To ascertain the efficiency "value" of various design attributes, heaters were simulated in different configurations, adding various design improvements onto a collector with a smooth, non-selective absorber with a single glazing. As can be seen from Figure 3-7 the addition of surface roughness increases performance by the greatest amount in the HD operating range. A typical value for a fully roughened surface using the parameters in Table 3.3 can increase the heat transfer coefficient 8 times over that for a smooth plate. The use of a selective absorber coating ($\epsilon$=0.05) also improves performance by a small amount. For low normalized gain a selective surface does not improve performance for over a roughened absorber, although it is more important at higher temperatures where radiative losses dominate.
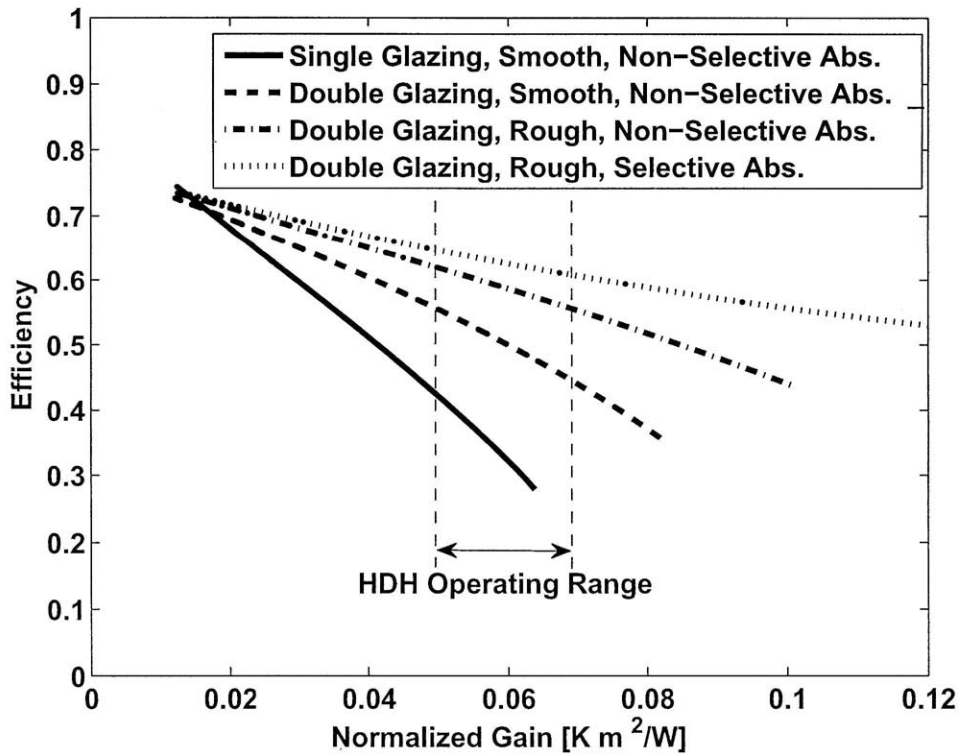


Figure 3-7: Effect of design enhancements on collector performance.

Figure 3-8 shows how the baseline design compares with existing air heaters that include Chafik's HD collector [3] and the SunMate commercial collector [29] for which the performance curve is available. It is clearly shown that the baseline collector, which incorporates all of the design enhancements beside a selective absorber, outperforms existing collectors in the HD operating range.
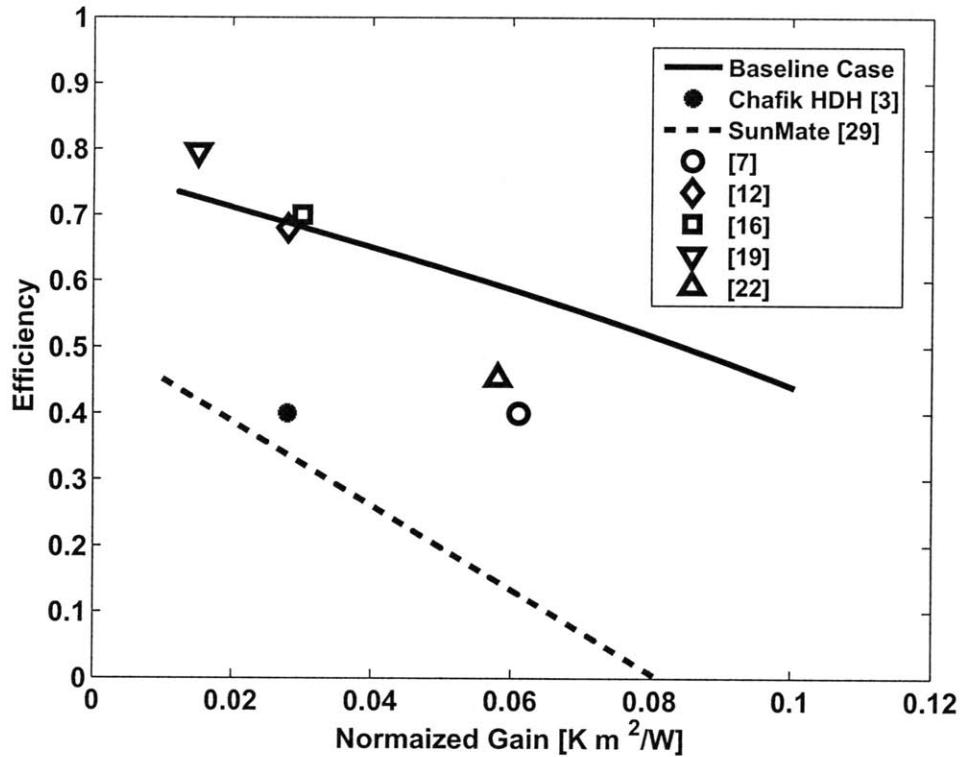


Figure 3-8: Comparison of baseline design (double glazed, rough, non-selective absorber) with existing air heaters.

## 3.5.2 Environmental Conditions

Environmental conditions also influence how a collector can be designed, and the importance of design enhancements. The environmental parameters of most importance are the ambient air temperature, the dew point temperature, which affects sky temperature, and ambient wind speed. As suggested in the literature [31], ambient air temperature has a small effect on performance when compared to ambient wind

speed. A variation in dew point temperature from -4 to 36 °C translates into a 1-2% efficiency change in the HD operating range, and a change in ambient air temperature from 0 to 40 °C translates into a 3-4% efficiency change in the HD operating range as calculated from this model.

Wind speed has a larger effect on performance. Figure 3-9 shows that wind speed can have a substantial effect on performance in the HD operating range, with an efficiency change of 10-12%. Figures 3-10 and 3-11 show the effect of wind speed on performance at varying infrared emissivities for glazing and absorber plates. The lines each represent a different wind speed from 2 m/s ($h_{amb} = 3.07$ W/m$^2$K) to 20 m/s ($h_{amb} = 39.74$ W/m$^2$K) in increments of 2 m/s. The graphs show that using low $\epsilon$ surfaces is of low importance in calm environments with only marginal improvement in windy ones.
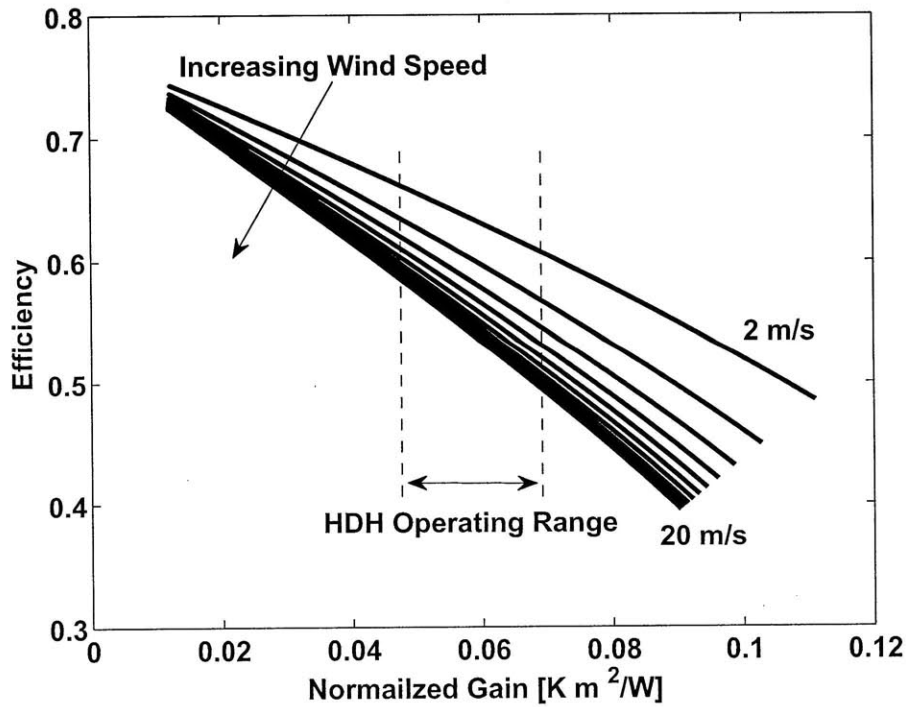


Figure 3-9: Efficiency vs normalized gain for different wind speeds.
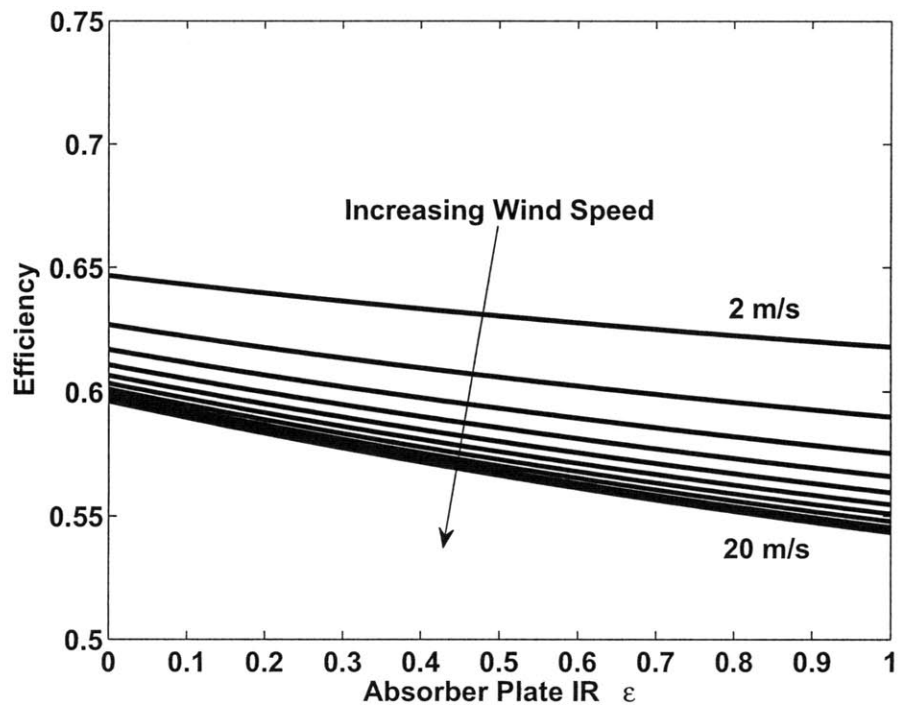
Figure 3-10: Effect of wind speed on collector performance at different absorber IR emissivity.
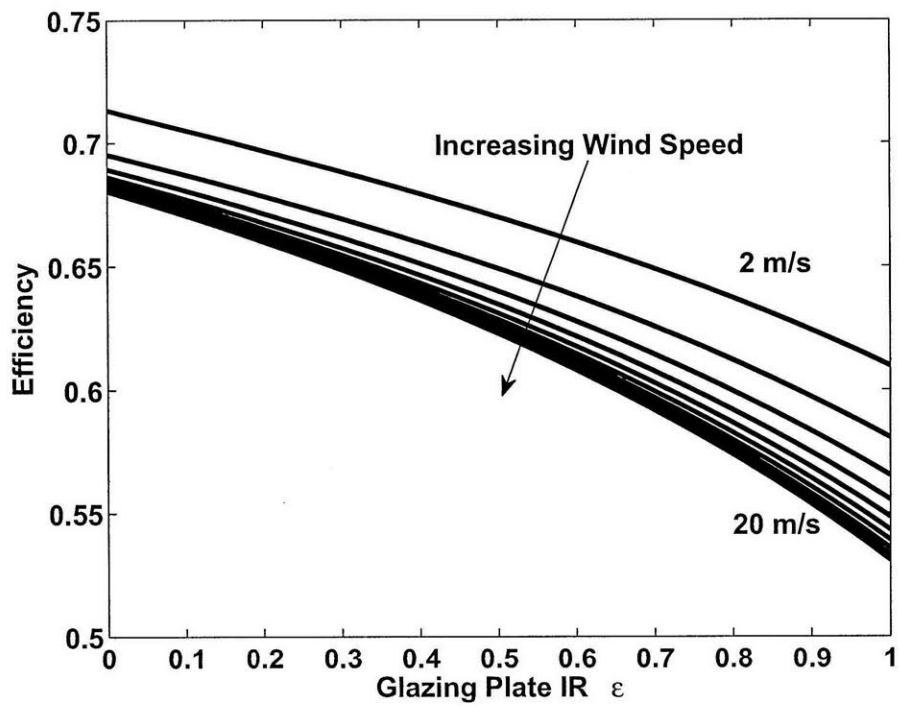
Figure 3-11: Effect of wind speed on collector performance at different glazing IR emissivity.

### 3.5.3 Other Design Attributes

Channel height also has an effect on efficiency, but must be sized in order to maintain turbulent flow through the channel. If the channel is too high the velocity goes down and the flow becomes less turbulent for a given mass flow rate, and heat transfer is poorer. However, as long as the flow remains turbulent, efficiency will not be compromised by a great deal. There also must be a minimum channel height to allow space for roughening features on the absorber plate.

Enlarging the glazing separation distance creates a larger air gap and enhances the insulating properties of the air gap. The improvements become smaller as the plate separation distance gets larger because the air layer can move more freely in convective loop defeating some of the insulation qualities of the air. However this has a negligible effect on efficiency as it only changes 1% over 40 cm of separation distance.

The bottom insulation thickness did not effect efficiency a great deal as the absorber plate was relatively cool at the baseline mass flow rate.

# Chapter 4

# Use of Polymer Materials In HD Solar Air Heaters

## 4.1   Introduction

HD Desalination requires solar air heaters to be exposed to a humid air mixture. This mixture easily corrodes metal surfaces that are not property coated. This increases replacement costs and maintenance of the collector. Low iron glass covers, while they are robust and provide good transmissivity, are often expensive and hard to procure in certain places. Therefore developing a polymer-based collector design may increase the lifetime, and decrease the cost of the collector over its life.

These components must still provide good thermal performance. As the sensitivity study indicated the most important parameters in the collector design are glazing transmissivity and absorber absorptivity. If heat transfer through the absorber is required then absorber thermal conductivity becomes important.

## 4.2   Polymer Functional Requirements

Since the HD cycle imposes unique operational constraints upon the collectors polymer materials have to meet certain basic requirements. Because of the high operating temperatures, the absorber plate must have a high working temp, above 100 °C. Glaz-

ing materials have to withstand slightly lower maximum temperatures, but those can still exceed 90 °C. The plastics also have to be chemically stable in the presence of high moisture at high temperature, which is particularly important for components in contact with the flowsteam. The external components have to be robust and able to withstand blown sand and periodic cleaning, as well being able to transmit light without degradation due to extended UV exposure.

## 4.3  Absorber Materials

Polymer choices for absorber plate materials have to be high temperature engineering plastics. The polymers considered for this application are produced by DuPont, although some older compounds are made by multiple manufacturers. New engineering plastics can withstand higher temperatures and resist UV light. They also have the advantage of being easy to fabricate into complex shapes using injection molding or thermoforming. Engineering plastics include Delrin (Acetal), Minlon (Nylon 6), Rynite PET (Polyethylene Terephthalate), Thermx PCT (Polycyclohexylene Terephthallate), Zenite LCP (Liquid Crystal Polymer) Zytel PPA (Polyphthalamide). Other polymers, like Bakelite, which belong to the thermoset family will also be considered, as they offer metal-like thermal degradation resistance and polymer corrosion resistance for a competitive price.

### 4.3.1  Maximum Working Temperature

The most important requirement of an absorber plate is operating temperature, as it is the hottest component in the system. The plastic cannot deform or become damaged at temperatures of 100 °C. Table 4.1 [37] lists the temperature it takes to deflect the material under a 1.8 MPa applied stress, which is a common material test.

Table 4.1: Maximum working temperate of absorber materials.

| Absorber Polymer | 180 MPa Deflection Temp [°C] |
|---|---|
| Acetal | 92 |
| Nylon 6 | 78 |
| PET | 200 |
| PCT (Thermx) | 240 |
| Liquid Crystal Polymer | 245 |
| PPA | 260 |
| Thermosets | N/A |

Acetal (Delrin) and Nylon 6 have operating temperatures that are too low for this application, and the material would melt if airflow over the plates failed. However, cost competitive PET and PPA have sufficiently high working temperatures.

## 4.3.2 Absorptivity

Absorptivity is the most important property of the absorber material and it is most often affected by coloring of the material as it can be imbued with carbon black or some equivalent during processing. All the materials are available in black varieties; however, materials manufacturers do not measure the solar absorptivity of the black materials. The absorptivity of a material can also be changed by a paint or coating which would enhance corrosion resistance as well. In many cases, paints, which offer a cheaper alternative to selective surfaces, have high absorptivity. Table 4.2 shows data as tabulated by NASA Goddard Space Flight Center [38]. It includes data for many coatings including some plastics.

Table 4.2: Absorptivity of materials.

| Material | Absorptivity | Emissivity |
|---|---|---|
| Anodize Black | 0.88 | 0.88 |
| Carbon Black Paint NS-7 | 0.96 | 0.88 |
| Catalac Black Paint | 0.96 | 0.88 |
| Chemglaze Black Paint Z306 | 0.96 | 0.91 |
| Aeroglaze 306/Kevlar Composite | 0.96 | 0.91 |
| CTL15 Black Gloss Paint | 0.95 | 0.87 |
| Deep Sky Black | 0.91-0.95 | 0.94 |
| Delrin Black Plastic | 0.96 | 0.87 |
| Ebanol C Black | 0.97 | 0.73 |
| Ebanol C Black - 384 ESH UV | 0.97 | 0.75 |
| E-Glass Fabric 5276 | 0.74 | 0.91 |
| GSFC MS-94 | 0.96 | 0.89 |
| GSFC NSB69-82 | 0.97 | 0.9 |
| Aeroglaze H322 | 0.96 | 0.86 |
| Aeroglaze L-300 | 0.95 | 0.84 |
| Martin Black Velvet | 0.91 | 0.94 |
| MH21S/LO Black Paint | 0.98 | — |
| NSB6982 | 0.97 | 0.91 |
| Paladin Black Lacquer | 0.95 | 0.75 |
| Polyethylene Black Plastic | 0.93 | 0.92 |
| PT401 Gloss Black Paint | 0.95 | 0.85 |
| Pyromark 1200 Black Paint | 0.95 | 0.83 |
| Tedlar Black Plastic | 0.94 | 0.9 |
| Vel-Black | 0.99 | 0.95 |

Among the materials tested are many cheap coatings like Carbon Black NS-7, as well as some plastics like Delrin, Polyethylene, and Tedlar. All these materials achieve an absorptivity around 0.95, making them excellent candidates for absorber plate materials. The black plastic materials have absorptivity that are very close to each other, within 2%.

## 4.4 Glazing Materials

Clear polymer glazings can also offer a performance advantage. Polymers used in glazings are not an entirely new concept. Chafik [3] utilized polycarbonate (PC) glazings for HD solar collectors. Ben Amara et al. (2004) [39] used untreated polycarbonate glazings for a desalination solar collector. The glazing was prone to cold spots that led to condensation in some locations and melting in others in the face

of extreme solar radiation. Polycarbonate, even if treated for UV resistance is not as hard as glass, which makes it more prone to wind damage by blown sand. Studies by Pickett et al (2004) [40] on polycarbonate exposed in Phoenix, AZ, a desert environment, found significant losses in transparency after 1 year. However coating can improve the weathering of polycarbonate as found by Schmauder et al. [41] who tested an economical hardcoating done with chemical vapor deposition. Raman et al. [42] found that coating polycarbonate with acrylic helped withstand long term exposure to UV light and heat.

### 4.4.1   Operating Temperature

First and foremost, the materials used must be able to withstand temperatures required by an HD cycle. The glazing should also withstand temperatures that would result from the airflow through the collector failing. Table 4.3 shows the maximum working temps of many materials as provided by their manufacturers [43, 44, 45, 46]. In addition to the materials mentioned above, other transparent plastics were also included.

Table 4.3: Maximum working temperatures of glazing materials.

| Glazing Material | Maximum Working Temp [C] |
| --- | --- |
| DuPont Tedlar (PVF) Film | 107 |
| Teflon (FEP) Film | 205 |
| Mylar (PET) Film | 190+ |
| Polycarbonate (GE Lexan) | 154 |
| Plexiglass (PMMA) | 50 |
| High Impact Polystyrene | 100 |

Some materials like PMMA and HIPS have operating temperatures that are too low and will not be considered further.

### 4.4.2   Transmissivity

After determining that a material has a sufficient operating temperature, its overall transmissivity needs to be compared to the best glass option, which is low-iron or

water white glass. Table 4.4 gives the solar transmissivity [31, 47, 43, 48] of all materials that have a sufficient operating temperature. The transmissivity values are for perpendicular direct radiation.

Table 4.4: Transmissivity of glazing materials in visible and near infrared.

| Material | Thickness | Transmissivity |
|---|---|---|
| High Iron Glass | 2.5 mm | 0.87 |
| Water White Glass | 2.5 mm | 0.94 |
| FEP (DuPont Teflon) | 0.025 mm | 0.96 |
| PVF (DuPont Tedlar) | 0.025 mm | 0.90 |
| Polycarbonate (Bayer Makrolon) | – | 0.88 |

Of all the materials listed, Teflon has the most comparable transmissivity to water-white glass. A major concern with plastics are that they pass infrared radiation and would therefore lose heat faster than glass, which is opaque to infrared radiation. It is therefore necessary to look at the full transmission spectra. Figures 4-1 [49], 4-2 [47], and 4-3 [48] show the transmission spectra of the best transmitting polymers. The vertical lines denote the visible range.
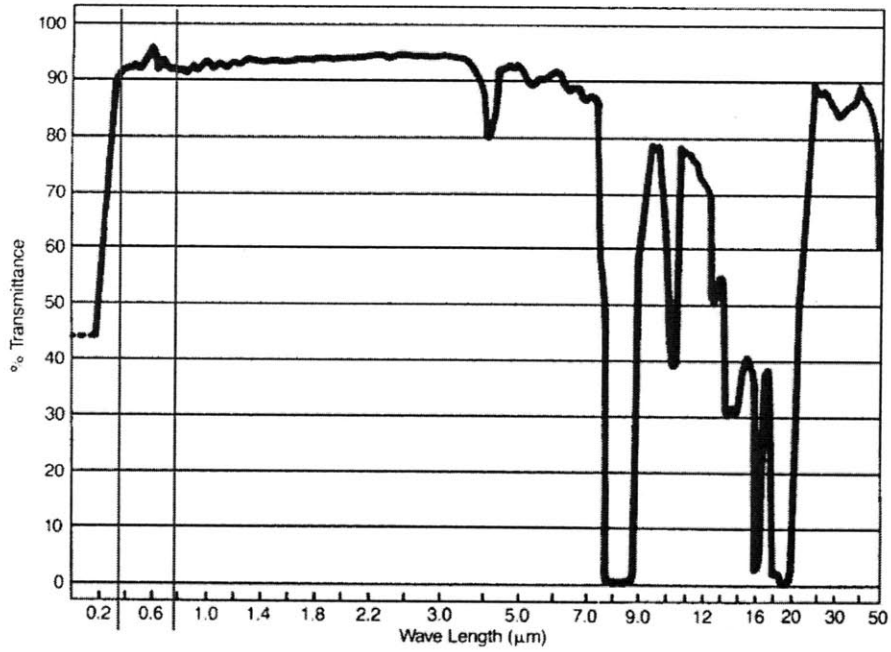
Figure 4-1: Transmission spectrum for 0.025 mm thick Teflon (FEP).
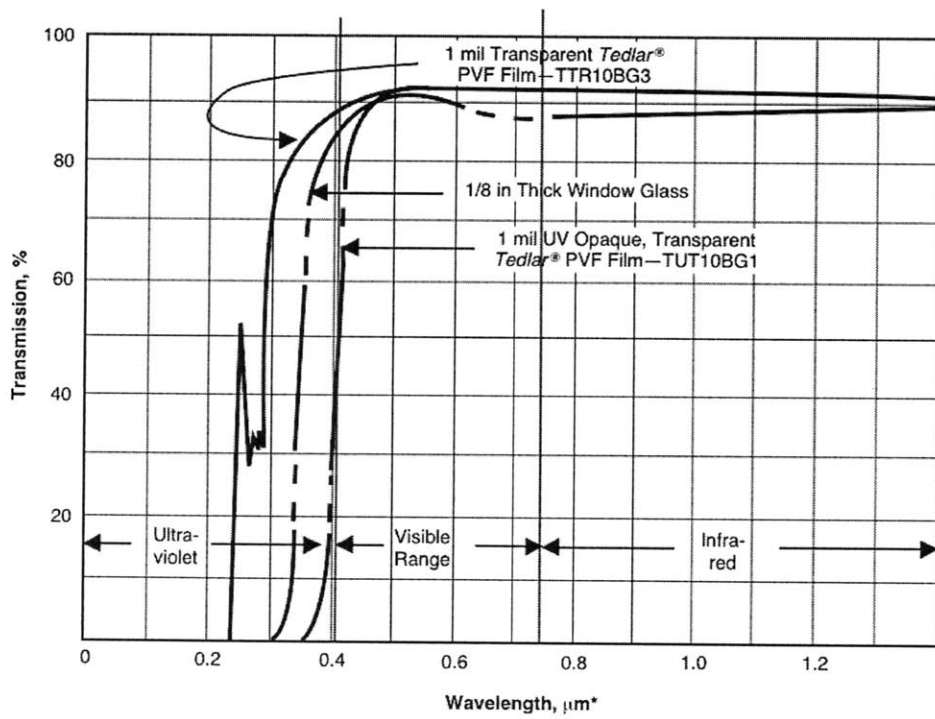


Figure 4-2: Transmission spectrum for for 0.025 mm thick Tedlar (PVF).
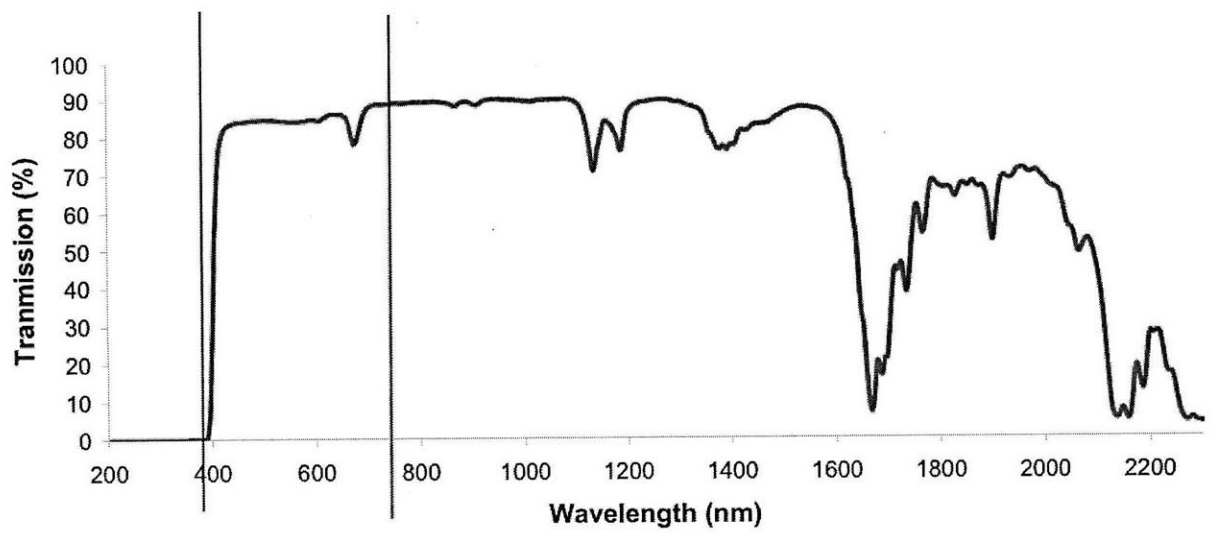
Figure 4-3: Transmission spectrum for Polycarbonate (unspecified thickness).

Of all the polymers shown, all have good transmission in the visible and near infrared ranges, which is desirable. FEP transmission drops off in the far infrared, but is high for select wavelengths, making it less desirable then glass. Polycarbonate drops off in far infrared more than FEP. Data for the far infrared spectrum for PVF was not available.

Optically, Teflon film or FEP is a superior choice for glazing materials. It however is bound by certain practical constraints. It is a thin film material, and would not hold up well to blown sand and mechanical cleaning.

### 4.4.3 Practical Considerations

In addition to sustained exposure to the sun, materials have to work within the practical constraints of an HD cycle. Currently, no data was found on exposure to brine on the inside or outside of a solar collector, as using solar air heating for desalination is not widespread. However, other data has been found that would be relevant to materials in an HD application. Polycarbonate has significant hydrolytic degradation problem at temperatures over 60 °C as noted by Ghorbel et al.[50]. This degradation results in carcinogenic chemicals being released into the air stream, which would exclude polycarbonate from being used as the inner glazing. The outer glazing also has to withstand mechanical cleaning, as dust buildup significantly hinders performance. Hegazi [51] found that transmissivity decreases by 15% over 30 days of exposure. These test were done in Minia, Egypt, a similar environment as where an HD system would be employed. This fact eliminates thin films for use as an outer glazing.

## 4.5 Cost Analysis

Since cost of the solar collectors is a major component the overall HD system cost, it must be considered first when looking at polymers for collector materials.

Polymer materials with good thermal performance tend to be expensive. However plastics are lighter and easier to fabricate than metals, and are also resistant to corrosion that would occur if metals were exposed to a humid air stream. Plastics

also have different mechanical properties than metals. They are less stiff, necessitating a thicker plastic surface where a metal surface might be thinner and still work in the same application. However, plastics are generally lighter than metals and therefore require less mass of material for the same dimensions. Therefore it was necessary to compare the cost of different materials normalized to a single stiffness, which would take the mechanical properties into account. To do this a plate with cross-sectional dimensions $w$, $t$ was cantilevered at both ends of its length, $L$, and its thickness adjusted to equal a certain stiffness. Stiffness was normalized to 3.175 mm thick steel plate of the same dimensions and configuration, and calculated by Equation 4.1

$$K = C\frac{EI}{L^3} \tag{4.1}$$

where $K$ is the stiffness in N/m, $C$ is a constant depending on the type of mounting of the plate, $E$ is the Young's Modulus and I is the moment of inertia, given by Equation 4.2:

$$I = \frac{wt^3}{12} \tag{4.2}$$

For evaluating the materials considered here the dimensions of the standard collector design used in the previous chapter were used. These are $L = 10$ m, $w = 0.3$ m. A plate cantilevered at both ends has a constant C = 384. Material properties including density and Young's modulus data were taken from *Materials Selection in Mechanical Design* by Ashby [52].

Once required stiffness is specified it can be plugged back into Equations 4.1 and 4.2 to get the thickness required for each type of material, or $t_{rqd}$. This thickness can be used to determine the cost of an absorber or glazing of the required stiffness

$$Cost_{norm} = \frac{Cost_{bulk}}{\rho}\frac{wt_{rqd}L}{A_p} = \frac{Cost_{bulk}}{\rho}t_{rqd} \tag{4.3}$$

$Cost_{bulk}$ is the bulk material cost in \$/kg which was obtained from market sources [53, 54, 55, 56, 57, 58, 59], $\rho$ is the material density, and $A_p$ is the plate area. Since $A_p = wL$ the equation can be simplified to the second form. These calculations allow

76

a comparison of cost per meter squared of surface area in the collector and is shown in Table 4.5.

Table 4.5: Bulk materials cost per square meter - stiffness normalized.

| Material | cost/m$^2$ low | cost/m$^2$ high |
|---|---|---|
| **Absorber Polymers** | | |
| Acetal | $49.09 | $60.42 |
| Nylon 6 | $36.13 | $152.55 |
| PET | $15.15 | $57.58 |
| PCT (Thermx) | - | - |
| LCP | $227.94 | $325.64 |
| PPA | $17.40 | $56.12 |
| Thermosets | $20.57 | $68.56 |
| **Glazing Polymers** | | |
| PC | $23.53 | $75.91 |
| PVF | - | - |
| PET | $12.95 | $49.20 |
| HIPS | $10.33 | $76.75 |
| FEP | - | - |
| | | |
| **Metals and Glass** | | |
| Steel | $21.62 | $21.62 |
| Aluminum | $18.43 | $18.43 |
| Copper | $113.01 | $113.01 |
| | | |
| Glass | $15.54 | $39.24 |

High temperature materials for which no cost data exist are very new and proprietary to DuPont. As a result cost on the open market is unavailable, and DuPont does not release costs for research purposes. It can be assumed that these plastics cost significantly more than ones for which cost data was available. This table does not represent the cost to make a stiff plastic coated metal surface or a structurally supported metal surface that uses even less of the more expensive materials, but which might have superior mechanical properties. Polymer materials with enhancements, like UV resistance, will be on the higher end of the scale.

As the numbers show, plastics are closely priced to metals and glass, with the exception of copper. Copper is unlikely to be used as air is not flowing under the absorber which would require high thermal conductivity. However, no cost data is available for the high performing plastic films, like PVF and FEP. These materials

are bound to be very cost effective because of the small amount of material required.

## 4.6 Conclusion

The high service temperature in a solar air heater means that the choice of plastic resins is limited. The best choice for absorber plate plastic would be Rynite (PET). Rynite is not a thermoset, so roughening features can be easily formed into it. It also comes in black varieties for maximum absorptivity.

For the glazing material a combination of materials could be used. For the upper surface a low iron glass could be used due to its resistance to UV degradation, and superior stiffness and resistance to damage by blown sand. A Teflon (FEP) film could be used for the inner layer. The FEP film would have to be taut enough to avoid fluttering as air flows through the channel. It is important to note that because glass does not corrode in the presence of moist air, it will most likely be the cheapest option with very high performance.

# Chapter 5

# Solar Air Heater With Built-In Energy Storage

## 5.1 Introduction

Solar water heaters have been thoroughly investigated and developed commercially [60, 61, 62] whereas there has been relatively little investigation and almost no commercial development of solar air heaters. In the context of Humidification-Dehumidification (HD) desalination, heating the air as opposed to the water stream leads to significant performance gains [63].

Chapter 3 investigated the performance of air heaters at steady state and showed improved performance over current designs; however, this analysis did not take into account the transient nature of solar irradiation throughout the day from sunrise to sunset.

Energy storage is an important aspect of collecting intermittent energy like that from the sun, especially for applications like HD desalination in which a stable warm temperature is needed for optimum performance. The goal of a properly optimized storage system is to deliver heat at an approximately constant temperature throughout a 24 hour day. Heating at a constant temperature also provides more stability to the HD system and increases performance over time [64]. This avoids startup effects in the morning as well as energy loss when the cycle top temperature drops at night.

## 5.2 Comparison of Performance

Chapter 3 the performance of solar air heaters was compared using the collector efficiency. This was an instantaneous power efficiency that was applicable to a collector with no heat capacity effects running in steady state with constant solar irradiation. Since this study concerns time varying radiation, which is zero at night, a time averaged value of efficiency will be used as defined by Equation 5.1:

$$\eta = \frac{\int_{t_1}^{t_2} \dot{m} c_p [T_{out}(t) - T_{in}]\, dt}{\int_{t_1}^{t_2} I A_p\, dt} \tag{5.1}$$

This definition of performance is the time average of the efficiency is used in the ASHRAE 93-2003 Standard for solar collector testing [4] and is similar to the one in Chapter 2 for instantaneous efficiency.

Additionally, to evaluate normalized gain over a period of time during which the solar irradiation may be zero (i.e., night), a time averaged normalized gain is defined by Equation 5.2:

$$NG = \frac{\int_{t_1}^{t_2} [T_{out}(t) - T_{in}]\, dt}{\int_{t_1}^{t_2} I\, dt} \tag{5.2}$$

## 5.3 Built-in Energy Storage

In this design, as shown in Figure 5-1, a phase change material (PCM) is placed below the absorber plate in direct contact with the absorber. This allows heat to be transfered directly from the absorber plate to the storage medium and then directly from the storage medium to the air when the sun is not shining. This eliminates the need for a separate apparatus and control systems for external storage as well as the associated heat losses. Additionally the low heat capacity working fluid is not used to transfer heat to the storage. Using a built-in storage system also eliminates the need for a secondary working fluid loop and the inherent increase in complexity and

cost.
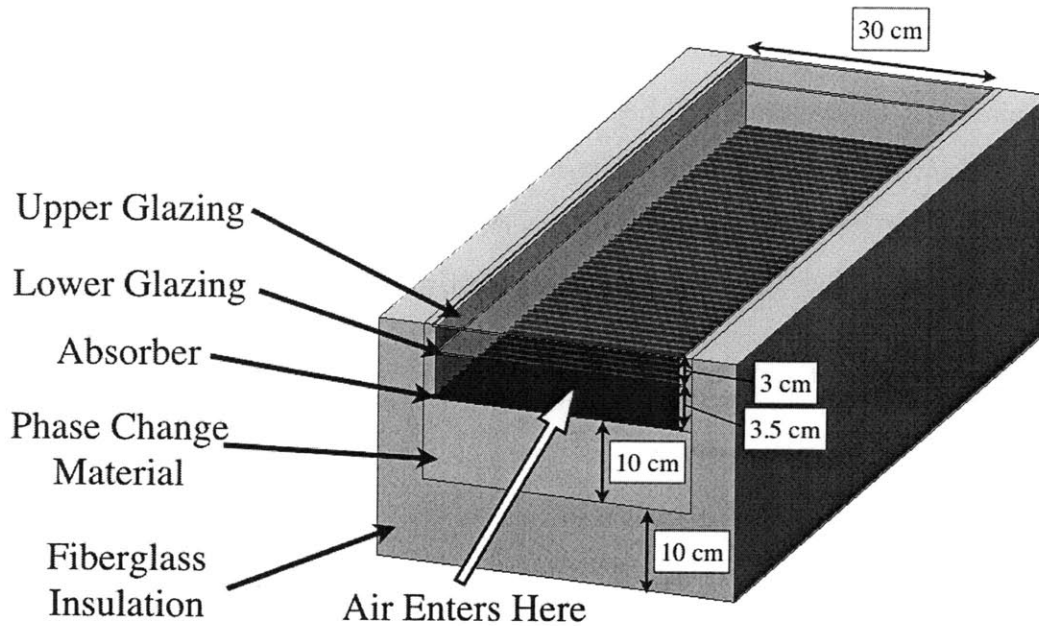


Figure 5-1: Schematic drawing of collector with storage.

The use of a PCM as the storage medium stabilizes the output temperature of the collector by storing heat near the melting temperature. A PCM can store 100 times more heat than a comparably sized sensible heat storage system. Therefore less material is required to store the same amount of heat. The smaller volume also reduces the need for high contact area or a high thermal conductivity in the storage material.

## 5.3.1 Existing Built-in Storage Collectors

Built-in energy storage has commonly been used for solar energy storage. Water heaters have used built-in storage for many years. Early water heaters [65] took advantage of the sensible heat storage in the water itself and made insulated tanks that held hot water heated by the sun during the day and used at night. Garg [66]

evaluated the performance of one of these heaters by varying the water tank depth. He found that water at 60°C was available after 5 PM even in winter.

In other instances a phase change material was used as part of a water tank to augment the storage capacity of water. Prakash et al. [67] used paraffin wax encapsulated at the bottom of a heated flat plate over the water tank. Kumar [68] used a tank of paraffin wax which absorbed solar radiation, and heat was removed by water flowing through three finned heat exchangers. In some cases, water flowed through pipes between an absorber surface with integrated phase change material. Rabin et al. [69] used a a configuration where pipes carrying water were placed in an oil that floated on top of a more dense salt hydrate phase change material. The oil served as an interface between the PCM and water, spreading the heat over the surface. A black absorber plate was above the oil to collect solar energy.

The use of built in PCM storage in a solar air heater is much less common. Enibe [70] used a natural convection driven heater where air flowed below the absorber and through banks of paraffin wax. The absorber had high thermal conductivity. A minimum temperature rise of 7°C with 200 W/m$^2$ of incident radiation was obtained. Jain [71] used an air heater for crop drying that contained a sensible heat storage medium placed below the absorber plate. The collector contained two glazings and air passed between the glazings and then over the absorber plate. It then passed under the bottom side of the absorber storage combination, and into the crop dryer. He achieved a minimum temperature rise of 5°C during the night with 900 W/m$^2$ of incident radiation. The efficiency of the dryer never exceeded 35%.

The air heater closest to what is desired here is due to Fath [72]. He used a series of close packed tubes containing wax, hot salts, or sand (for comparison with sensible heat storage). The tubes were arranged close to each other in parallel to make a a flat-plate-style configuration with air flowing above and below them simultaneously. A schematic diagram of his flow path is shown in Figure 5-2.
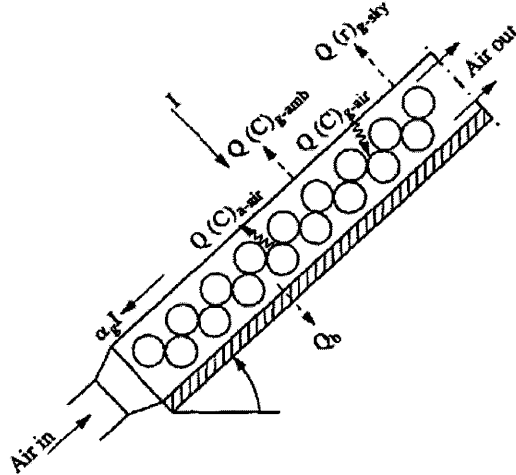
Figure 5-2: Schematic diagram of heater with storage from Fath.

The collector could maintain a minimum of 5°C of temperature difference and ran at design conditions 8 hours longer than a collector without storage. The collector used a wax PCM that melted at 51°C.

## 5.3.2 Enhancing PCM Conductivity

Paraffin wax is commonly used as a phase change material because it melts at specific temperatures, is unreactive, and is inexpensive. The properties of wax used are given in Table 5.1 [73].

Table 5.1: Material properties of paraffin wax storage material

| Material Properties | Solid | Liquid |
|---|---|---|
| Heat Capacity [J/kgK] | 2950 | 2510 |
| Density [kg/m$^3$] | 818 | 760 |
| Thermal Conductivity [W/mK] | 0.24 | 0.24 |
| Latent Heat Capacity [J/kg] | 226,000 | |
| Melting Temperature | 58 °C | |

This wax, like others, has low thermal conductivity which can result in substantial thermal resistance between the heat transfer surface and melt front within the wax. It is important that heat from the absorber plate can melt the entire depth of the

PCM. To get around this problem and better utilize the PCM, a metal matrix with high thermal conductivity can be embedded in the PCM [74]. The most cost effective matrix of this type is an aluminum wool or mesh grid. This method has been utilized in heat exchangers with phase change material buffering, but has not been used in a solar collector.

The conductivity of the matrix and PCM combination is calculated by using the relative density, $s$, of the metal wool. For example, commercial metal wool [75] has a density of 128 kg/m$^3$ giving it a relative density, $s$, of 0.05, when compared to solid aluminum which has an average density of 2700 kg/m$^3$. The thermal conductivity of the PCM-matrix system is given by Equation 5.3

$$k_{\textit{eff}} = (s)k_{Al}/3 + (1-s)k_{PCM} \qquad (5.3)$$

The factor of 1/3 takes into account the random internal structure of the wool: only an average of 1/3 of the threads are carrying heat through any given orthogonal direction. A similar equation is used for metal foams [76], which are stiffer but have a similarly random internal structure. Therefore the same equation applies. For wire mesh, where the threads are only aligned in two directions, 1/3 is replaced by 1/2 using similar reasoning.

In this study aluminum wool is assumed to be imbedded in the PCM.

**Effect of Aluminum on Other Thermal Properties**

Addition of an aluminum mesh or wool has effects on the other thermal properties of the system. It changes the sensible heat capacitance or $(\rho c_p)$ product. This change varies with the relative density of aluminum. Equation 5.4 shows how the sensible heat capacitance of the added aluminum compares with the wax.

$$\frac{(\rho c_p)_{Al}s}{(\rho c_p)_{PCM}(1-s)} \sim \frac{s}{1-s} \qquad (5.4)$$

Since $s$ remains small, on the order of 0.1, the addition of the aluminum matrix does not significantly change the sensible heat storage.

## 5.4 Mathematical Model

A simple lumped parameter model was used in Chapter 3 to describe the temperatures and heat fluxes in a solar collector operating at constant irradiation with no heat capacity and transient effects. Due to the inclusion of transient effects in this study, there are spatial and temporal temperature variations in the absorber plate, and, as a result, an irregularly shaped PCM melt front that varies along the length of the collector, as well as in the depth of the PCM. Therefore, more detailed modeling is required to determine the temperature distribution and melt front shape in the storage material. Finite element modeling which enables a numerical solution of the heat equation in two dimensions and time is an appropriate choice. Due to its ability to handle temperature dependent material properties, the ADINA finite element modeling system was chosen [77].

### 5.4.1 Phase Change Model

Because ADINA does not have a method for handling phase change calculations, the phase change had to be encapsulated as part of the heat capacity of the material. This has been done in previous finite element simulations using two different methods. One, due to Leoni and Amon [74], raises the heat capacity at the melting temperature to represent the energy absorption associated with melting the substance. It is given in the following equation:

$$c_p = c_{p_s} \quad \text{for } T < T_{melt} \tag{5.5a}$$

$$c_p = c_{p_l} + \frac{h_{sf}}{\delta T} \quad \text{for } T = T_{melt} + \delta T \tag{5.5b}$$

$$c_p = c_{p_l} \quad \text{for } T > T_{melt} + \delta T \tag{5.5c}$$

The other method is to neglect the ordinary sensible heat and to treat the latent heat as an increasing heat capacity that changes as the substance gets warmer. This is proposed by Gong and Mujumdar [78] and is given as Equation 5.6:

$$c_p = \frac{h_{sf}}{(T_{melt} - T)} \qquad (5.6)$$

Because Equation 5.6 does not allow for temperatures beyond the melting point and neglects sensible heat storage, the first method was chosen for the numerical model.

## 5.4.2 Solar Radiation Model

Solar irradiation was calculated for Dammam, Saudi Arabia for mid-July using the isotropic sky model [31] and constant environmental data given in Table 5.2. Data for the daily variation of solar radiation as it varies throughout the day in Dammam were obtained from the European Union Joint Research Center PVGIS Database [79]. Data were obtained for both a horizontal surface and a tilted surface at the optimal angle of 26.4°. Values for ground reflectivity were obtained [31, 80, 81] and a value of 0.3 was used for a typical desert environment.

Table 5.2: Constant parameters for simulating baseline design of collector with storage

| Constants | Values |
|---|---|
| Ambient Wind Speed | 5 m/s |
| Latitude | 26.4 ° |
| Solar Declination | 23 ° |
| Collector Tilt Angle | 26.4 ° |
| Collector Inlet Temperature | 30 °C |
| Ambient Air Temperature | 30 °C |
| Dew Point Temperature | 4 °C |
| Insulation Conductivity | 0.02 W/mK |

With this known it is possible to obtain an expression for the heat radiation input $S$:

$$S = I_{T,beam}(\tau\alpha)_{beam} + I_{T,d}(\tau\alpha)_d + I\rho_{s,gr}F_{cg}(\tau\alpha)_{gr} \qquad (5.7)$$

The $(\tau\alpha)$ product for beam irradiation was calculated based on the incidence angle of of the sun's rays (based on solar declination and collector tilt angle as described in Chapter 3), the index of refraction of the glazings, the glazing thickness, the absorber absorptivity, and the extinction coefficient of the glazings, given in Table 5.3.

Table 5.3: Baseline values of material properties.

| Material Properties | Value |
|---|---|
| Glazing Refraction Index | 1.526 |
| Glazing Extinction Coefficient | 4 |
| Absorber Solar Absorptivity | 0.94 |
| Glazing IR Emissivity | 0.92 |
| Absorber IR Emissivity | 0.86 |
| Metal Matrix Relative Density | 0.07 |

For the other $(\tau\alpha)$ products, the same calculation was made except that the incidence angle was replaced with an effective tilt angle of diffuse and ground reflected radiation [31]. Each of the $(\tau\alpha)$ products are listed in Table 5.4.

Table 5.4: $(\tau\alpha)$ product values for each component of solar irradiation.

| $(\tau\alpha)$ Product | Value | Effective Angle |
|---|---|---|
| Beam | 0.78 | 22.5 ° |
| Diffuse | 0.71 | 57 ° |
| Ground Reflected | 0.36 | 77 ° |

The isotropic sky model is more accurate that the method used in for the heater without storage, where all radiation is assumed to be beam radiation. The second method overestimates the radiation input into the collector as shown in Figure 5-3
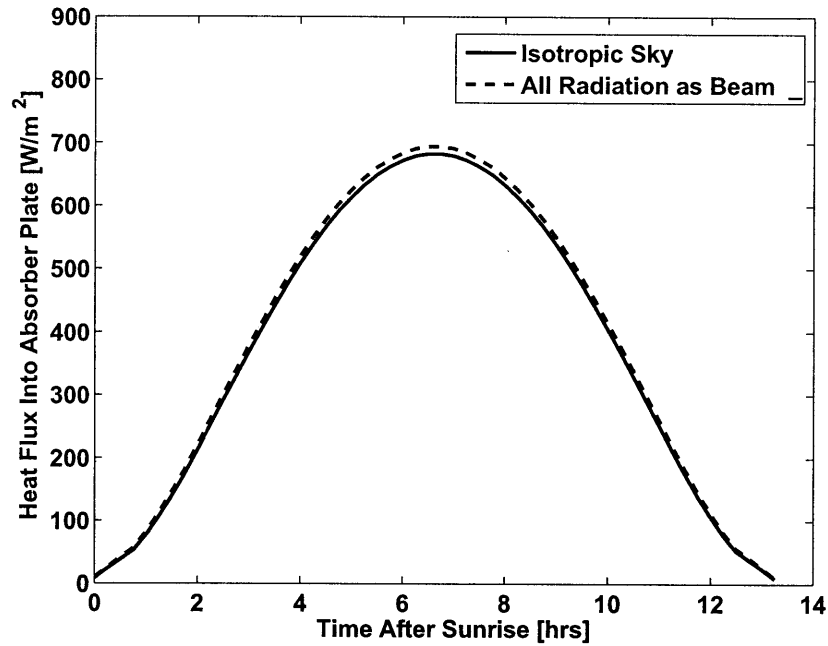
Figure 5-3: Profile of radiation input into the collector for beam radiation and isotropic sky model for reference location and time of year. Time is hours after sunrise.

## 5.4.3 Heat Transfer Model

The solar collector was modeled using a two dimensional finite element model. This was necessarily as the collector was long giving rise to streamwise temperature gradients, and the PCM has thickness, giving rise to depth-wise temperature gradients in the PCM. The end result is that the PCM is not at a uniform phase throughout, and cannot be modeled using a lumped parameter model as was used in Chapter 3 to describe the collector without storage. Figure 5-4 shows the various regions of the finite element model.
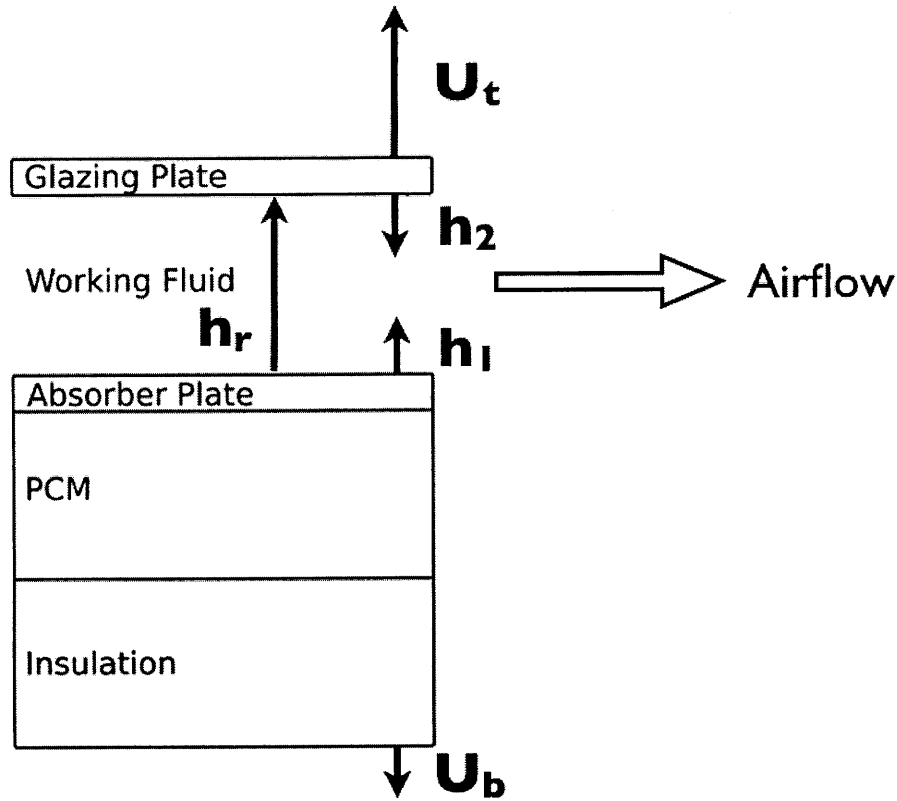
Figure 5-4: Layout of two dimensional finite element model of a solar collector with built-in storage

The model's regions communicate thermally by direct contact (conduction) or by the convection/radiation heat transfer coefficients shown in the figure. This model uses a fixed thermal resistance for heat transfer into the air (i.e., the heat transfer coefficients $h_1$, $h_2$), which avoids the complexity and computational power required of a full turbulence model of the air stream. The resistance added by the second glazing due to the natural convection between the two glazings is lumped into a single top loss coefficient, $U_t$. This avoids the computational complexity of modeling the convection cell in between the plates.

**External Loss Coefficients, $U_t$, $U_b$**

The loss coefficients were modeled as convective boundary conditions at the top of the first glazing and the bottom of the insulation. The finite element model uses a

single upper thermal resistance (akin to a single inner glazing) which accounts for the thermal resistance of natural convection between the glazings, the forced convection due to wind over the top glazing, and radiative transfer between the glazings and the upper glazing and the sky. The conduction resistance in the second glazing is negligible compared to the other resistances in the cover system. The presence of temperature-dependent radiation and natural convection heat transfer makes this convection coefficient temperature dependent. Boundary conditions in ADINA can be made dependent on the boundary temperature and some fixed ambient temperature.

Since the model only contains the inner glazing, to avoid modeling the fluid mechanics of the natural convection cell, the temperature of the outer glazing must be estimated in order to calculate the the various heat transfer coefficients comprised in the top loss coefficient, $U_t$. To estimate this temperature, the average temperature difference between the glazings from the collector without storage from Chapter 3 was used. Since this collector operated at the peak solar radiation expected in a desert climate (900 W/m$^2$), this value was a slight overestimate of the temperature. However, this does not have a large effect on the accuracy of the final result as the natural convection and radiation heat transfer coefficients are weakly dependent on the temperature difference between the plates. This temperature was found to be 15.1°C lower than the top plate. Using this method, $U_t$ is tabulated as a function of the inner cover temperature, and can be entered into ADINA as a temperature dependent boundary condition. $U_b$ is constant and it is entered as a simple convective boundary condition.

**Airflow Model**

The bulk temperature of the air stream was calculated without simulating the cross-channel velocity distribution. Instead, heat transfer coefficients $h_1$ and $h_2$ were calculated on the upper and lower surfaces of the channel and these were applied as thermal resistances to the top and bottom. In this design, there is a thermal entry length were the heat transfer coefficient is within 20 percent of the fully developed value in 10 hydraulic diameters [35], or 60 cm for this collector. Since this length

is 6% of the total collector length the flow can be approximated as thermally fully developed along the entire length. Assuming the flow is mostly fully developed and the heat transfer resistance constant, it is easy to represent these resistances as thin layers of material (0.1 mm thick) between each plate and the air stream of arbitrary conductivity. Figure 5-5 shows the location of these synthetic materials, indicated by the arrows.
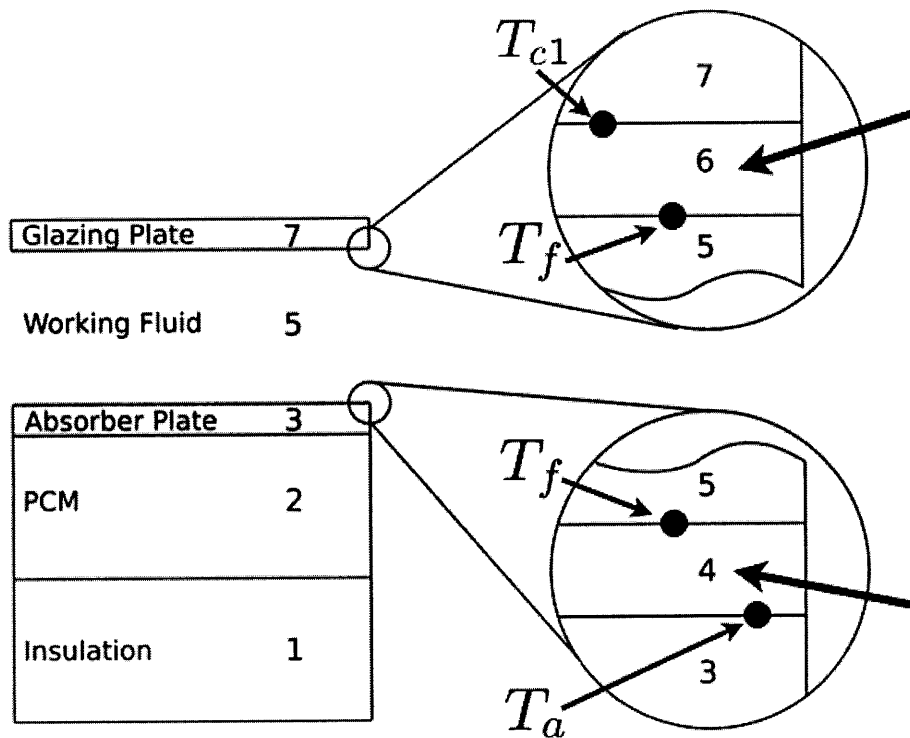


Figure 5-5: Layout of two dimensional finite element model showing applied thermal resistances and temperatures at their edges.

These layers contain the entire temperature gradient between the absorber and bulk air or glazing and bulk air, as shown in the figure. The air is then modeled as a slug flow at a bulk temperature $T_f$. The materials communicate with the plate via conduction and have a conductivity set to match the thermal resistance of the actual convection process.

## Radiation Heat Transfer Between the Absorber and Glazing

Radiation heat transfer between the absorber and upper glazing can be modeled as a linearized heat transfer coefficient. It is not dependent on the air temperature, only the temperatures of the two plates, and therefore it cannot be easily wrapped into the synthetic materials that encapsulate the convective heat transfer. However, if the bulk fluid temperature is used, the radiation heat transfer can be separated into two linearized coefficients by Equation 5.8:

$$h_r(T_a - T_{c1}) = h_r(T_a - T_f) + h_r(T_f - T_{c1}) \tag{5.8}$$

With this equation, $h_r$ can be added to the constant convection coefficient and wrapped into the conductivity of the synthetic layer that represent the convection coefficients. The only difference is that $h_r$ is dependent on both plate temperatures, but coefficient attached to one thin material can be made dependent only on that material. Therefore it is necessary to estimate temperature difference between the plates, $\Delta T$. The temperature difference $\Delta T$ was obtained from the analysis of the collector without PCM from Chapter 3 and computing the average temperature difference between the absorber plate and the inner glazing. This value can be used to calculate $h_r$ as defined by Equation 5.9:

$$h_r = \sigma \mathcal{F}[T^2 + (T_a - \Delta T)^2](2T_a - \Delta T) \quad \text{on the absorber plate side} \tag{5.9a}$$

$$h_r = \sigma \mathcal{F}[T^2 + (T + \Delta T)^2](2T + \Delta T) \quad \text{on the glazing plate side} \tag{5.9b}$$

As shown in Figure 5-5 there is a temperature gradient in the synthetic materials between the plate temperature and the air temperature. Thus, any temperature dependent thermal resistance will vary though the thickness of the synthetic layers. Since the radiation heat transfer coefficient is only a function of a plate temperature,

this is only an approximate solution to the radiative transfer; however the temperature difference between the top and bottom of these thin materials varies by only 5 K on average, and the radiation heat transfer coefficient is much more strongly dependent on the absolute temperature of a plate than temperature difference between the two plates; as a result the effect of that temperature difference is averaged with an error in the radiation heat transfer coefficient, $h_r$, of no more than 4%.

## 5.5   Simulation Results

### 5.5.1   PCM Depth Optimization

To estimate the necessary PCM depth it was assumed that the PCM can be described as a lumped parameter system governed by the following differential equation:

$$\rho_{PCM} h_{sf} \frac{d}{dt} V_{PCM} = S A_p - \dot{m} c_p (T_{out} - T_{in}) - (U_t + U_b) A_p (T_a - T_{amb}) \qquad (5.10)$$

where terms are defined in nomenclature. The differential equation is an energy balance where the change in energy in the PCM (extent of melting) is equal to the solar radiation absorbed less the energy removed by the air and energy lost to the environment. Recognizing that the PCM volume is $A_p d_{PCM}$, where $d_{PCM}$ is the depth of PCM melted, and that the first order equation gives rise to a time constant $\tau_c$ for melting, an estimate for the depth melted in a time span $\tau_c$ can be derived.

$$d_{PCM} = \frac{\tau_c}{\rho_{PCM} h_{sf}} \left[ S - \frac{\dot{m} c_p}{A_p} (T_{out} - T_{in}) - (U_t + U_b)(T_a - T_{amb}) \right] \qquad (5.11)$$

Since the inlet temperature is taken to be the ambient temperature and the plate temperature is close the the fluid outlet temperature (due the stabilizing effects of the PCM) each temperature difference can be approximated to be on the order of

$(T_{melt} - T_{amb})$. This gives a first estimate of the PCM thickness of order 10 cm.

To optimize the PCM depth, the ADINA simulation was run at the slowest possible flow rate to maintain turbulent flow through the collector (46.8 kg/hr) for 6 different PCM depths on the order of 10 cm: 4 cm to 14 cm in 2 cm increments. Figure 5-6 shows the temperature profile for several PCM thicknesses at a mass flow rate of 46.8 kg/hr. This shows that the 8 cm depth gives the most consistent temperature output with the least amount of PCM, with temperature output becoming less sensitive to PCM thickness as it increases beyond this depth.
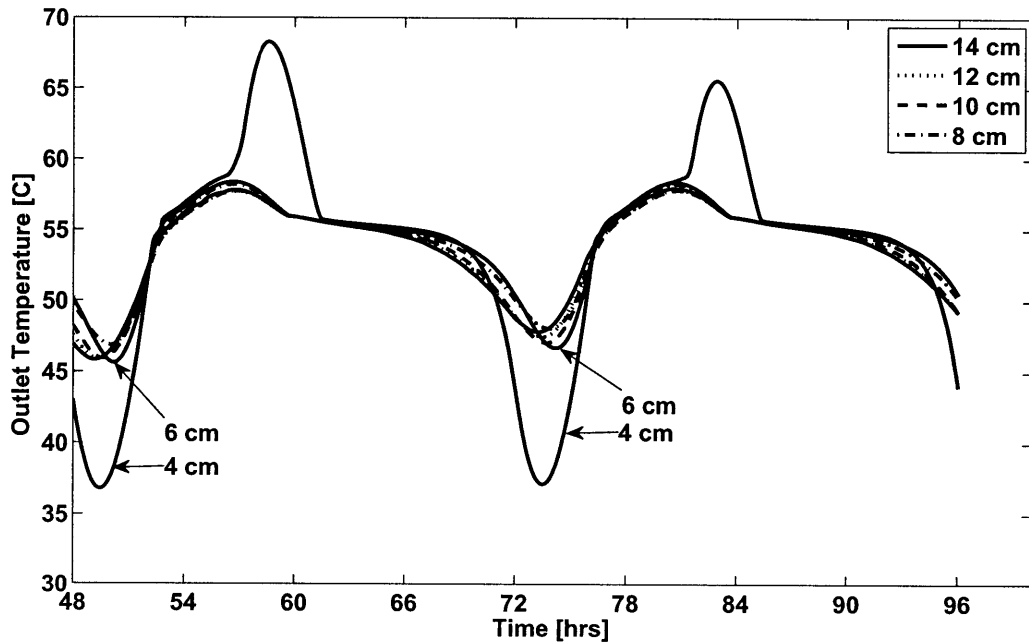


Figure 5-6: Outlet temperature profiles for various PCM thicknesses at $\dot{m} = 47$ kg/hr.

## 5.5.2 Outlet Temperature Stabilization

The ADINA model was initially run for 96 hours with a total of 1000 time steps, using the dimensions shown in Figure 5-1 with various mass flow rates, from 0.013 to 0.052 kg/sec (46.8 to 186.8 kg/hr), representing Reynolds numbers in the duct from 4000 to 16000 in steps of 2000. Figure 5-7 shows the outlet temperature over time for

two consecutive days after warm up transients have been allowed to die out during the first two days of operation.
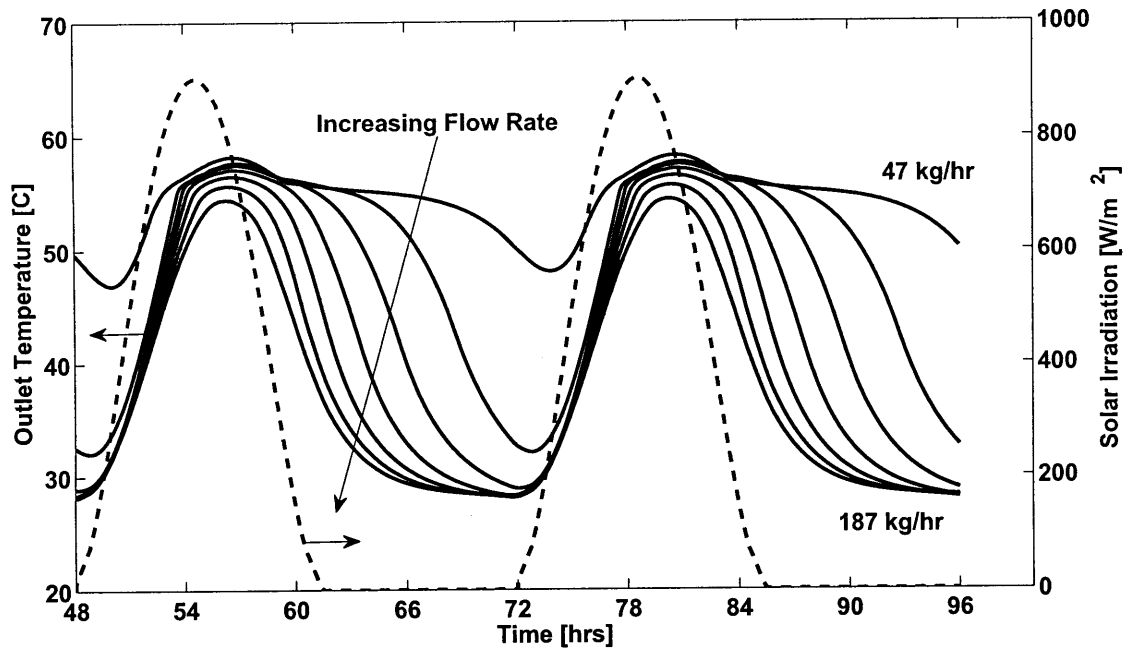


Figure 5-7: Temperature as a function of time for two days of consecutive operation for multiple mass flowrates from 47 kg/hr to 187 kg/hr in increments of 20 kg/hr.

The figure shows that a sustained air output temperature can be obtained by slowing the mass flow rate, which lowers the Reynolds number, allowing more energy to be stored for use at night. The sustained output temperature is near the melting point of the phase change material. The finite element simulation for $\dot{m} = 46.8$ kg/hr shows minimal superheating of the PCM.

However, with sustained output temperature comes a trade-off in efficiency. Figure 5-8 shows the efficiency as a function of the time averaged normalized gain.
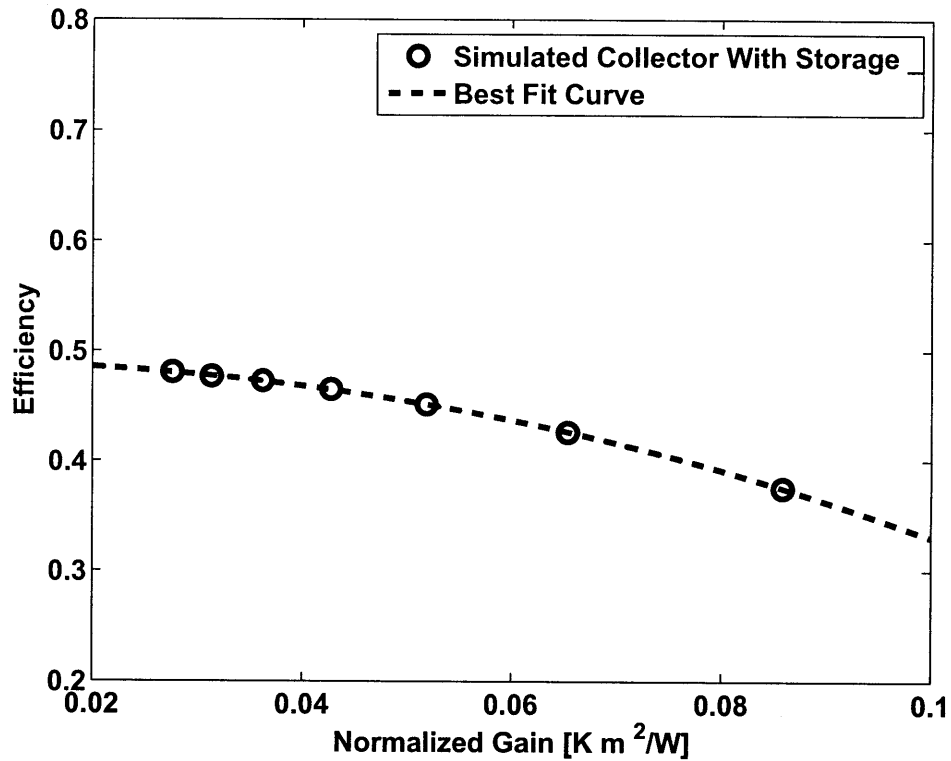
Figure 5-8: Time-averaged collector efficiency vs. time averaged normalized gain with curve fit.

The efficiency displays a logarithmic drop-off as shown by the best fit (least squares) curve with $r^2 = 0.99$ that is shown on the graph. It can be seen that to gain a more constant operating temperature throughout the night the collector has to operate very inefficiently. This is because the collector runs hotter for a longer time when producing a consistent temperature output, so the integrated heat loss over the run period is larger.

## 5.5.3 Variation with Latent Heat of Solidification

Phase change materials are available at a variety of latent heat capacities and melting temperatures. They range in latent heats of solidification from 120 kJ/kg to 300 kJ/kg for materials which sufficiently high melt temperatures for HD cycle operation [82, 83]. Selection of the melt temperature is dependent on the top temperature

required by the HD cycle. Figure 5-9 shows the effect of latent heat of the PCM on outlet temperature with the outlet temperature becoming more stable as latent heat goes up. However with a greater latent heat a smaller amount of PCM is melted as seen in Figure 5-10. Values greater than 1 and less than 0 mean the PCM is completely melted, or completely frozen respectively.
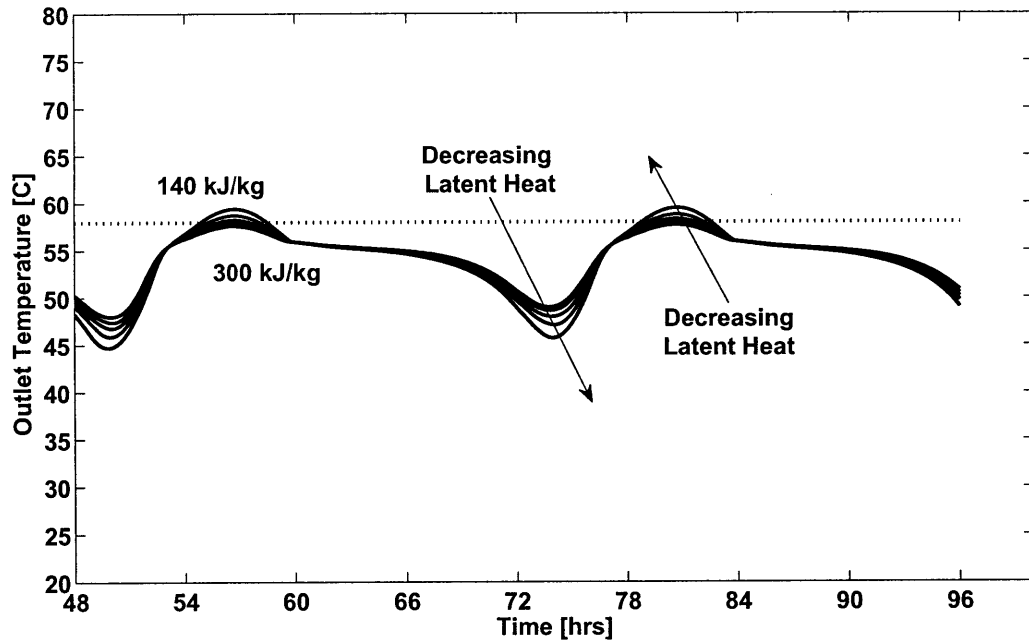


Figure 5-9: Outlet temperature profiles for various latent heat of solidifications: 140 kJ/kg to 300 kJ/kg in increments of 40 kJ/kg at $\dot{m} = 47$ kg/hr. Melting temperature is shown with the dotted line.
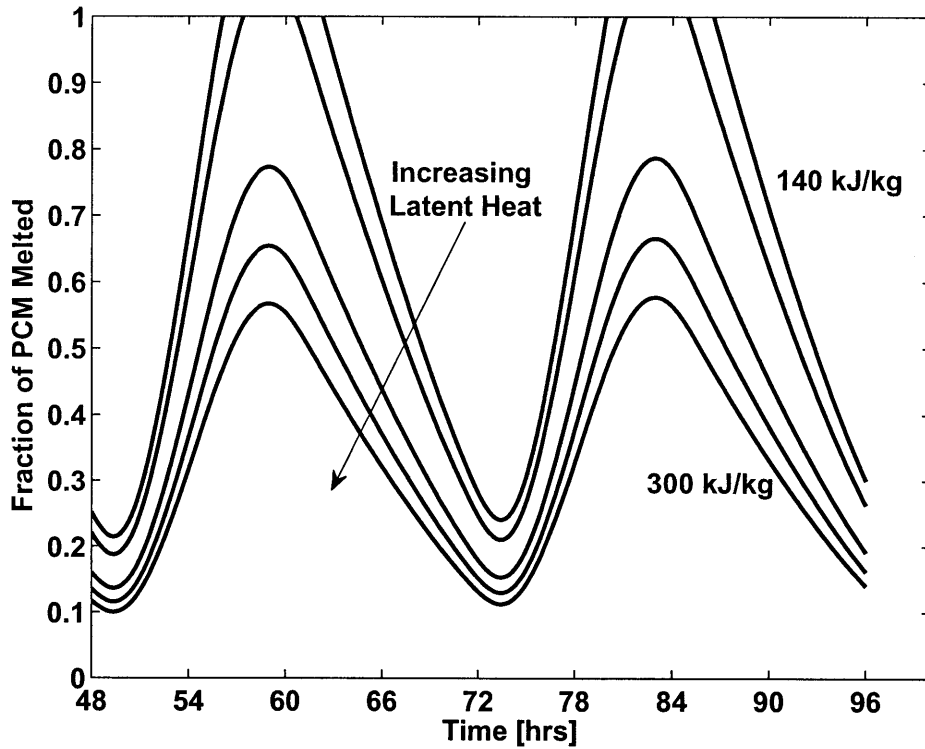
Figure 5-10: Fraction of PCM melted for various latent heat of solidifications: 140 kJ/kg to 300 kJ/kg in increments of 40 kJ/kg at $\dot{m} = 47$ kg/hr.

## 5.5.4 Variation with Increased Metal Matrix Solidity

Increasing the relative density of the metal matrix allows more heat to be conducted through the metal and deeper into the storage layer. It also increases lateral conduction in the streamwise direction. The net effect is that the plate temperature is more stable and more energy is stored in the latent heat resulting in a more stable outlet temperature. This is shown in Figure 5-11, where the temperature clearly becomes more stable with increasing relative density. The curve for the wax only assumes no natural circulation of the melted portion of the wax.
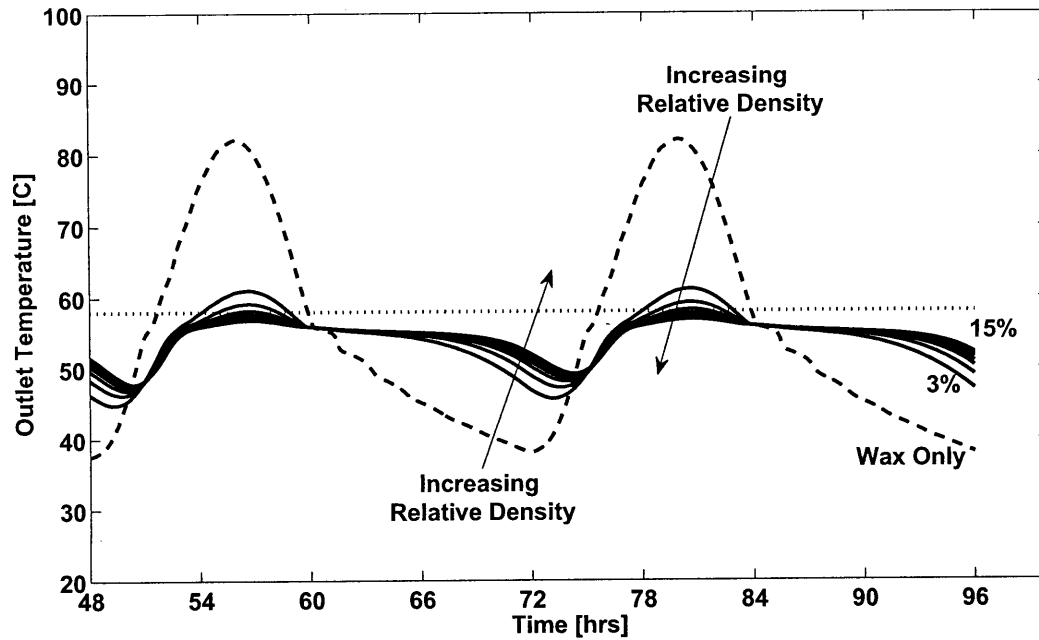
Figure 5-11: Outlet temperature profiles for various metal mesh relative densities: 3% to 15% in increments of 2% at $\dot{m} = 47$ kg/hr. Melting temperature is shown with the dotted line. The configuration factor is 1/3 for all lines.

## 5.5.5 Variation with Changes in Surface Roughening

Decreasing the surface roughening decreases heat transfer coefficient to the air and increases the temperature difference between the air and the absorber plate, which is held close to the melt temperature of the PCM. Figure 5-12 shows how the outlet temperature varies with changes in transverse rib spacing.
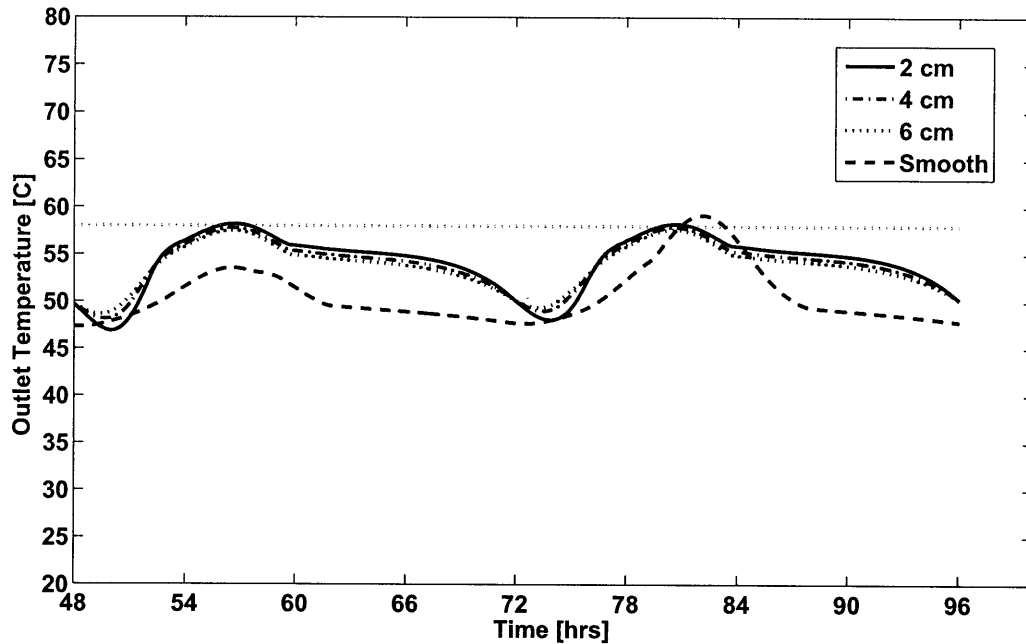
Figure 5-12: Outlet temperature profiles for various roughness rib separation distances at $\dot{m} = 47$ kg/hr. Melting temperature is shown with the dotted line.

In this case, increased temperature stability goes with increased spacing, or lower roughness. This allows less heat to transfer to the air stream and more to be stored in the PCM, thus decreasing the dip in temperature at the end of the night. In the case where the plate has no roughening the temperature is significantly lower than the melt temperature, and the collector still has large thermal transients after 3 days. This also suggests that, as the collector runs for more consecutive days, significant superheating of the PCM will occur, resulting in lower temperature stability. In order to take advantage of the relatively low heat transfer into the air a material with higher latent heat of solidification would be able to store this energy at a specified melt temperature.

# Chapter 6

# Experimental Prototype Design

## 6.1 Introduction

The previous chapter established a model for using a phase change material under the absorber as a viable way of storing energy and achieving near constant temperature operation. A physical experiment in real world conditions could be used to validate the model. Therefore a scaled-down physical collector was constructed.

The physical collector would have the same cross-sectional profile as the modeled collector as shown in Figure 5-1, but instead of being 10 m long, it is 1 m long to allow for a more easily constructed device.

The main challenges with turning the simulated collector into a physical device are selecting the phase change material and dealing with the thermal expansion and contraction of the material, which can be quite large.

Additionally, since this is a one-off prototype, mass manufacturing processes that require the use of dies and molds could not be used, requiring most of the components to be machined or custom made elsewhere. This substantially drives us cost and would not reflect the per square meter cost of a larger mass-manufactured solar array.

## 6.2   Collector Top: Absorber Plate and Glazings

The absorber plate and glazings area made of glass and metal construction as detailed in the previous chapter. Figure 6-1 shows the construction of the top.
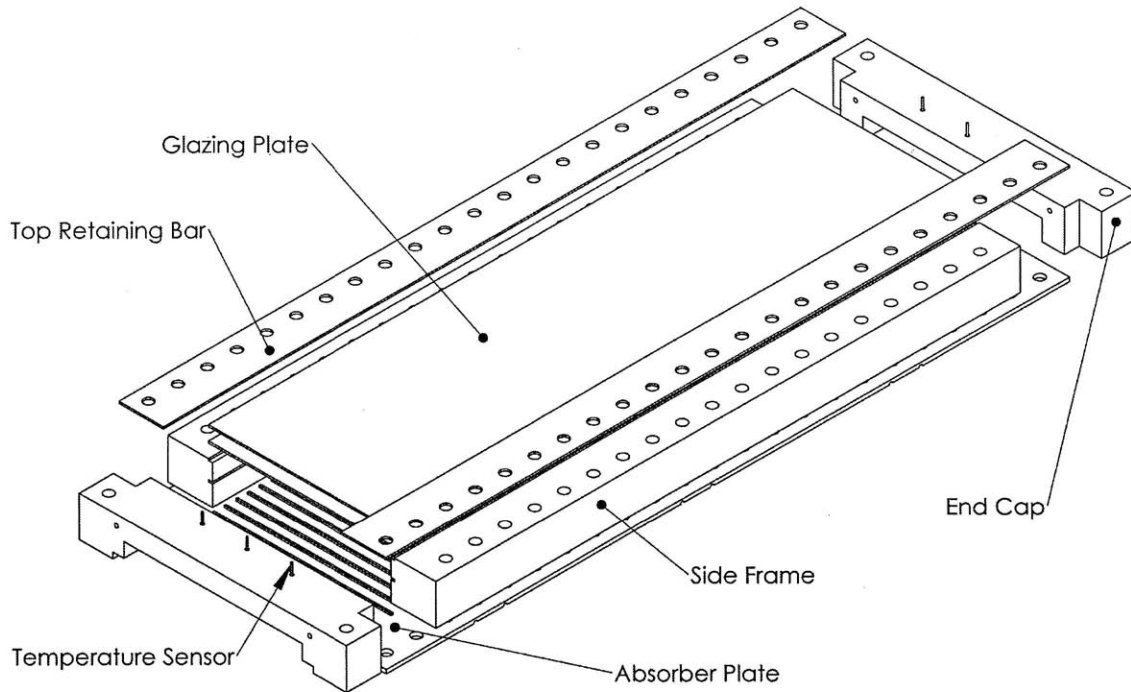


Figure 6-1: Prototype collector top.

### 6.2.1   Absorber Plate

The absorber plate was made out of 6061-T6 aluminum and is 1/4 inch (6.25 mm) thick. As this is an experimental collector, this thickness accommodates embedded temperature measurements, as shown in Figure 6-2
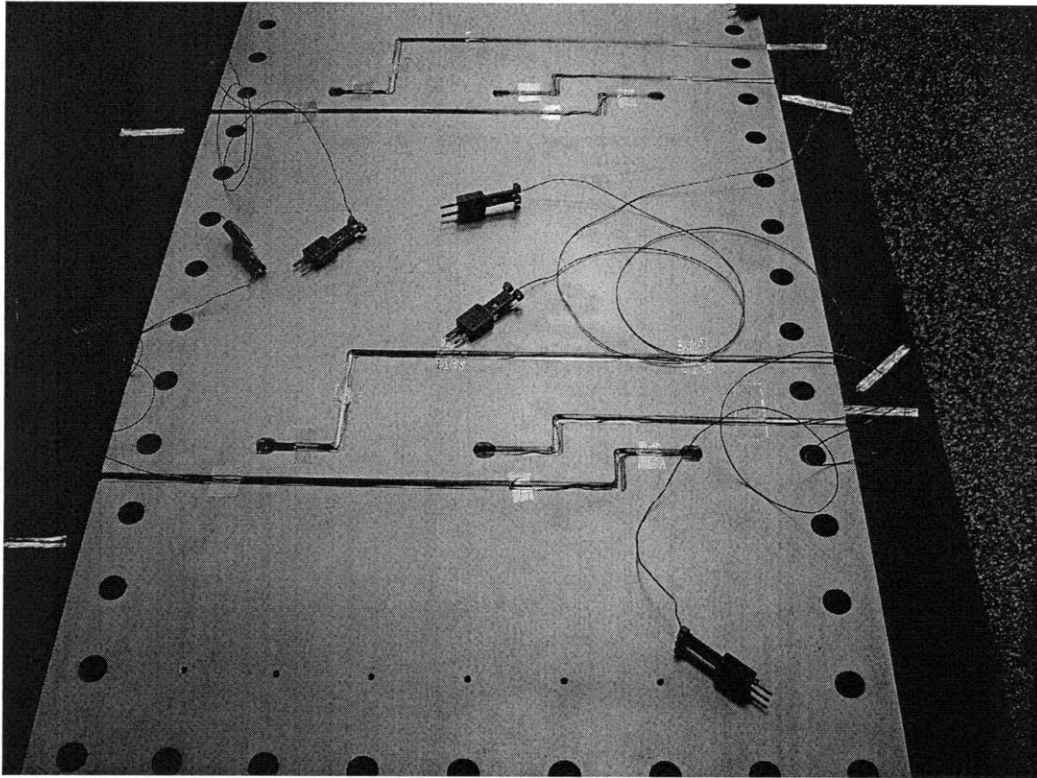
Figure 6-2: Absorber plate showing grooves for the placement of temperature sensors.

The absorber plate was machined and included transverse rib roughening for its simplicity of manufacturing by this method. The roughening specifications were identical to the simulated collector given in Table 3.3. The top of the absorber was coated in Rust-o-leum professional grade spray paint pigmented with carbon black for high solar absorptivity ($\alpha = 0.96$, $\epsilon = 0.88$). Figure 6-3 shows the coated absorber surface.

Figure 6-3: Top surface of rib-roughened absorber plate.

## 6.2.2 Glazing Plates

A double glazing design was implemented matching the simulated collectors. The glazings were mounted in wooden guide rails. Wood was chosen for its low thermal conductivity to avoid conducting heat into the glazings. The grooves were oversized as to avoid cracking of the glazings under differential thermal expansion from both materials. The wooden rails were mounted with screws onto a structural aluminum box frame. This frame is separated from the hot absorber plate by a piece of 1 inch (25.4 mm) thick wood acting as thermal break. This setup is shown in Figure 6-4.
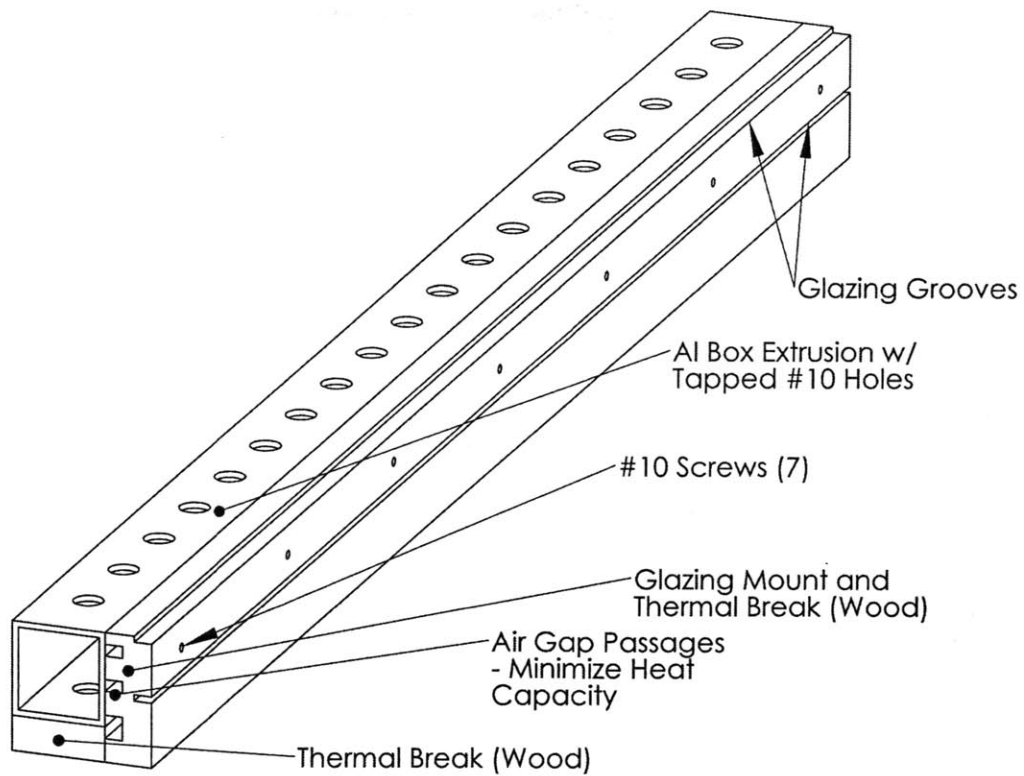
Figure 6-4: Diagram showing the configuration of the glazing support system.

On top of the upper glazing is an aluminum cap holding everything in place. This is bolted down to the absorber plate through the bolt holes shown.

Lastly plastic endcaps, made of HDPE, are used to mount inlet and exit ducting and mount the temperature sensors that measure the airstream inlet and outlet temperature. The temperature sensors are mounted in delrin holders, to minimized heat conducted from the sensor to the environment. These holders are then set into the end caps as shown in Figure 6-5 and are removable.
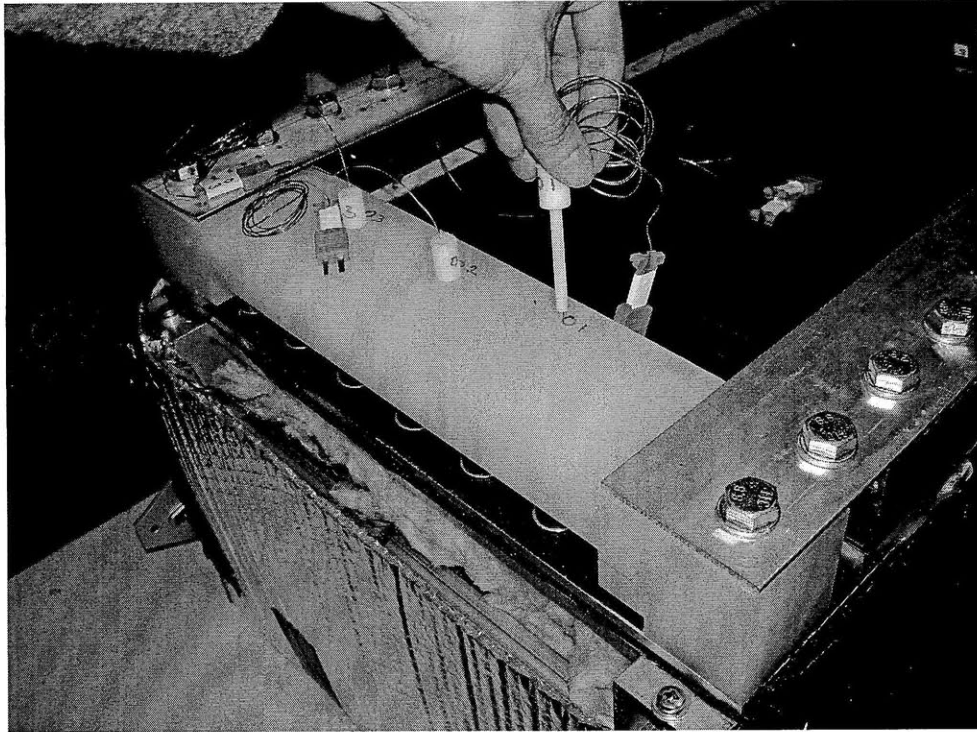
Figure 6-5: End caps and mounting configuration of temperature sensors.

## 6.3    Phase Change Material and Thermal Expansion

Paraffin wax was used as a phase change material because of its variety of melting points and its robustness to thermal cycling. The wax was manufactured by Candlewic to have a melting point of 51 °C. However, the wax comes with a great deal of thermal expansion. As shown in Table 5.1, the density increases by 7% when the wax melts to become liquid. In a rigid container the melting would lead to a large pressure increase which would cause the wax to leak from the container's seals or, at worst, rupture the container.

To accommodate this expansion and assure that the wax remains in contact with the hot absorber plate as it shrinks, a spring loaded rubber bellows is used. The bellows are made of EPDM rubber, similar to that found in automobile tires, which has a working temperature far in excess of temperatures experienced in the collector.

106

The bellows is sealed against the bottom of the absorber plate by sandwiching it between a structural aluminum box frame, and the absorber plate by the means of the through bolts mentioned in the previous section. It is shown in Figure 6-6.
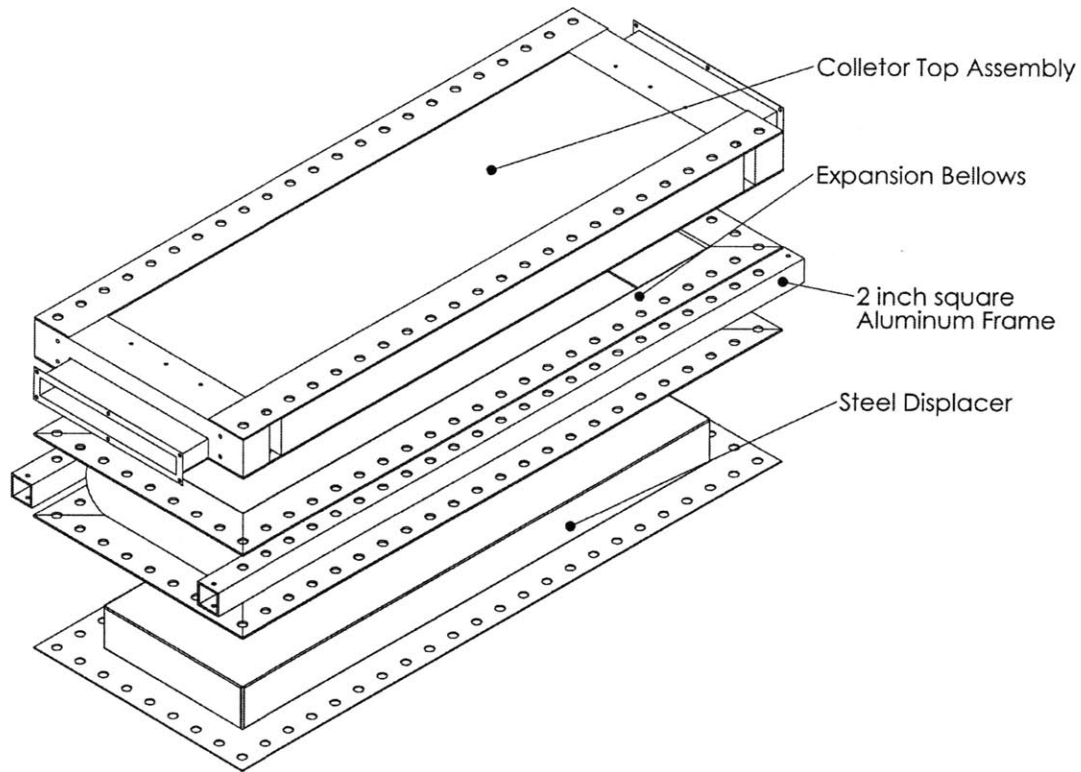


Figure 6-6: Diagram showing the configuration of the bellows as it mounts to the absorber plate.

To enhance the wax thermal conductivity a folded aluminum mesh was employed. This mesh is made of 6061-T6 aluminum for its high thermal conductivity. It was folded in an accordion pattern giving a total relative density of $s = 0.087$. The mesh is held against the absorber plate by thick steel wire wrapped around screws in the bottom of the absorber. Figure 6-7 shows the aluminum mesh attached to the absorber plate. The wax was chosen to have similar properties as those used in the similar collector and listed in Table 5.1. However, to obtain melting of the wax, a 51 °C melting point wax was used.
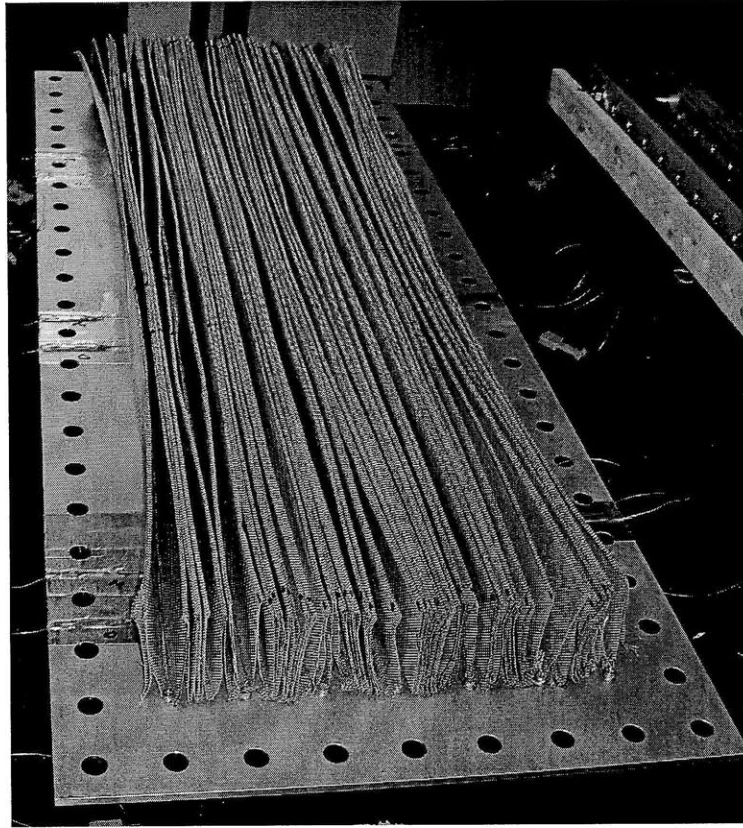
Figure 6-7: The folded aluminum mesh attached to the absorber with steel wire.

Lastly, since the bellows could only be manufactured to a minimum of 6 inches (15.24 cm) from top to bottom, and the wax layer required is only 8 cm a steel displacer is used to take up the rest of the thickness. This is bolted on to the bottom of the bellows. Springs are them used to compress the entire assembly upward. They are sized to provide a force equivalent to 2.5 times the dead weight of the steel and wax combined when mounted. Figure 6-8 shows a schematic diagram of the wax and mesh as it fits into the whole assembly. Figure 6-9 shows its physical realization.
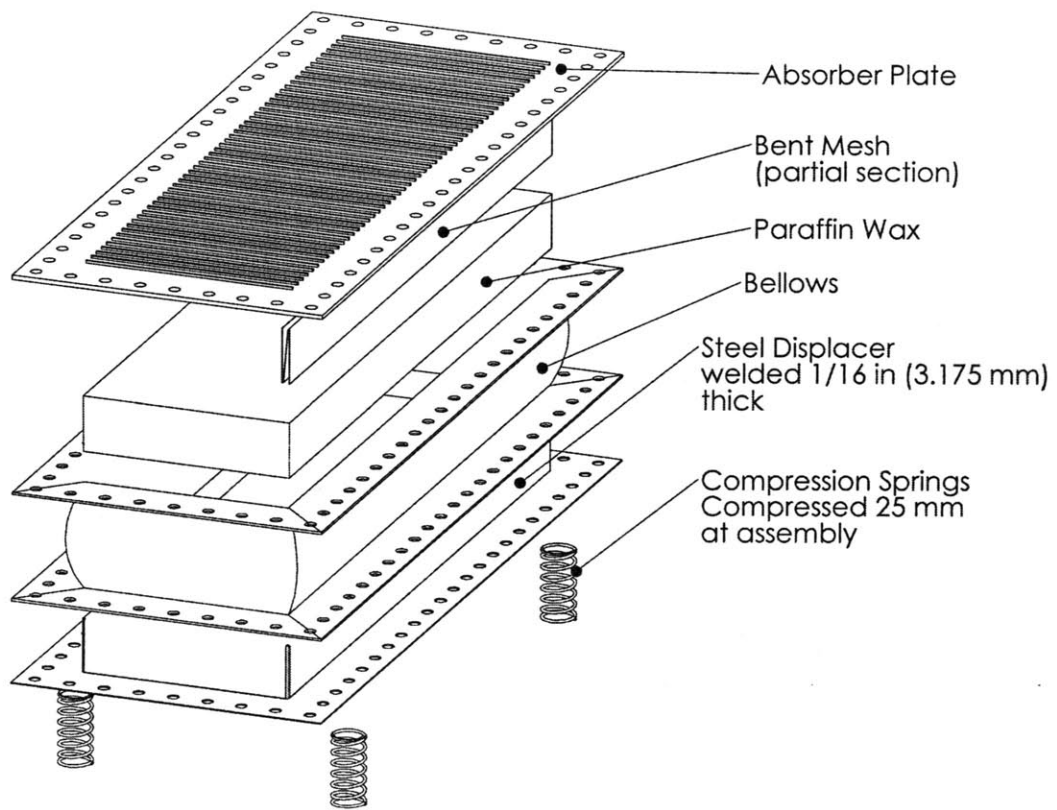
Figure 6-8: Schematic diagram of energy storage (bottom) portion of the collector.

Absorber Plate

Bent Mesh
(partial section)

Paraffin Wax

Bellows

Steel Displacer
welded 1/16 in (3.175 mm)
thick

Compression Springs
Compressed 25 mm
at assembly
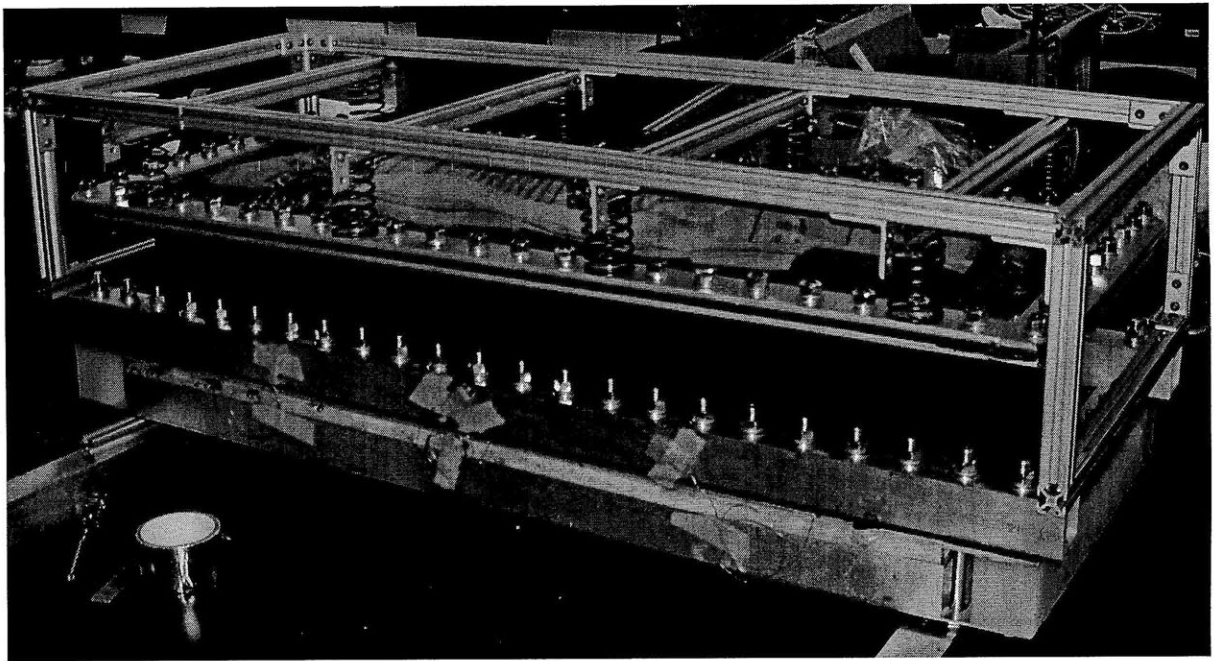
Figure 6-9: Assembled energy storage (bottom) portion of the collector.

Lastly the whole assembly is mounted on an 80/20 frame that retains the springs and enables the insulating of the bottom section as shown in Figure 6-10. Fiberglass insulation ($k = 0.02$ W/mK) is used and then covered by a reflective thermal radiation shield.
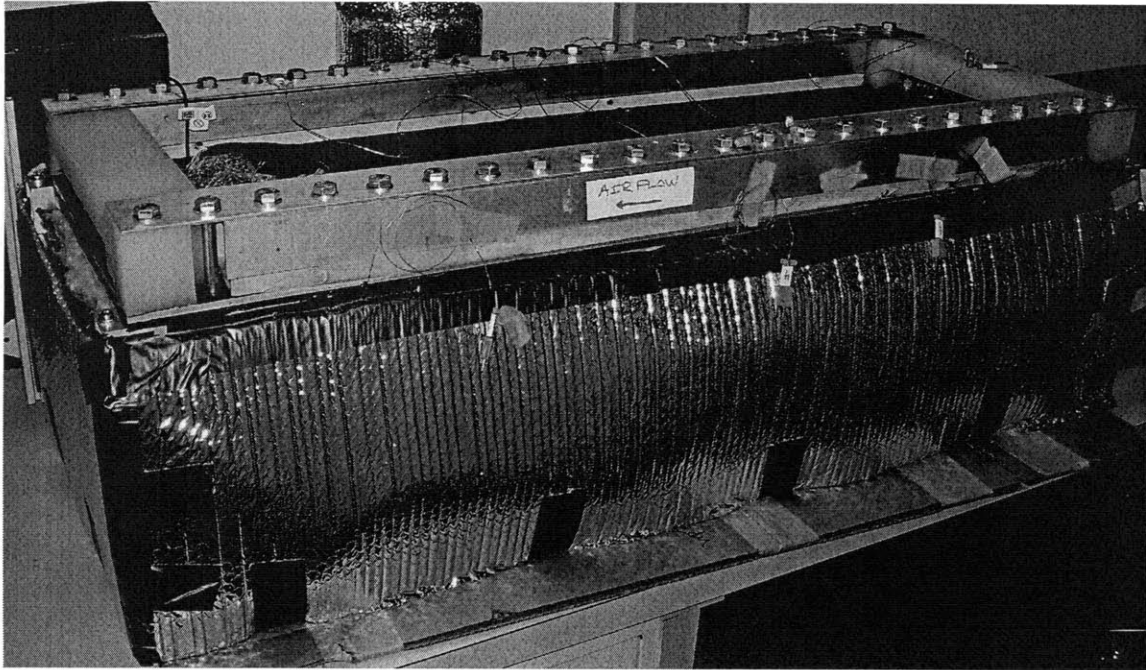


Figure 6-10: Final assembly of the collector and bottom surrounded by insulation.

## 6.4 Temperature Sensing

Temperature sensing was done with T-type thermocouples. Using a standard calibration curve for type T thermocouples manufactured with special limits of error wire would result in a measurement error of +/-0.5 °C at the low temperatures used in an HD cycle. At low temperatures thermistors might be more accurate, but interfacing with data acquisition systems in Saudi Arabia would be easier using thermocouples. Also the small sensor area of thermocouples enables easy interfacing with the absorber plate. Figure 6-2 shows thermocouples embedded in the plate. After these are installed the grooves are sealed over with aluminum tape to prevent the wax from leaking.

## 6.5 Testing

The tests will be done at KFUPM in Daharan, Saudi Arabia as the subject of future work. The abundant solar resources of this area make the tests more feasible than if they were conducted at MIT.

# Chapter 7

# Conclusions

Low temperature solar air heating has been investigated in two respects, for instantaneous efficiency and how that is effected by material properties, and utilizing an energy storage method to output heat at a constant temperature.

## 7.1 Heater Without Storage

The sensitivity study revealed important facts about material properties and heater design to be considered when selecting materials and designing the overall configuration for the heater. Overall, improving the transmissivity of the glazing by using highly transmissive polymer films or low iron glass, and using a very absorptive absorber, which is inexpensively accomplished by including a carbon black coating would have the largest impact on performance. The greatest improvement to a collector's performance can be accomplished by using a double glazing, resulting in a 20% efficiency increase in the HD operating range compared to a single glazed collector. This reduces radiative losses as glass is opaque to infrared radiation. An insulating layer of trapped air between the plates also lowers the outer collector temperature and further decreases convective and radiative losses. The second most important enhancement is the addition of a rough surface on the absorber plate, which improves convection from the heat source to the air. This offers up to a 12% efficiency increase without the need for a selective surface on the absorber. Adding a selective surface to the

absorber, or a low $\epsilon$ coating to the glazing can add a great deal of cost due to the use of exotic materials. In the H operating range these improvements have limited impact on performance, even as environmental conditions change adversely. Using a low emissivity absorber, or a selective surface which does not emit infrared radiation is therefore not important when a heater is well insulated and has good heat transfer characteristics.

Of the environmental conditions that effect performance, wind speed has the greatest impact. The wind speed increases the already dominant convective losses from the collector.

In addition to being highly transmissive, the glazing has to resist wear and discoloration by UV light. This essentially rules out polymer glazings for the upper glazing surface. Even glass materials have to be transmissive, like white water glass. The absorber, on the other hand, has more options as it can be coated with high absorptivity material like carbon black paint.

The heater geometry is very flexible and can change to suit the heat output needs of the heater. For instance, a long effective length can be gained with using a double pass heater. Since hydraulic diameter of the heater is relatively large pressure drop through the heater is not an issue, and the pressure drop of a complete HD system would be mostly likely governed by the humidifier, especially if it has a packed bed.

This heater preformed better than those found in literature, as shown in Figure 3-8. A collector with a double glazing, a highly roughened absorber, and a carbon black coated absorber, results in a collector efficiency of 58% at a normalized gain of 0.06 K m$^2$/W. This is because the heater employed all the measures used to cut losses and improve heat transfer to the air stream that were not used on every design found in literature. For instance, one design might have two glazing plates, but not use rough surfaces, and therefore would work less efficiently then one that had both. Also this model is only a computer simulation, which might lead to higher performance than for experimental results found in literature.

114

## 7.2 Heater With Storage

Investigating the solar collector beyond a simple collector with no heat capacity, energy storage is investigated. Energy storage is a critical component of systems that rely on a variable source of energy, but would perform better with a constant energy input into that system.

Built-in latent heat energy storage has shown great promise to maintain a consistent temperature output throughout the entire day and night. A finite element model is used to assess the performance of a built-in storage system with paraffin wax and an embedded aluminum matrix to enhance the wax layer conductivity. This case of a phase change material allows the plate temperature to be stabilized and the outlet temperature to be roughly limited to the melt temperature of the phase change material. Optimization of surface roughness characteristics can lead to greater temperature stability, and increasing the conductivity of the PCM layer though a metal mesh increases PCM utilization and temperature stability because energy can penetrate deeper into the layer. All of these improvements will enhance the solar driven humidification-dehumidification distillation cycle by eliminating transients and warm up time associated with other system components by maintaining the top temperature of the system at an optimal operating temperature. However these improvements come at the cost of thermal conversion efficiency requiring larger collector areas for given heat outputs. This could dramatically increase the cost of a large scale system, suggesting that this method of energy storage may not be the workable at large scales.

## 7.3 Future Work

This work revealed a great deal about the workability of solar air heating for HD desalination, and represents an investigation of the thermal performance of such systems. However to get a better understanding of how feasible such devices would be in an actual HD system, a cost analysis needs to be preformed. Chapter 4 investigated the cost impact of using alternative materials to glass a metal construction and con-

cluded that they would meet the requirements of thermal performance and be cost competitive in some cases. However a complete cost of a manufactured collector per square meter has not been established, which would be important, given that the collectors can be 40% of an HD desalination system's cost.

Chapter 5 suggested the built-in storage may not be the most effective means of energy storage, especially at large scales, as running at a high constant temperature day and night can double the amount of time that the collector looses heat. An analysis that compares the thermal performance of other energy storage systems, as well as their cost, would ascertain the feasibility of storage at different scales.

Chapter 5 also shed light on the transient behavior of a collector with heat capacity, but at a constant inlet temperature. In an actual HD system the collector would be subject to varying inlet temperatures. Integrating the transient model of this collector with other transient simulations of the total HD system would more accurately characterize the performance of the collector and its impact on the amount of water produced.

# Appendix A

# Parameter Sensitivity Study Code

```
1  %Sensitivty Study of Soalr Air Collectors
2  %Edward Summers
3  %October 9, 2008
4  %
5  %rev 4 modified Jan 1, 2010
6
7  clear all;
8
9  i=0;
10 ii=0;
11
12 %For time integrated efficiency calculations
13
14 [vec_time, vec_irr]=AdDammanSolarRad('Jul');
15 subd_time=((24.88-max(vec_time))/.25)+((min(vec_time)-0.88)/0.25);
16 last_e=numel(vec_time);
17 for(i=last_e+1:last_e+subd_time)
18     vec_time(i)=vec_time(i-1)+0.25;
19     vec_irr(i)=0;
20 end
21 vec_time=vec_time-vec_time(1);
22
23 %Loop to vary second parameter in two-parameter study
24
25 %vec_b=(0.013:0.001:0.2);
26
27 %for(ii=1:numel(vec_b))
28
29
30
31 %following sequence clears all vairables except i and ones needed to make
32 %plots in the end before starting a new loop
33 clear a*;clear A*;clear b*;clear B*;clear c*;clear C*;clear d*;
```

117

```
34  clear D*;clear ep*;clear F*;clear g*;clear G*;clear h*;clear H*;
35  clear I*;clear j*;clear J*;clear k*;clear K*;clear l*;clear L*;
36  clear m*;clear M*;clear nu*;clear N*;clear o*;clear O*;clear p*;
37  clear P*;clear q*;clear Q*;clear r*;clear R*;clear s*;clear S*;
38  clear t*;clear T*;clear u*;clear U*;clear V*;clear w*;
39  clear W*;clear x*;clear X*;clear y*;clear Y*;clear z*;clear Z*;
40
41
42  %mass flow rate vector for curves
43
44  %vec=(0.013:0.001:0.2);
45
46  %vector for first parameter
47
48  %vec=(1:1:400);
49  vec=(0.01:0.001:0.4);
50
51  %
52  %
53
54  %loop for varying one parameter
55
56  for(i=1:numel(vec))
57
58
59  %following sequence clears all vairables except i and ones needed to make
60  %plots in the end before starting a new loop
61  clear a*;clear A*;clear b*;clear B*;clear c*;clear C*;clear d*;
62  clear D*;clear ep*;clear F*;clear g*;clear G*;clear h*;clear H*;
63  clear I*;clear j*;clear J*;clear k*;clear K*;clear l*;clear L*;
64  clear m*;clear M*;clear nu*;clear N*;clear o*;clear O*;clear p*;
65  clear P*;clear q*;clear Q*;clear r*;clear R*;clear s*;clear S*;
66  clear t*;clear T*;clear u*;clear U*;clear V*;clear w*;
67  clear W*;clear x*;clear X*;clear y*;clear Y*;clear z*;clear Z*;
68
69
70
71  %Calculation Flags - Turn on and off certain features
72
73  %Roughness
74  Rough_fl =1;
75  %Covers (1 = one cover, 2 = 2 covers)
76  Covers_fl=2;
77  %Super selective absorber
78  Sel_Abs_fl=0;
79
80
81  %
82
83  %Constant Values
84  sigma = 5.6697e-8; %steffan boltzman constant
85  m_dot = 0.029; %[kg/s] speed of working fluid through collector
86  flag=0;
87  lambda = 0.75;
```

```matlab
88
89  %Regional constants
90  I = 900; %[W/m^2] solar radiation for an average location in Saudi Arabia
91
92  V_amb = 5; %[m/s] ambient wind speed
93  T_air = (273+30); %[K] ambient temperature for average loc Saudi Arabia
94  T_dew = 4; %[C] typical dewpoint temp for a desert location in july
95
96  phi = 0.471; %[rads] the lattitudinal angle of an area in Northen KSA
97  ∆_dec = 0.403; %[rads] the declination angle of the sun on July 17
98  theta_tilt = pi()/4; % tilt angle of the collector
99
100 theta_I = abs(phi−∆_dec−theta_tilt); %incidence angle D&B 1.6.8a
101
102
103 %constant properties of air at 47 C, AHTT Table A.6
104 rho_air = 1.103; %[kg/m^3]
105 cp_air = 1008; %[J/kg*K]
106 mu_air = 1.935e−5; %[kg/m*s]
107 k_air = 0.02753; %[W/m*K]
108 Pr_air = 0.708;
109 alpha_air=k_air/(rho_air*cp_air);
110 nu_air = mu_air/rho_air;
111 g = 9.8;
112
113 %constant material properties
114 %glass
115 k_glass = 0.14; %[W/mK] from Ashby Tables
116 n_glass = 1.526; %index of refraction from Duffie and Beckman
117 epsilon_glass = 0.92; %from http://www.infrared−thermography.com/material−1.htm
118 K_ext = 4; %[1/m] from Duffie and Beckman, extinction cof of water white
119
120 %lower plate insulation
121 k_ins = 0.02; %[W/m*K]
122 t_ins = 0.1; %[m]
123
124
125 %other material constants
126 t_glaz = 0.0025; %[m] thickness of glass chosen
127 d_sep_c = 0.03; %[m] speration distance between two plates
128
129 %absorber plate qantities
130 %material properties from AHTT for carbon black paint
131 alpha_abs = 0.94;
132 epsilon_abs = 0.86;
133 rho_abs = 0.86;
134
135 %roughness − transverse ribs
136 h_r = 0.003175; %[m] roughness height
137
138 p_r = 0.02; %[m] roughness pitch
139
140
141 %oveall dimensions of Unit (can be varied)
```

119

```
142  l_chan = 10; %[m]
143  w_chan = 0.30; %[m]
144  d_chan = 0.035; %[m]
145
146
147  %Place value to vary in the run here
148
149      %m_dot=vec_b(ii);
150      d_sep_c= vec(i);
151
152
153  %BEGIN CALCS
154
155  if(Sel_Abs_fl==1)
156      epsilon_abs = 0.05;
157  end
158
159
160  %set of equations for any number of covers, equations apply to a single
161  %cover
162
163  %Glazing Property calculation
164  theta_1 = theta_I;
165  theta_2 = asin(sin(theta_1)/n_glass);
166  %reflectance (duffie and beckman eqs 5.1.4)
167  r_orth = ((sin(theta_2-theta_1))^2/(sin(theta_2+theta_1))^2);
168  r_pll = ((tan(theta_2-theta_1))^2/(tan(theta_2+theta_1))^2);
169
170  %absorbtance for one cover eq 5.2.2
171  t_a = exp((-K_ext*t_glaz)/cos(theta_2));
172  alpha_glaz = 1 - t_a;
173
174  %components of absrobtance eqs 5.3.1-3
175  t_orth= (t_a*(1-r_orth)^2)/(1-(r_orth*t_a)^2);
176  rho_orth = r_orth*(1+(t_a*t_orth));
177  alpha_orth = (1-t_a)*((1-r_orth)/(1-r_orth*t_a));
178
179  t_pll = (t_a*(1-r_pll)^2)/(1-(r_pll*t_a)^2);
180  rho_pll = r_pll*(1+(t_a*t_pll));
181  alpha_pll = (1-t_a)*((1-r_pll)/(1-r_pll*t_a));
182
183
184  if(Covers_fl==1)
185      %set of euqations for one cover (d and b equations 5.3.4-5.3.5)
186      t_r = (1/2)*(((1-r_pll)/(1+r_pll))+((1-r_orth)/(1+r_orth)));
187
188      t_glaz=t_r*t_a;
189      rho_glaz= t_a-t_glaz;
190  end
191
192  if(Covers_fl==2)
193      %set of equations to be used for two covers
194      %transmittance eq 5.3.7, 5.3.8
195      t_orth_tot = (t_orth^2/(1-r_orth^2));
```

120

```matlab
196    t_pll_tot = (t_pll^2/(1-rho_pll^2));
197    t_glaz = (1/2)*(t_orth_tot+t_pll_tot);
198    rho_glaz = (1/2)*((rho_orth+(t_orth_tot*rho_orth*t_orth)/...
199        t_orth)+(rho_pll+(t_pll_tot*rho_pll*t_pll)/t_pll));
200 end
201
202
203 %final set of transmittance absorbtance equations
204
205 %absorber transmittance-absorb product not used at this time
206 ta_prod = t_glaz*alpha_abs/(1-(1-alpha_abs)*rho_glaz);
207 R_beam = cos(theta_I-theta_tilt)/cos((theta_I)); %eq 1.8.1
208
209 %total energy into the collector from solar radiation
210 %All radiation as beam
211 S = I*ta_prod;
212
213
214
215
216
217 %reset any flags used in for loop
218 rf_flag=0;
219
220 %ENERGY LOSS CALCULATIONS
221 %Radiative Loss
222
223 %Sky Temperature D and B eq 3.9.2
224 T_sky=T_air*(0.711+0.0056*T_dew+7.3e-5*T_dew^2+0.013*...
225     cos((15*12)*(2*pi()/360)))^(1/4); %Tsky for noontime [K]
226
227
228 %View Factor flat absorber and lower coverplate, AHTT Table 10.3, eq 1
229 X = w_chan/d_chan;
230 Y = l_chan/d_chan;
231 F_ac = (2/(pi()*X*Y))*(log(((1+X^2)*(1+Y^2)/(1+X^2+Y^2))^(1/2))-X*...
232     atan(X)-Y*atan(Y)+X*(1+Y^2)^(1/2)*atan(X/(1+Y^2)^(1/2))+...
233     Y*(1+X^2)^(1/2)*atan(Y/(1+X^2)^(1/2)));
234 %View factor absorber insulated wall (one half), AHTT Table 10.3, eq 2
235 H = d_chan/l_chan;
236 W = w_chan/l_chan;
237 F_aw = (1/(pi()*W))*(W*atan(1/W)-(H^2+W^2)^(1/2)*atan((H^2+W^2)^(1/2))+...
238     H*atan(1/H)+(1/4)*log(((1+W^2)*(1+H^2)/(1+W^2+H^2))*...
239     ((W^2*(1+W^2+H^2))/((1+W^2)*(W^2+H^2)))^(W^2)*...
240     ((H^2*(1+H^2+W^2))/((1+H^2)*(H^2+W^2)))^(H^2)));
241 %View Factor bottom coverplate and top coverplate
242 X = w_chan/d_sep_c;
243 Y = l_chan/d_sep_c;
244 F_cc = (2/(pi()*X*Y))*(log(((1+X^2)*(1+Y^2)/(1+X^2+Y^2))^(1/2))-...
245     X*atan(X)-Y*atan(Y)+X*(1+Y^2)^(1/2)*atan(X/(1+Y^2)^(1/2))+Y*...
246     (1+X^2)^(1/2)*atan(Y/(1+X^2)^(1/2)));
247 %View Factor lower coverplate and sidewall above it
248 H = d_sep_c/l_chan;
249 W = w_chan/l_chan;
```

```matlab
250  F_cw = (1/(pi()*W))*(W*atan(1/W)-(H^2+W^2)^(1/2)*atan((H^2+W^2)^(1/2))+...
251      H*atan(1/H)+(1/4)*log(((1+W^2)*(1+H^2)/(1+W^2+H^2))*...
252      ((W^2*(1+W^2+H^2))/((1+W^2)*(W^2+H^2)))^(W^2)*...
253      ((H^2*(1+H^2+W^2))/((1+H^2)*(H^2+W^2)))^(H^2)));
254
255  %radiation resistance claculations (see diagram)
256  ep1 = epsilon_abs;
257  ep2 = epsilon_glass;
258  Ap = l_chan*w_chan; %absorber and glazing plate area also the area
259  %through which radiation flows
260  A_lw = l_chan*d_chan; % lower wall area
261  A_uw = l_chan*d_sep_c; %upper wall area
262
263  R1 = (1-ep1)/(ep1*Ap);
264  R2 = (((1/(Ap*F_aw))+(1/(Ap*F_aw)))^(-1)+Ap*F_ac+((1/(Ap*F_aw))...
265      +(1/(Ap*F_aw)))^(-1))^(-1);
266  R3 = (1-ep2)/(ep2*Ap);
267  R4 = (((1/(Ap*F_cw))+(1/(Ap*F_cw)))^(-1)+Ap*F_cc+((1/(Ap*F_cw))+...
268      (1/(Ap*F_cw)))^(-1))^(-1);
269  R5 = (1-ep2)/(ep2*Ap);
270  R6 = 1/(ep2*Ap);
271
272  R_rad_tot = R1+R2+R3+R4+R5; %[1/m^2] total radiation resistance
273  %between e_abs_and e_sky
274
275
276
277
278  %CONVECTIVE LOSS
279
280  %air flowing between absorber and lower glazing
281  %correlations for smooth pipe surface based on hydraulic diameter
282  A_chan = d_chan*w_chan;
283  d_h = 4*A_chan/(2*(d_chan+w_chan));
284  V_chan = m_dot/(rho_air*A_chan);
285  Re_d = rho_air*V_chan*d_h/mu_air;
286  f=(1.82*log10(Re_d) -1.64)^(-2); %AHTT 7.42
287  Nu_d = (f/8)*(Re_d-1000)*Pr_air/(1+12.7*(f/8)^(1/2)*(Pr_air^(2/3)-1));
288  %AHTT eq 7.43 Gnielinski Eq
289  h_plate_bulk = Nu_d*k_air/d_h; %[W/m^2*K]
290
291  %case for roughened pipe %from mills (1992) table 4.8 pg 337
292  %roughening method transverse square ribs
293  if(Rough_fl==1)
294      if((p_r/h_r)>2&&(p_r/h_r)<6.3)
295          k_s = h_r*exp(3.4-3.7*(p_r/h_r)^(-0.73));
296      end
297      if((p_r/h_r)>=6.3&&(p_r/h_r)<20)
298          k_s = h_r*exp(3.4-0.42*(p_r/h_r)^(0.46));
299      end
300      if((p_r/h_r)>=20||(p_r/h_r)<2)
301          rf_flag=1;
302          h_rough = h_plate_bulk;
303      end
```

```matlab
304
305        %h_r=k_s; %mean hieght of protrusions
306
307        f_r = (-2.0*log10(((k_s*2)/(7.4*d_h))-(5.02/Re_d)*log10(((k_s*2)/...
308            (7.4*d_h))+(13/Re_d))))^(-2);
309        u_e = (m_dot/rho_air)/(d_chan*w_chan); %charictaristic velocity
310        h_nd = (u_e*h_r/nu_air)*(f_r/8)^(1/2);
311        k_nd = (u_e*k_s/nu_air)*(f_r/8)^(1/2);
312        g_adj = 4.3*(h_nd)^(0.28)*Pr_air^(0.57); %adjusted gravity for air
313        %g_adj = 0.55*(h_nd^(1/2))*(Pr_air^(2/3)-1)+9.5;
314        St_av = (f_r/8)*(0.9+(f_r/8)^(1/2)*(g_adj-7.65))^(-1);
315        Nu_d=St_av*Re_d*Pr_air;
316        h_rough = Nu_d*k_air/d_h;
317    else
318        %if no roughening the the plate to air transfer ciefficient
319        %is the same as for smooth plate.
320        rf_flag=1;
321        h_rough=h_plate_bulk;
322    end
323
324    %Presure Drop Through The Channel
325    %v_av=(2/3)*(m_dot/(rho_air*w_chan*d_chan));
326    %∆P=(((f+f_r)/2)*(l_chan/d_h)+0.3)*(rho_air*v_av^2/2);
327
328
329    %loss out of the insulation on the bottom only; sidewalls are aidibatic
330    h_ins=(k_ins/t_ins);
331
332    %forced convection loss out of the top; laminar flow for low velocities
333    l_char=(l_chan+w_chan)/2;
334    %l_char=w_chan;
335
336    Re_tr=5e5;
337    Re_l = rho_air*V_amb*l_char/mu_air;
338    Nu = 0.664*Re_tr^(1/2)*Pr_air^(1/3)+0.036*Re_l^0.8*Pr_air^0.4*...
339        (1-(Re_tr/Re_l)^0.8);
340    %Nu = 0.664*Re_l^(1/2)*Pr_air^(1/3);
341    h_amb = Nu*k_air/l_char;
342
343    %guessed temperatures for itarative calculations
344    Tp=273+10; %[K] guessed absorber plate temperature
345    Tc_1 =Tp-10; %[K] inner cover temperature
346    Tc_2 =Tp-20; %[K] outer cover temperature
347    Tc =Tp-10; %[K] guess temp for only single cover
348
349
350    %Guess a Sol-Air Temperature
351    T_amb = T_sky+10;
352
353    clear Tp_vec;
354    clear guess_vec;
355    clear u;
356
357    Tp_vec(1)=Tp;
```

```matlab
358    guess_vec(1)=Tp;
359
360    %reset any flags before the while loop
361    flag=0;
362    r_flag=0;
363
364    %Re_d_vec(i)=Re_d;
365
366    j_c=2;
367
368    while(flag==0)
369
370        guess_vec(j_c)=Tp;
371
372        %Calculate losses from guessed temperatures
373
374        %TEMPERATURE DEPENDENT HEAT TRANSFER COEFFS
375
376
377        if(Covers_fl==2)
378            %Natural convection between two glazings (tilted plates)
379            Ra = g*(2/(Tc_1+Tc_2))*(Tc_1-Tc_2)*d_sep_c^3/(nu_air*alpha_air);
380            %from eqn 3.11.4 in Duffie and Beckman
381            A=(1-1708/(Ra*cos(theta_tilt)));
382            if(A<0)
383                A=0;
384            end
385            B=(((Ra*cos(theta_tilt))/5830)^(1/3))-1;
386            if(B<0)
387                B=0;
388            end
389            Nu_d = 1 +1.44*((1-((1708*(sin(1.8*theta_tilt))^1.6)/...
390                Ra*cos(theta_tilt)))*A)+B;
391            h_stag_air = Nu_d*k_air/d_sep_c;
392
393            %radiation heat transfer coieffs (include areas)
394            hA_rad_cc = (sigma*(Tc_1^2+Tc_2^2)*(Tc_1+Tc_2))/(R3+R4+R5);
395            hA_rad_ac = (sigma*(Tp^2+Tc_1^2)*(Tp+Tc_1))/(R1+R2+R3);
396            hA_rad_cs = (sigma*(T_sky^2+Tc_2^2)*(T_sky+Tc_2))/(R6);
397
398            h_rad_cc=hA_rad_cc/Ap;
399            h_rad_ac=hA_rad_ac/Ap;
400            h_rad_cs=hA_rad_cs/Ap;
401
402            %plate to first cover resistance
403            U_pl_c = (h_rad_ac+(h_rough+h_plate_bulk));
404            %between covers
405            U_c_c = (h_rad_cc+h_stag_air);
406            %outer cover to sky
407            U_c_s = (h_rad_cs+h_amb);
408            %plate to outside through bottom insulation
409            U_pl_bot = ((1/h_ins)+(1/h_amb))^(-1);
410            %U_pl_bot=0;
411
```

```
412     %U's where fluid is not in contact
413     U_t=((1/U_c_s)+(1/U_c_c))^(-1);
414     U_b=U_pl_bot;
415
416     %h's where fluid is in contact
417     h_r=h_rad_ac;
418     h_1=h_plate_bulk;
419     h_2=h_rough;
420     end
421
422     if(Covers_fl==1)
423         hA_rad_ac = (sigma*(Tp^2+Tc^2)*(Tp+Tc))/(R1+R2+R3);
424         hA_rad_cs = (sigma*(T_sky^2+Tc^2)*(T_sky+Tc))/(R6);
425
426         h_rad_ac=hA_rad_ac/Ap;
427         h_rad_cs=hA_rad_cs/Ap;
428
429         %plate to cover resistance
430         U_pl_c = (h_rad_ac+(h_rough+h_plate_bulk));
431         %outer cover to sky
432         U_c_s = (h_rad_cs+h_amb);
433         %plate to outside through bottom insulation
434         U_pl_bot = ((1/h_ins)+(1/h_amb))^(-1);
435
436         %U's where fluid is not in contact
437         U_t=U_c_s;
438         U_b=U_pl_bot;
439
440         %h's where fluid is in contact
441         h_r=h_rad_ac;
442         h_1=h_plate_bulk;
443         h_2=h_rough;
444
445     end
446
447     %find the difference in radiative heat loss between the sky temp and
448     %air temp
449
450     q_IR_Δ = -h_rad_cs*(T_air-T_sky);
451
452
453     %Sol-air temp - assuming the outer structure does not absorb IR
454     %radiation
455
456     T_amb = T_air+(q_IR_Δ/(h_rad_cs+h_amb));
457
458     %CALCULATE TOTAL LOSS
459
460     %total loss coiefficient d&b eq 6.14.8
461     U_L=((U_b+U_t)*(h_r*h_1+h_2*h_r+h_1*h_2)+U_b*U_t*(h_1+h_2))/...
462         (h_r*h_1+U_t*h_2+h_2*h_r+h_1*h_2);
463
464     %flow factor d&b 6.14.7
465     F_p=(h_r*h_1+U_t*h_2+h_2*h_r+h_1*h_2)/...
```

125

```
466        (((U_t+h_r+h_1)*(U_b+h_2+h_r))-h_r^2);
467
468
469    %heat removal factor d & b eqn 6.7.4 for any heater integrated in the
470    %streamwise direction
471    F_R=(m_dot*cp_air/(Ap*U_L))*(1-exp(-(Ap*U_L*F_p)/(m_dot*cp_air)));
472    F_O=F_R/exp(-(Ap*U_L*F_p)/(m_dot*cp_air));
473
474    F_dp=F_R/F_p;
475
476    %knowing removal factor and loss coieffs find new plate temp
477    q_u=(S-U_L*(Tp-T_amb));
478
479    Tp_new=T_amb+(q_u/(F_R*U_L))*(1-F_R);
480    Tf_mean=T_amb+(q_u/(F_R*U_L))*(1-F_dp);
481
482    q_u=(S-U_L*(Tp_new-T_amb));
483
484    %first law and heat loss through top only
485    Q_l=Ap*(-q_u+S)-(Ap*U_pl_bot*(Tp_new-T_amb));
486
487    if(Covers_fl==2)
488
489        a=U_c_c*Ap;
490        b=U_c_s*Ap;
491
492        %bigK=[a -a; b 0];
493        %bigF=Q_l*[1;1]-T_amb*[0;-b];
494
495        bigK=[a -a;0 b];
496        bigF=Q_l*[1;1]-T_amb*[0;-b];
497
498        u=bigK\bigF;
499
500        Tc_1=u(1);
501        Tc_2=u(2);
502    end
503
504    if(Covers_fl==1)
505        Tc=(Q_l/(U_c_s*Ap))+T_amb;
506    end
507
508
509    Tp_vec(j_c)=Tp_new;
510
511    Tp=lambda*Tp+(1-lambda)*Tp_new;
512
513    if(abs(Tp_vec(j_c)-Tp_vec(j_c-1))<.001)
514        r_flag=1;
515        Tp=Tp_new;
516    end
517
518    if(r_flag==1)
519        flag=1;
```

```matlab
520        end
521
522
523        j_c=j_c+1;
524
525 end
526
527     T_inlet=T_air;
528     vec_Q_out(i)=Ap*q_u;
529     vec_ΔT(i)=(Ap*q_u/(m_dot*cp_air));
530     eta(i)=Ap*q_u/(I*Ap);
531     %ng(i)=(T_out-T_inlet)/I;
532     vec_FR(i)=F_R;
533     vec_FO(i)=F_O;
534     vec_Fp(i)=F_p;
535
536
537     % saved vaules for 2 cover system only
538
539
540 %     q_top_conv=h_amb*(Tc_2-T_amb);
541 %     q_top_rad_amb=h_rad_cs*(Tc_2-T_amb);
542 %     q_top_rad_sky=((sigma*(T_sky^2+Tc_2^2)*(T_sky+Tc_2))...
543 %         /(R6))*(Tc_2-T_sky);
544 %
545 %     perc_err_1=((q_top_rad_sky-q_top_rad_amb)/(q_top_rad_sky));
546 %     perc_err_2=((q_top_rad_amb)/(q_top_rad_sky));
547 %
548 %     vec_perc_err_1(i)=perc_err_1;
549 %     vec_perc_err_2(i)=perc_err_2;
550
551     %eta=eta';
552     %ng=ng';
553     vec_Q_out=vec_Q_out';
554     vec_ΔT=vec_ΔT';
555
556     %vec_Re(i)=Re_d;
557     %vec_h_rough(i) = h_rough;
558     %vec_h_smooth(i) = h_plate_bulk;
559     %vec_Tp(i)=Tp;
560     %vec_Tf_mean(i)=Tf_mean;
561     %vec_Re_d(i)=Re_d;
562     %vec_Tc1(i)=Tc_1;
563     %vec_Tc2(i)=Tc_2;
564     %vec_ΔP(i)=ΔP;
565     %vec_t_glaz(i)=t_glaz;
566     %vec_ΔT(i)=T_out-T_amb;
567     %vec_S(i)=S;
568 end
569
570 %used when second parameter is varied
571
572 % vec_b_Qu(:,ii)=vec_Q_out;
573 % vec_b_ΔT(:,ii)=vec_ΔT;
```

```
574
575   %end
576
577   %Used when time-varying radiaiton is used
578
579   %total_I=trapz(vec_time,vec_irr);
580   %total_e=total_I*Ap;
581   %for(ii=1:numel(vec_b_Qu(:,1)))
582   %     eta_int(ii)=trapz(vec_time,vec_b_Qu(:,ii))/total_e;
583   %     ng_int(ii)=trapz(vec_time,vec_b_ΔT(:,ii))/total_I;
584   %end
```

# Bibliography

[1] International Water Management Institute, Ed., *Water for Food, Water for Life: A Comprehensive Assessment of Water Management in Agriculture.* London: Earthscan, 2006.

[2] Florida Solar Energy Center. (2006) Is florida really the sunshine state for solar energy?. University of Central Florida. [Online]. Available: http://www.fsec.ucf.edu/en/media/newsletters/echron/archives/2006/Q2/sunshine.htm

[3] E. Chafik, "A new type of seawater desalination plants using solar energy," *Desalination*, vol. 1, no. 153, pp. 25–37, 2002.

[4] D. Rojas, J. Beermann, S. A. Klein, and D. T. Reindl, "Thermal performance testing of flat-plate collectors," *Solar Energy*, vol. 82, no. 8, pp. 746–757, August 2008.

[5] G. Lof, M. El-Wakil, and J. Chiou, "Residential heating with solar-heated air – colorado solar house," *ASHRAE Journal*, vol. 5, no. 10, pp. 77–86, 1963.

[6] C. L. Gupta and H. P. Garg, "Performance studies on solar air heaters," *Solar Energy*, vol. 11, no. 1, pp. 25–31, January-March 1967.

[7] D. J. Close, "Solar air heaters for low and moderate temperature applications," *Solar Energy*, vol. 5, no. 3, pp. 117–124, July-September 1963.

[8] A. Whillier, "Plastic covers for solar collectors," *Solar Energy*, vol. 7, no. 3, pp. 148–151, July-September 1963.

[9] A. Schmidt, "Solar air heater," U.S. Patent 4 085 729, 1976.

[10] A. Severson and et. al., "Solar air heater," U.S. Patent 4 085 730, 1978.

[11] O. Vincent, "Dome solar air heater," U.S. Patent 4 236 507, 1977.

[12] S. Satcunanathan and S. Deonarine, "A two-pass solar air heater," *Solar Energy*, vol. 15, no. 1, pp. 41–49, May 1973.

[13] N. Bansal, "Thermal performance of plastic film solar air and water heaters," *International Journal of Energy Research*, vol. 11, no. 1, pp. 35–43, Jan-March 1987.

[14] C. Choudhury and H. P. Garg, "Performance of air-heating collectors with packed airflow passage," *Solar Energy*, vol. 50, no. 3, pp. 2005–221, March 1993.

[15] V. K. Sharma, S. Sharma, R. B. Mahajan, and H. P. Garg, "Evaluation of a matrix solar air heater," *Energy Conversion and Management*, vol. 30, no. 1, pp. 1–8, 1990.

[16] M. Mittal and L. Varshney, "Optimal thermohydraulic performance of a wire mesh packed solar air heater," *Solar Energy*, vol. 80, no. 9, pp. 1112–1120, September 2006.

[17] A. Mohamad, "High efficiency solar air heater," *Solar Energy*, vol. 60, no. 2, pp. 71–76, February 1997.

[18] H. Esen, "Experimental energy and exergy analysis of a double-flow solar air heater having different obstacles on absorber plates," *Building and Environment*, vol. 43, no. 6, pp. 1046–1054, June 2008.

[19] M. Sahu and J. Bhagoria, "Augmentation of heat transfer coefficient by using 90 degree broken transverse ribs on absorber plate of solar air heater," *Renewable Energy*, vol. 30, no. 13, pp. 2057–2073, October 2005.

[20] B. S. Romdhane, "The air solar collectors: Comparative study, introduction of baffles to favor the heat transfer," *Solar Energy*, vol. 81, no. 1, pp. 139–149, January 2007.

[21] C. Ho, H. Yeh, and R. Wang, "Heat-transfer enhancement in double-pass flat-plate solar air heaters with recycle," *Energy*, vol. 30, no. 15, pp. 2796–2817, November 2005.

[22] M. Ramadan, A. El-Sebaii, S. Aboul-Enein, and E. El-Bialy, "Thermal performance of a packed bed double-pass solar air heater," *Energy*, vol. 32, no. 8, pp. 1524–1535, August 2007.

[23] C. Kennedy, "Review of mid- to high-temperature solar selective absorber materials," National Renewable Energy Laboratory, Tech. Rep., 2002.

[24] A. Hachemi, "Technical note: Comparative study on the thermal performances of solar air heater collectors with selective and nonselective absorber-plate," *Renewable Enegy*, vol. 17, no. 1, pp. 103–112, May 1999.

[25] V. Teixeira, E. E. Sousa, M. Costa, C. Nunes, L. Rosa, M. J. Carvalho, M. Collares-Pereira, E. Roman, and J. Gago, "Spectrally selective composite coatings of Cr-Cr2O3 and Mo-Al2O3 for solar energy applications," *Thin Solid Films*, vol. 392, pp. 230–326, 2001.

[26] T. Liu, W. Lin, W. Gao, C. Luo, M. Li, Q. Zheng, and C. Xia, "A parametric study on the thermal performance of a solar air collector with a v-groove absorber," *International Journal of Green Energy*, vol. 4, no. 6, pp. 601–622, November 2007.

[27] T. Koyuncu, "Performance of various design of solar air heaters for crop drying applications," *Renewable Enegy*, vol. 31, no. 7, pp. 1073–1088, June 2006.

[28] K. K. Matrawy, "Theoretical analysis for an air heater with a box-type absorber," *Solar Energy*, vol. 63, no. 3, pp. 191–198, September 1998.

[29] Solar Rating and Certification Corporation. (2008) Directory of certified solar collector ratings. [Online]. Available: http://www.solar-rating.org/ratings/OG100DIRECTORIES/OG100DIRFULL.pdf

[30] K. Sopian, M. Alghoul, E. M. Alfegi, M. Sulaiman, and E. Musa, "Evaluation of thermal efficiency of double-pass solar collector with porous-nonporous media," *Renewable Energy*, vol. 34, no. 3, pp. 640 – 645, 2009. [Online]. Available: 88a1b93ea8b31f1a9bfb55691

[31] J. A. Duffie and W. A. Beckman, *Solar Engineering of Thermal Processes*, 3rd ed. Hoboken, NJ: Wiley, 2006.

[32] R. McCullough, "Solar heater with integral heat trap glazing,," U.S. Patent 4 323 053, 1980.

[33] M. Elhadidy and S. Shaahid, "Wind resource assessment of eastern coastal region of Saudi Arabia," *Desalination*, vol. 209, no. 1-3, pp. 199–208, 2007.

[34] J. H. Lienhard V and J. H. Lienhard IV, *A Heat Transfer Textbook*, 3rd ed. Cambridge, MA: Phlogiston Press, 2006.

[35] A. F. Mills, *Heat and Mass Transfer*, 2nd ed. Boston, MA: Irwin, 1992.

[36] M. Dalle Donne and L. Meyer, "Turbulent convective heat transfer from rough surfaces with two-dimensional rectangular ribs," *International Journal of Heat and Mass Transfer*, vol. 20, pp. 583–620, 1977.

[37] DuPont Inc. (2008) DuPont Engineering Plastics Datasheets. [Online]. Available: http://www2.dupont.com/Plastics/en US/Products/index.html

[38] L. Kauder, "Spacecraft thermal control coatings references NASA/TP2005212792," *NASA Technical Publication*, vol. 1, pp. 1–121, December 2005.

[39] M. Ben Amara, I. Houcine, A. Guizani, and M. Maalej, "Comparison of indoor and outdoor experiments on a newly designed air solar plate collector used with the operating conditions of a solar desalination process," *Desalination*, vol. 1, no. 168, pp. 61–88, 2004.

[40] J. Pickett, M. Gardner, D. Gibson, and S. Rice, "Global weathering of aromatic engineering thermoplastics," *Polymer Degradation and Stability*, vol. 90, no. 3, pp. 405–417, December 2005.

[41] T. Schmauder, K. Nauenburg, K. Kruse, and G. Ickes, "Hard coatings by plasma cvd on polycarbonate for automotive and optical applications," in *Selected Papers from the 5th International Conference on Coatings on Glass (ICCG5)- Advanced Coatings on Glass and Plastics for Large-Area or High-Volume Products*, vol. 502, no. 1-2, ICCG-5. Thin Solid Films, April 2006, pp. 270–274.

[42] R. Raman, S. Mantell, J. Davidson, and C. Wu, "A review of polymer materials for solar water heating systems," *Journal of Solar Energy Engineering*, vol. 122, no. 2, pp. 92–100, 2000.

[43] DuPont Inc. (2008) Teflon fep film properties bulletin. [Online]. Available: http://www2.dupont.com/Teflon_Industrial/en_US/assets/downloads/h55008.pdf

[44] ——. (2008) Tedlar: Technical information. [Online]. Available: http://www2.dupont.com/Tedlar_PVF_Film/en_US/assets/downloads/pdf/h49725.pdf

[45] SABIC Innovative Plastics. (2009) Lexin resin properties. [Online]. Available: http://www.sabic-ip.com/gepapp/Plastics/servlet/ProductsAndServices/Product/

[46] IDES Plastics Web. (2006) Impact ps 5410 - nova chemicals - polystyrene high impact. [Online]. Available: http://www.inplexplastictubing.com/images/hips.pdf

[47] DuPont Inc. (2008) Tedlar: Optical properties. [Online]. Available: http://www2.dupont.com/Tedlar_PVF_Film/en_US/assets/downloads/pdf/h49725.pdf

[48] Accredited Gemologists. Makrolon polycarbonate sheet light transmission. [Online]. Available: http://accreditedgemologists.org/lightingtaskforce/SpectralDistClearPolycarbonate.pdf

[49] DuPont Inc. (2008) Teflon: Informational bulletin. [Online]. Available: http://www2.dupont.com/Teflon_Industrial/en_US/assets/downloads/h55007.pdf

[50] I. Ghorbel, F. Thominette, P. Spiteri, and J. Verdu, "Hydrolytic aging of polycarbonate. i. physical aspects," *Journal of Applied Polymer Science*, vol. 55, no. 1, pp. 163–171, 1995.

[51] A. A. Hegazy, "Effect of dust accumulation on solar transmittance through glass covers of plate-type collectors," *Renewable Energy*, vol. 22, no. 4, pp. 525–540, April 2001.

[52] M. Ashby, *Materials Selection in Mechanical Design*, 3rd ed. Boston: Elsevier Butterworth-Heinemann, 2005.

[53] Steel On The Net. (2009, January) Market prices : Steel. [Online]. Available: http://www.steelonthenet.com/prices.html

[54] Metalprices.com. (2009, January) Metal prices & news on the internet. [Online]. Available: http://www.metalprices.com/

[55] B. Anderson and M. Wells. (2005) Selecting the right glazing material. Buld It Solar. [Online]. Available: http://www.builditsolar.com/Projects/SolarHomes/PasSolEnergyBk/Appendix6.pdf

[56] IDES. (2009, January) Plastics marketplace. [Online]. Available: http://www.ides.com/marketplace/default.aspx

[57] J. Greene, "Engineering thermoplastics," Course Presentation, Fall 2008.

[58] Acrylic Fabrication. (2009, January) Polycarbonate sheet price. [Online]. Available: http://acrylicparts.com/lexanprice.html

[59] T. McNamara. (2009, Jaunary) Thermosets - the forgotten engineering plastic. Thermotech. [Online]. Available: http://www.thermotech.com/wn_thermotech.html

[60] A. Eggers-Lura, *Solar Energy for Domestic Heating and Cooling: A Bibliography with Abstracts, and a Survey of Literature and Information Sources.* Pergamon Press, 1978.

[61] H. Garg, "Solar water heating systems," in *Proceedings of the Workshop on Solar Water Heating Systems.* New Delhi, India: Dordrecht, 1985.

[62] S. A. Kalogirou, "Solar thermal collectors and applications," *Progress in Energy and Combustion Science*, vol. 30, pp. 231–295, 2004.

[63] G. P. Narayan, M. H. Sharqawy, E. K. Summers, J. H. Lienhard, S. M. Zubair, and M. A. Antar, "The potential of solar-driven humidication-dehumidication desalination for small-scale decentralized water production." *Renewable and Sustainable Energy Reviews*, vol. 14, no. 4, pp. 1187–1201, May 2010.

[64] G. P. Narayan, M. H. Sharqawy, J. H. Lienhard V, and S. M. Zubair, "Thermodynamic analysis of humidification-dehumidification desalination cycles," *Desalination and Water Treatment*, vol. 16, no. 1, pp. 339–353, April 2010.

[65] A. Shukla, D. Buddhi, and R. Sawhney, "Solar water heaters with phase change material thermal energy storage medium: A review," *Renewable and Sustainable Energy Reviews*, vol. 13, no. 8, pp. 2119–2125, October 2009.

[66] H. Garg, "Year round performance studies on a built-in storage type solar water heater at jodhpur, india," *Solar Energy*, vol. 17, no. 3, pp. 167–172, 1975.

[67] J. Prakash, H. Garg, and G. Datta, "A solar water heater with a built-in latent heat storage," *Energy Conversion and Management*, vol. 25, no. 1, pp. 51–56, 1985.

[68] B. Kumar, "Design, development and performance evaluation of a latent heat storage unit for evening and morning hot water using a box type solar collector," M.Tech, Devi Ahilya University: School of Energy and Enviromental Studies, Indore, India, 2001.

[69] Y. Rabin, I. Bar-Niv, E. Korin, and B. Mikić, "Integrated solar collector storage system based on a salt-hydrate phase-change material," *Solar Energy*, vol. 55, no. 6, pp. 435–444, December 1995.

[70] S. O. Enibe, "Thermal analysis of a natural circulation solar air heater with phase change material energy storage," *Renewable Enegy*, vol. 28, no. 14, pp. 2269–2299, November 2003.

[71] D. Jain, "Modeling the system performance of multi-tray crop dryingusing an inclined multi-pass solar air heater with bulit in thermal storage," *Journal of Food Engineering*, vol. 71, pp. 44–54, 2005.

[72] H. E. S. Fath, "Transient analysis of thermosyphon solar air heater with built-in latent heat thermal energy storage system," *Renewable Enegy*, vol. 6, no. 2, pp. 119–124, March 1995.

[73] A. Haji-Sheikh, J. Eftekhar, and D. Lou, "Some thermophysical properties of paraffin wax as a thermal storage medium," in *AIAA 20th Aerospace Sciences Meeting and the 3rd AIAA/ASME Joint Thermophysics, Fluids, Plasma, and Heat Transfer Conference*, vol. 86, 1983, pp. 241–253.

[74] N. Leoni and H. Amon, "Thermal design for transient operation of the TIA wearable portable computer," in *ASME INTERpack'97 Conf.*, Kona, HI, June 15-18 1997, pp. 2151–2161.

[75] Briwax Online. (2009) Gmt exotic alloy metal wools. [Online]. Available: http://www.briwax-online.com/GMTAlum.html

[76] ERG Areospace. (2009) Material specific properties of duocel foams. [Online]. Available: http://www.ergaerospace.com/foamproperties/matspecificproperties.htm

[77] ADINA R and D, Inc. (2010) ADINA CFD. [Online]. Available: http://www.adina.com/adinaf.shtml

[78] Z. X. Gong and A. S. Mujumdar, "Finite element analysis of cyclic heat transfer in a shell-and-tube latent heat energy storage exchanger." *Applied Thermal Engineering*, vol. 17, no. 6, pp. 583–591, 1997.

[79] European Commission Joint Research Centre. (2010) Photovoltaic geographical information system. [Online]. Available: http://re.jrc.ec.europa.eu/pvgis/apps3/pvest.php

[80] M. M. Elsayed, "Optimum orientation of absorber plates," *Solar Energy*, vol. 42, no. 2, pp. 89 – 102, 1989. [Online]. Available: ead0a3e357d62377e84e38d352e

[81] J. Dave, "Performance of a tilted solar cell under various atmospheric conditions," *Solar Energy*, vol. 21, no. 4, pp. 263 – 271, 1978. [Online]. Available: 4742822e5c046c8b60f243436

[82] M. M. Farid, A. M. Khudhair, S. A. K. Razack, and S. Al-Hallaj, "A review on phase change energy storage: materials and applications," *Energy Conversion and Management*, vol. 45, no. 9-10, pp. 1597 – 1615, 2004. [Online]. Available: 06d1404ede3a1c98ab5ac7d61

[83] S. D. Sharma and K. Sagara, "Latent heat storage materials and systems: A review," *International Journal of Green Energy*, vol. 2, no. 1, pp. 1–56, 2005.